Asphaltene Precipitation and Phase Behavior Analysis During CO_2 Utilization for Enhanced Oil Recovery: Experimental and Modeling Study

By

Julia E. Espinoza Mejia
B.Sc., National University of Engineering (Peru), 2010

Submitted to the graduate degree program in the Chemical and Petroleum Engineering Department and the Graduate Faculty of the University of Kansas in partial fulfillment of the requirements for the degree of Master of Science.

_____
Committee Chair: Xiaoli Li

_____
Committee member: Jyun Syung Tsau

_____
Committee member: Shahin Negahban

Date Defended: 07 June 2022

The thesis committee for Julia E. Espinoza Mejia certifies that this is the approved version of the following thesis:

Asphaltene Precipitation and Phase Behavior Analysis During CO_2 Utilization for Enhanced Oil Recovery: Experimental and Modeling Study

_____

Chair: Xiaoli Li

_____

Graduate Director: Prajnaparamita Dhar

Date Approved: 07 June 2022

Abstract

The study of the asphaltene precipitation problem during CO_2 Enhanced Oil Recovery (EOR) under different reservoir conditions is addressed in this thesis. The general objective of this investigation is to effectively predict asphaltene precipitation using a thermodynamic model. More specific objectives are (a) measuring, comparing, and modelling the saturation points for crude oil and gas injection systems, (b) measuring asphaltene content and asphaltene onset pressures (AOP), (c) analyzing asphaltene-oil-CO_2 phase behavior and reversibility mechanisms, (d) determining asphaltene precipitation weight, and (e) tuning an equation of state (EOS) and a solid model to predict the experimental data using WinProp (CMG, 2011).

The experimental determination of the total asphaltene content in the oil sample is performed following the laboratory standard, ASTM D-3279. Afterward, an advanced fully visual Pressure-Volume-Temperature (PVT) instrument and a Solid Detection System (SDS) are utilized to perform all the saturation pressure and AOP measurements in this work. These two pieces of equipment include a high-resolution camera through which the developed phase behaviors and asphaltenes particle characterization are observed at different pressure and temperature conditions.

From the experimental results, the saturation pressures for all the CO_2-oil mixtures increase directly with CO_2 concentrations and temperature. The upper asphaltene onset pressures (UAOP) increase with CO_2 concentrations in the system and decrease with temperature increments. In contrast, the lower asphaltene onset pressure (LAOP) increases with CO_2 concentrations and temperature increments in all cases. For 25 mole% of CO_2 at 60, 90, and 120 °C, the reversibility

of the asphaltene precipitation process is corroborated. However, irreversible asphaltene precipitation processes are found for 35, and 45 mole% of CO_2 injected at 25 °C. The maximum quantity and most significant size of asphaltene precipitation particles are found at bubble point for all cases. Asphaltenes particles do not have a specific shape, and their colors vary from brown to black. The reversible asphaltene mechanisms developed four different phase behaviors during the isothermal depressurization. In contrast, the irreversible asphaltene mechanisms developed only three phase behaviors.

The crude oil sample characterization and modeling calculus are performed using commercial software, WinProp, from Computer Modelling Group Ltd. (CMG). The model reproduced the experimental saturation pressure measurements by tuning the Peng-Robinson EOS. A solid model is used as a thermodynamic equation. The purpose is to predict asphaltene precipitation under different CO_2 mole% injections for isotherms at 25°C, 60°C, 90°C, and 120°C. This thermodynamic model calculates fugacity of the liquid phase from the tuned Peng-Robing EOS to predict the asphaltene precipitation wt%. Then it is adjusted manually for different solid molar volume parameters. The experimental asphaltene precipitation wt% was successfully modeled for various CO_2 mole% injections for isothermal conditions. A new correlation of the molar volume in function of temperature and CO_2 molar concentrations was developed. The developed correlation successfully predicts the solid molar volume required to match the experimental asphaltene precipitation wt% with an absolute average relative deviation (AARD) of 0.75%.

Acknowledgments

Thanks to God for allowing me to achieve goals that, as a first-generation student I never thought I would be able to aim.

I am grateful for being granted a scholarship from the Fulbright and CAREC institutions, for the study work license from PETROPERU, and the financial support through a teaching assistant position and the Summer Research scholarships from the Chemical and Petroleum Department of the University of Kansas.

A special thank you to my adviser Dr. Li because her patience, encouragement, academic guidance, and role model helped me keep my motivation to complete my goals during the development of this thesis.

Finally, I thank my present and past research group members, Dr. Ruyi Zheng, Dr. Di Chai, Dr. Gang Yang, and MSc. Yuhao Yang, for their selfless help and sound advice.

Dedications

To my loved parents and siblings. I hope this accomplishment makes you feel proud. To my nephews Aaron, Caleb, and Joshua because their laughs make me feel happier. I hope this work inspires you never to stop fighting for your dreams.

Finally, to my dear husband, Mr. Jose Salazar, who taught me the value of unconditional love.

Table of Contents

List of Figures

List of Tables

Chapter 1: Introduction

1.1. Background

Asphaltenes are an old problem, but unfortunately, not many new effective solutions have been proposed. In 1837 Boussingault defined asphaltenes from experimental observations of distilling residues with asphalt-like properties (Boussingault, 1837). Today, the definition of *asphaltenes* is still a paradox. Asphaltenes are polydisperse fractions, polar, brown to black, classified as a solubility class insoluble in n-pentane or n-heptane, but soluble in toluene, benzene, or xylene (Syed et al., 2012). Researchers know them as the most complex components of crude oil, having the heaviest molecular weight, no melting point, and no unique chemical structure (Mohammadi et al., 2016b; Ortiz et al., 2017). They can be found as a dispersed fraction in the fluid phase, agglomerated-colloidal-viscous liquid phase, or stacked chunk solid particles. The asphaltenes particles have no specific shape, and their complex-vary molecular structure is classified into the island and the archipelago groups. It is experimentally found that the archipelago asphaltene structures are more likely to form clusters, ultimately producing asphaltene deposition.

Asphaltene precipitation and deposition mechanisms are still controversial. However, the colloidal and solubility theories set the foundations for the current asphaltene studies. The colloidal approach postulate that the main forces driving the asphaltene phase behavior are the polar-polar interactions between an asphaltene single-particle and surrounded resins. The perfect equilibrium balance keeps asphaltenes-resins micelles disperse as colloids neighbored by aromatic molecules, which serve as a bridge with saturates (Dickie & Yen, 1967; Leontaritis & Ali Mansoori, 1988; Mitchell & Speight, 1973; Pfeiffer & Saal, 1940). On the other hand, the solubility theory claims that asphaltenes phase behavior obeys the less strong van der Waals forces that keep the

equilibrium of saturates, aromatics, resins, and asphaltenes. In primary oil production, pressure, temperature, or composition changes can disrupt the force balance. While in mature oil reservoirs, gas injection, solvent concentration, or other EOR techniques can cause asphaltene destabilization. The final product of the asphaltene disbalance is its precipitation and, ultimately, its deposition. The deposition of asphaltenes is the culprit of a multimillion-dollar problem for the oil industry. For example, the new forms of oil production, such as deepwater and EOR, where thermodynamic conditions are usually unstable. Therefore, it is crucial to accurately measure, correlate, and predict the asphaltene phase behavior (Soleymanzadeh et al., 2019; Syed et al., 2020).

In the latest years, the experimental measurements of asphaltene phase behavior have accomplished high progress (Afra et al., 2020). Nowadays, many direct and indirect laboratory methods exist for measuring asphaltene behavior. One of them is the high-pressure, high-temperature equipment coupled with a high-resolution microscope that determines the asphaltene onset pressures and the phase behavior analysis of crude oil mixtures at reservoir conditions. However, this state-of-the-art laboratory test is expensive and time-consuming. With that in mind, thermodynamic correlations and simulators that can predict asphaltene change outcomes are urgently required (AlHammadi et al., 2017).

The modeling of asphaltene phase behavior requires a characterization of the asphaltene molecules. In 1967, professors Dickie and Yen postulated that asphaltene could be considered polycyclic aromatic hydrocarbons PAHs, PAH stacks, alkanes, and petroporphyrins. The limitation of this theory is the little consensus on the colloidal and molecular nature of asphaltenes. (Mullins, 2010) proposed a new Yen-Mullins theory where asphaltenes are represented as a single moderated large PHA with peripherical alkanes. These asphaltenes nanoparticles aggregate, forming stacks of a maximum of six PHA structures. The final stage of the aggregation is the

asphaltene cluster, where a minimum of eight single PHA structures can be found stacked. In 1998, Buckley studied the phase behavior of asphaltenes. Later, Hildebrand & Wood, 1933 proposed a thermodynamic model based on the non-polar components of solutions. Huggins, 1942 and Flory, 1944 introduced the polymer equations that successfully predict asphaltene onsets for different solvents. However, the size of asphaltenes is not as much bigger than polymers but bigger than solvent molecules. Hirschberg, 1984 developed the solubility theory, which matches the experimental data of asphaltene precipitation for gas injection and pressure depletion. This model was simplified for different crude oils for De Boer in 1995. It was only until 2010 when Flory, Hugging, and Zuo modified the Hirschberg model and introduced the variations in fluid properties with well-depth (Zuo et al., 2013).

Modeling asphaltene phase behavior using EOS is the second approach of the solubility models. EOS returns to the general thermodynamic concepts, and fewer assumptions are made. PVT properties are used to formulate calculations for predicting asphaltene instability. These models are based on Redlich & Kwong, 1949; Soave, 1972; and Peng and Robinson, 1976. The Cubic Peng Robinson Solid Model was developed for Ngheim in 1993, Nghiem and Coombe in 1997, and Kohse et al. in 2000. The model separates the heaviest component of the oil into a precipitated and non-precipitated fraction. The fraction that precipitates is named the asphaltene solid phase. The other vapor and liquid phases are modeled with the PR-EOS with volume shift parameters. Another recently introduced EOS is the Perturbed-Chain Statistical Associating Fluid Theory (PC-SAFT) EOS developed by Ting et al., 2007; Gonzalez et al., 2008; and Vargas et al., 2009. PC-SAFT successfully predicts asphaltene onsets; however, the method requires the SARA analysis (saturates, aromatics, resins, and asphaltenes). The SARA analysis is costly, increasing the total cost of the tests, and there is still a gap between different lab results (Vargas & Tavakkoli, 2018).

1.2. Objectives

The main objective of this work is to successfully predict the asphaltene precipitation for a CO_2-EOR process under different reservoir conditions throughout the experimental and computational study of asphaltene phase behavior.

The specific objectives are defined by chapters 3 and 4 of this study and are summarized as follows:

- Chapter 3: Successfully measure saturation pressures for oil and gas injection (ethane, propane, and CO_2) systems at reservoir conditions, compare, and model the most affected option by asphaltene precipitation.
- Chapter 4: Experimentally determine the asphaltene content by a well-known standard and corroborate the results using the Solid Detection System (SDS). Measure the Asphaltene Onset Pressures (AOP), analyze the phase behavior and reversibility, and quantify the asphaltene precipitation of the gas-assisted EOR process at different reservoir conditions. Successfully predict asphaltene precipitation using WinProp.

1.3. Thesis Outline

The investigation presented in this thesis comprises the asphaltene phase behavior experimental and modeling analysis for an oil-CO_2 system during an EOR process. The content of the work is divided into five Chapters. The first chapter, Introduction, presents a background of the initial asphaltenes studies, theories, experimental techniques developed to date, and attempts to model their behavior. Chapter 2, Literature Review, summaries the asphaltene problem history and importance, the experimental techniques used for the asphaltene precipitation quantification, and theories developed to date for modeling asphaltene phase behavior. In chapter 3, PVT Analyses, the methodology for measuring oil properties, saturation point, and swelling factors is described in detail. Likewise, the saturation pressure modeling is presented where experimental data is matched with the theoretical model using the WinProp simulator. This model is further used in Chapter 4. Following the asphaltene phase behavior analysis, Chapter 4, Asphaltene Precipitation Prediction, includes the experimental determination of asphaltene content using two methods. The ASTM-3279 establishes the first and second using the Solid Detection System (SDS). The experimental measure of Asphaltene Onset Pressures (AOP), the Phase Behavior and reversibility analyses, and quantification of the asphaltene precipitation are also presented. Finally, the experimental data is modeled in WinProp to predict asphaltene precipitation at different reservoir conditions and CO_2 gas injections. Chapter 5, Conclusions, Limitations, and Future Directions, gives a general approach to the whole work; the most important conclusions of the study are summarized, the limitations encountered in the thesis development are acknowledged, and the future directions are proposed for researchers in the asphaltene field.

Chapter 2: Literature Review

2.1. Asphaltenes Problem

Despite the fact that more than one century has passed since Boussingault introduced the asphaltene concept in 1837. Still, not a unique chemical structure of asphaltene is found, which is the key to solving the puzzle for predicting specific properties, precipitation and deposition mechanisms, and surface activity in crude oil asphaltenes (Hassanzadeh & Abdouss, 2022). This ambiguous definition of asphaltenes is responsible for many problems in the upstream and midstream stages of the oil industry. In addition to the issues associated with asphaltene deposition, such as porous media blockage, changes in rock matrix wettability, or wellbore, near-wellbore, pipes, and equipment plugging, asphaltene precipitation is a culprit among others for creating rigid interfacial films that create asphaltenes-water-oil stabilized super emulsions and inducing an undesirable wax deposition environment (Becker, 1997).

It is well known today that the flow assurance problems caused by asphaltenes flocculation/precipitation/deposition are directly related to changes in reservoir thermodynamic conditions or solvents quality rather than the content of asphaltenes present in the oil composition (Dufour et al., 2010). In fact, there are vast field cases registered where asphaltene problems were reported more often in asphaltene-low-content-light crude oils than in asphaltene-high-content-heavy crude oils. When light components leave the oil system, the intermolecular forces that keep attached saturates, aromatics, resins, and asphaltenes are broken, leading to the agglomeration of asphaltene molecules and finally, the asphaltene deposition problem. Light components are not present in heavy oils, so asphaltene problems are unlikely (Guzmán et al., 2021). In the Gulf of Mexico, the average cost of a well shut-in for asphaltene deposition is US $70 million per well.

This cost can be increased to US $100 million per well when the asphaltene deposition affects the surface-controlled subsurface safety valve (González, 2015).

The CO_2-induced asphaltene precipitation and deposition are significant matters for CO_2-assisted EOR processes in mature fields. The CO_2-EOR process has successfully demonstrated its potential to increase the oil recovery and displacement and nowadays is highly important by offering a bridge for carbon emission reduction (Arnaut et al., 2021). The main limitations of studying asphaltenes problems in the CO_2 flooding process are the inaccuracy in different experimental measuring techniques and the lack of a standard thermodynamic model for simulating asphaltenes precipitation (Daryasafar et al., 2020).

2.2. Experimental Determination of Asphaltene Precipitation

2.2.1 Experimental Techniques

The experimental techniques for determining asphaltene precipitation are divided into indirect and direct methods. Direct methods consider measuring the asphaltene precipitation content after pressure or temperature changes or adding a solvent. These techniques can be performed at ambient conditions or high-pressure and high-temperature simulating reservoir surroundings. *Figure 1* lists the most popular laboratory techniques for determining asphaltenes precipitation. Indirect methods measure the absence of asphaltene precipitation, unlike the direct methods (Tavakkoli et al., 2015)

Direct high-pressure and high-temperature methods are the most reliable. However, these methods are costly, have time-consuming procedures, and highly qualify-trained personnel is needed.

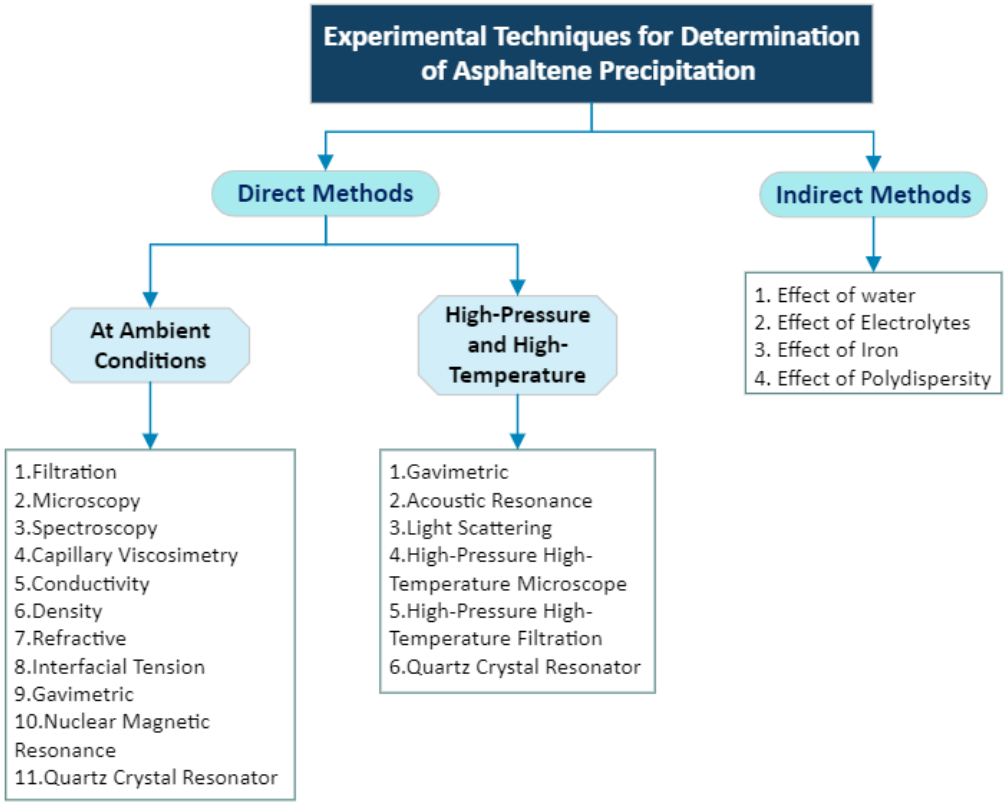

Figure 1. Experimental techniques for asphaltene precipitation

2.2.1.1. High-Pressure and High-Temperature Microscope

In this work, a high-pressure, high-temperature high-resolution microscope is used. This microscope is part of a Solid Detection System (SDS) coupled with a PVT cell where the bubble points are measured.

Many SDS apparatuses are usually used with the light scattering technique (LST) to verify the onset pressure. In this study, the SDS does not have LST. The SDS provides particle size analysis software used to determine the amount of asphaltene precipitation. Additionally, the high-magnifying capacity of the microscope allows for identifying the asphaltene phase behavior giving enough information for verifying the reversibility of the process.

Many investigations have been published for analyzing asphaltene precipitation using a HPHT microscope. Most of them are for primary production and for testing the use of chemical inhibitors (Ghloum et al., 2019; Karan et al., 2003; Mohammadi et al., 2016a), but only a few of them are related to asphaltene precipitation induced by CO_2 during EOR processes (Espinoza Mejia et al., 2022; Zanganeh et al., 2012).

The limitation of this technique is the time and expertise required by the lab worker before starting the experiment. It requires at least 12 hours per measured point, including cleaning and setting up all SDS and PVT cell equipment. Another constraint for this procedure is that the microscope cannot detect particles in dark oils or oils with high asphaltene content. A solvent or an indirect method must be used in these cases. The advantage of the HPHT microscope is that this procedure gives a direct and real-time measurement. It provides good images to analyze phase behavior and reversibility of the process, especially for the CO_2-EOR process.

The SDS and PVT cell use in this experimental work is provided in sections 3.3.2 and 4.3.2. For this experimental work, the SDS and PVT do not have an LST associated that helps verify the asphaltene onset pressures (AOP). For this reason, the AOP pressures and their respective asphaltene precipitation were modeled using commercial software.

2.3. Asphaltene Precipitation Modelling

2.3.1 Asphaltene Phase Behavior

The asphaltene phase behavior envelope in *Figure 2* is represented by a pressure-temperature diagram for an oil reservoir. Above the Upper Asphaltene Boundary, only the liquid phase is found. Here, asphaltenes and light components are dissolved into the crude oil phase. Due to the depletion of the reservoir, asphaltene molecules start agglomerating, forming stacks and finally clusters that precipitate, creating two phases solid asphaltenes and liquid crude oil. This point is the Upper Asphaltene Boundary. The amount of asphaltenes particles reaches a maximum when the pressure is the bubble point. All light components leave the liquid phase at the saturation point, creating a three-phase environment, solid asphaltenes, liquid oil, and light vapor components. Since the light components left the oil phase, the heavy-rich components of the oil become a suitable solvent for asphaltenes again. Asphaltene particles will be redissolved into the oil phase until the last asphaltene particle comes into the solution at the Lower Asphaltene Boundary. Points 1 to 5 in Figures 2 and 3 represent an isothermal depressurization process.

For the case of the CO_2-EOR, the phase behavior also encounters similar characteristics to a primary depleted oil reservoir, a single-phase (liquid oil and CO_2) at miscible conditions, two phases (liquid oil and CO_2 and solid asphaltenes) at UAOP, three phases (liquid oil and gas CO_2 and solid asphaltenes) at bubble point, and two phases (liquid oil and gas CO_2) below LAOP. *Figure 3* describes all these phases of a depressurization process, showing the percentage of asphaltene precipitation per area% for a fixed fraction of CO_2 gas injected into an oil sample. Images are taken from an HPHT microscope under reservoir conditions.

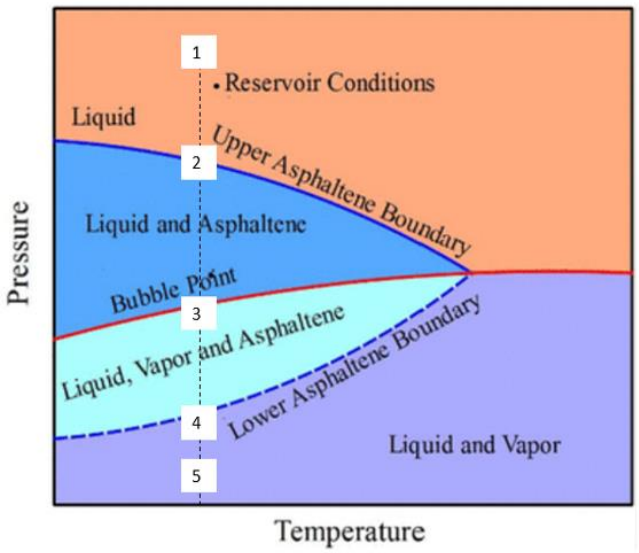

Figure 2. Asphaltene phase envelope, pressure-temperature diagram.
(Adapted from "Asphaltenes – problematic but rich in potential" by (Akbarzadeh et al., 2007), *Oilfield Review, 19,* p. 28.)

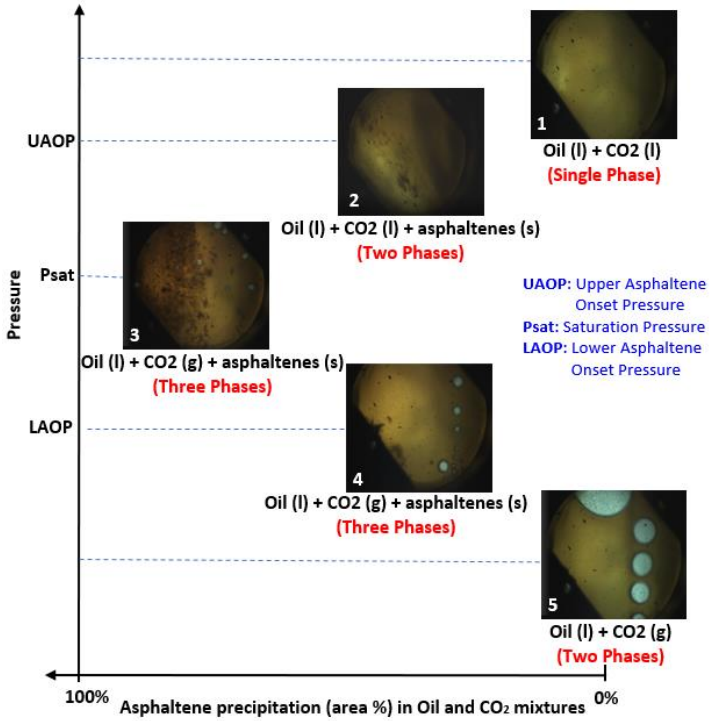

Figure 3. Asphaltene phase behavior, pressure-asphaltene precipitation diagram.
(Adapted from "Experimental Study of Asphaltene Precipitation and Deposition During Immiscible CO_2 - EOR Process" by Espinoza et al., 2022, *SPE,* p. 10.)

2.3.2 Reversibility Mechanisms

The asphaltene precipitation process is a reversible process under specific conditions. Asphaltene precipitation and its further deposition depend on temperature, pressure, and composition of the light components present in the oil. Initially, asphaltenes particles are dissolved into the oil phase as asphaltene nano-particle; at this thermodynamic condition, asphaltenes are stabilized by resins which are polar molecules like asphaltenes, resins surround every asphaltene particle, and these at the same time are surrounded by aromatic molecules creating the perfect equilibrium, *Figure 4*. *Figure 5* shows that the asphaltene equilibrium is broken due to operational and reservoir factors. Asphaltene particles attach when the equilibrium is broken, forming stacks; these primary particles aggregate with others forming microaggregates. The HPHT microscope will identify these particles as asphaltene precipitation. According to many studies at this point, the asphaltene formation mechanism is reversible, which means asphaltenes clusters can be redissolved again into the oil phase if the initial conditions are reestablished. However, there is a point in temperature, pressure, or light components composition where a portion of asphaltenes particles will not go back into the oil phase and will remain as solids even though the initial conditions are reestablished. The aging process is where asphaltene solid particles will start forming asphaltene deposition. At this stage, no thermodynamic changes can help dissolve these solids again into the oil phase causing blockage of the porous media and affecting the permeability and wettability of the matrix rock, *Figure 6*.

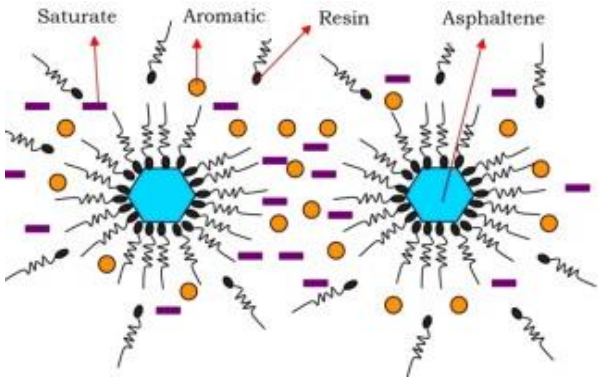

Figure 4. Force balance on asphaltenes.
(Adapted from "The relationship between SARA fractions and crude oil stability" by (Ashoori et al., 2017), Egyptian Journal of Petroleum, 26, p.212.)

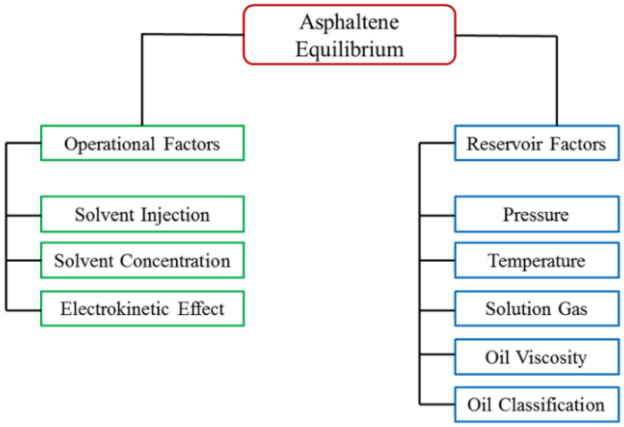

Figure 5. Factors affecting asphaltene equilibrium.
(Adapted from "Critical review of asphaltene properties and factors impacting its stability in crude oil" by (Fakher et al., 2020), Journal of Petroleum Exploration and Production Technology, 10, p.1190.)

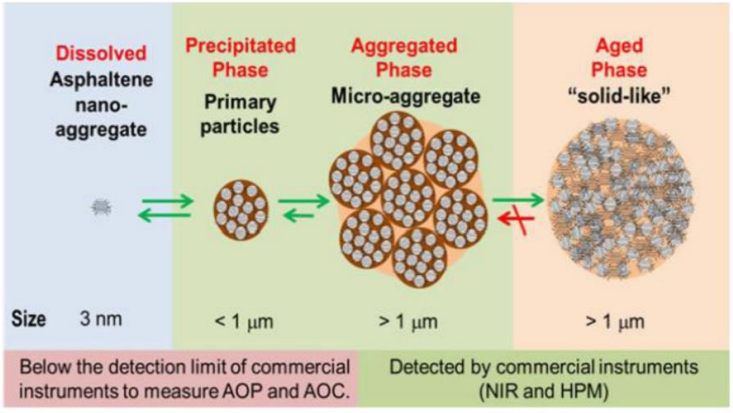

Figure 6. Asphaltene precipitation, aggregation, and aging mechanism.
(Adapted from "Asphaltene Deposition" by (Vargas & Tavakkoli, 2018), CRC Press Taylor and Francis Group, p.7.

2.3.3 Thermodynamic Models

Due to the ambiguous definition of asphaltenes and the complexity of their structures, experimental achievements for determining accurately and cost-effectively asphaltene precipitation is still limited. For that reason, there is necessary to develop thermodynamic relationships that can predict the behavior of asphaltene precipitation in terms of independent variables such as pressure, temperature, and composition of the components in the crude oil. These PVT relationships have been studied for many years; however, no unique model has been developed to predict uniformly asphaltene results for crude oils and all types of solvent injections. The most popular theories postulate asphaltene precipitation models are the Solubility and Colloidal models. The Colloidal model assumes that asphaltenes are micelles stabilized by polar-polar interaction with resins. Under this approach, if the concentration of resins/asphaltenes is too low, asphaltenes precipitate from the bulk phase. In the second group, the solubility models, it is believed that asphaltenes are soluble in the oil phase either partially or totally. A solubility parameter is defined and will depend on the weak van der Waals interaction forces rather than the colloidal model's solid polar-polar interactions (Khaleel et al., 2015; Tavakkoli et al., 2016).

Figure 7 shows a classification of the asphaltene precipitation thermodynamic models. The Solubility models are divided into two main groups, the solution theories and the Equations of State (EOS). For the solution theory, the crude oil is assumed to be a binary mixture. Asphaltene is treated as the solute and the rest of the mixture as the asphaltene solvent. In the EOS case, the model uses the multiphase equilibrium formulation introduced by Michelsen

(1982). The PT-flash and the EOS outputs can be manipulated to match the experimental data by tuning the asphaltene model parameters.

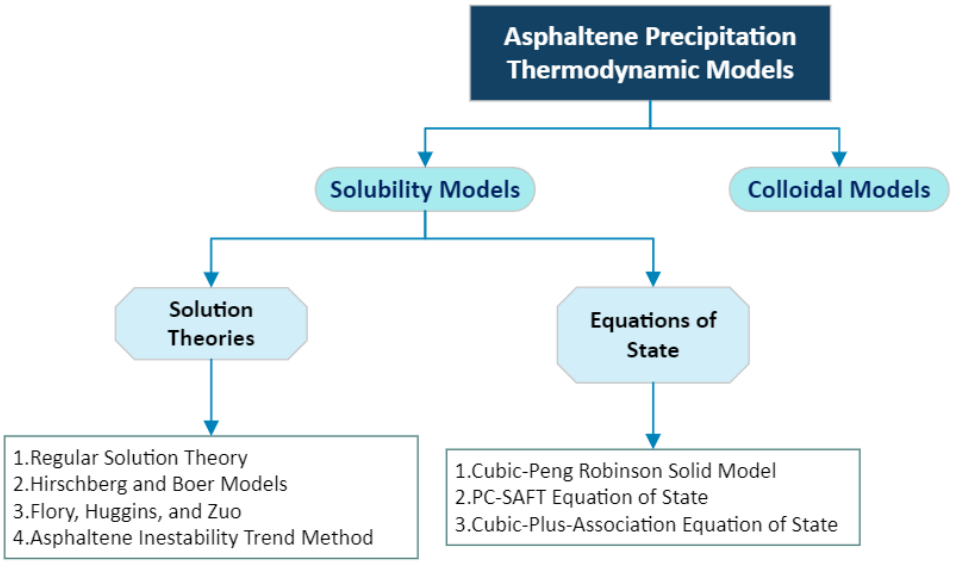

Figure 7. Asphaltene precipitation thermodynamic models

2.3.3.1. Cubic-Peng Robinson (PR) Solid Model

The thermodynamic model used in WinProp to predict asphaltene precipitation was developed for Ngheim in 1993, Nghiem and Coombe in 1997, Ngheim et al., 1993, and Khose et al. in 2000. In this model, the asphaltene phase can be considered a solid, partially solid, or viscous fluid. The model separates the heaviest component of the oil into a precipitated and non-precipitated fraction. The fraction that precipitates is named the asphaltene solid phase. The other vapor and liquid phases are modeled with the PR-EOS with volume shift parameters. The solid model used in WinProp has several assumptions which reduce its computational time. The assumptions are listed as follows (Subramanian et al., 2016):

- Homogeneous asphaltene behavior
- Molecular interactions are not counted for
- Reversible asphaltene precipitation, although this can be modified
- Asphaltene molecular structure or geometry is not considered

At least one point for PVT and AOP experimental data are needed to adjust the solid model parameters.

The parameters to be estimated for using the model are:

- The fugacity of the pure asphaltene at a reference pressure
- The molar volume of the solid
- The volume shift parameter
- The interaction coefficient between the asphaltene components and other components

The procedure used in the solid model is described as follows:

- Fluid characterization of the oil and the solvent
- Regression to match fluid PVT data
- Specification of asphaltene component parameters
- Validation of asphaltene component parameters with isothermal experimental data
- Determination of the solid model parameters for non-isothermal conditions
- Prediction of Asphaltene Precipitation Envelope (APE)

The reliability has been demonstrated in many field cases (Al-Qasim, 2017; Ghasemi & Al-Safran, 2020; Zadeh et al., 2011). However, not all cases can be reproduced with total success. For that reason, some improvements have been proposed to improve the model's accuracy (Shoukry et al., 2020).

A more extended explanation of the solid model used in this work is presented in *section 4.5.2, Mathematical Modeling*.

Chapter 3: PVT Analyses

3.1 Introduction

All crude oils contain asphaltenes in their composition. The content of asphaltenes does not determine whether or not asphaltenes will precipitate. This complex thermodynamic equilibrium depends on the pressure, temperature, and composition of the crude oil components. For gas-assisted EOR processes, solvent injection ratios directly affect the asphaltene precipitation. There is a close interrelationship between asphaltene precipitation and the PVT analysis. Through PVT analysis, saturation points and swelling factors can be determined. At saturation point, the maximum asphaltene precipitation is reported while the swelling factor measures the oil expansion, impacting oil recovery and displacement. This chapter addresses the PVT analyses by measuring saturation pressures and swelling factors for five oil samples at reservoir temperatures and various gas injection fractions. The experimental work compares the saturation pressures and swelling factors for ethane, propane, and CO_2 injection fractions. Initially, the oil properties are required; *section 3.2 Crude Oil Properties* presents these measurements. Results from the experiments are shown in *section 3.3 Saturation Pressures and Swelling Factors Measurements*. It is desired to simulate the experimental saturation pressures of crude oil #5 and CO_2 mixtures using WinProp (CMG, 2011). Therefore, *section 3.4, Saturation Pressure Simulation,* explains the mathematical modeling, simulation results, and regression of the experimental data to obtain the best-simulated saturation pressures. This chapter concludes that the software accurately predicts the saturation pressures of crude oil #5 and CO_2 mixtures; these results are used for further asphaltene precipitation prediction.

3.2 Crude Oil Properties

3.2.1. Density

The density and API gravity are measured for all crude oils #1-5 using the densimeter DMA 4500 from Anton Paar. This digital density meter is based on the oscillating U-tube principle. The U-shaped glass tube is excited and starts oscillating at a certain frequency. When the tube is filled with the sample, this frequency changes; the sample density is calculated based on this measured frequency. The measuring range of the densimeter is 0 to 3 g/cm^3. Density and temperature accuracies are ± 0.00005 g/cm^3 and ± 0.03 °C, respectively. Likewise, the density and temperature repeatability or standard deviations are 0.00001 g/cm^3 and 0.01 °C, respectively. A minimum sample of 1 ml can be used (Anton Paar, 2022).

First, the checking procedure, adjustment, and calibration for air and distilled water must be performed. Then, cleaning the measuring cell with toluene and acetone must be performed. Toluene removes the residues, acetone removes the remaining toluene, and it is easily evaporated during the drying process. The drying process is performed by a stream of dry air available in the densimeter. Now, the densimeter is ready for measuring.

In the instrument, activate the method "Crude Oil." Set the desired temperature and inject 1 ml of oil sample. A typical measuring time per sample is approximately 30 seconds. Change the new temperature to continue with the subsequent measurement. When the samples need to be changed, the adjusting, cleaning, and drying procedures must be repeated before starting the new measurement (Du, 2018).

Figure 8. Densimeter DMA 4500, Anton Paar

Table 1 shows the density measurements for crude oils #1-5.

Table 1. Density and API gravity for crude oils #1-5

Crude oil #	**Density, g/cm^3 at 15.5 °C**	**° API at 15.5 °C**
1	0.8457	35.1
2	0.8812	28.595
3	0.8276	38.96
4	0.8043	43.9
5	0.836	37.829

The PVT experiments for crude oils #1-4 are performed at a single reservoir temperature. Whereas, for the case of crude oil#5, five different reservoir temperatures were analyzed. For that reason, the density measurements for crude oil #5 were performed at different temperatures. Results are reported in *Figure 9* and *Figure* 10.

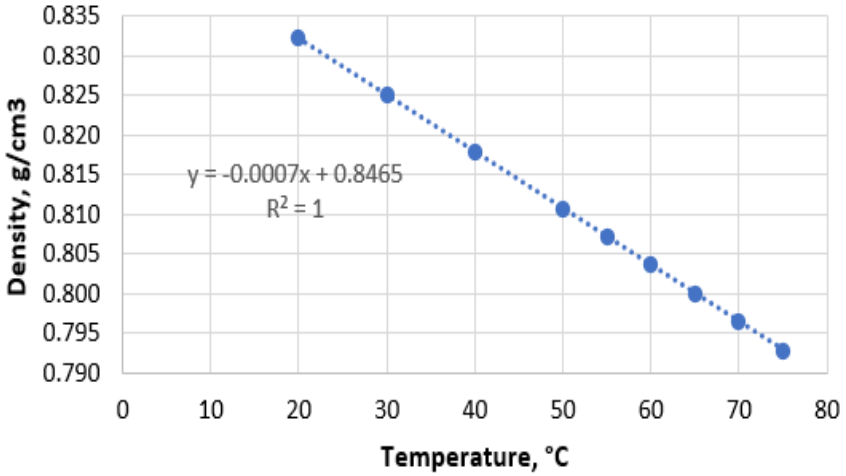

Figure 9. Density measurements for crude oil #5 at different temperatures

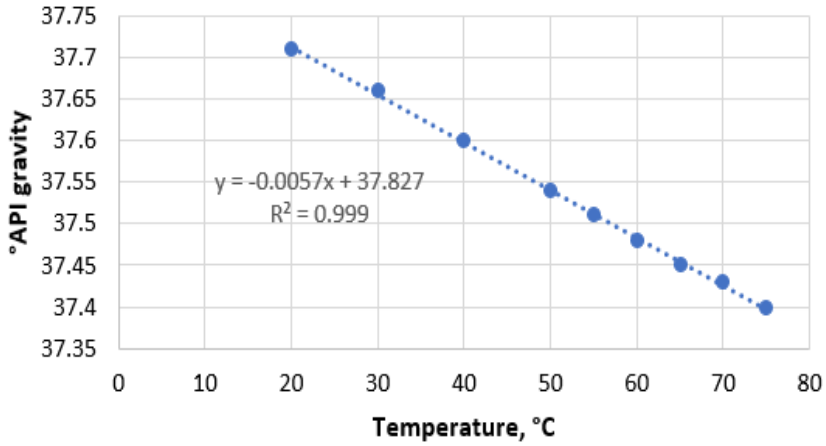

Figure 10. API gravity measurements for crude oil #5 at different temperatures

Crude oil #5 has a measured density and °API of 0.836 g/cm^3 and 37.829 at 15.5 °C, respectively.

3.2.2. Molecular Weight

The molecular weight is indirectly measured for crude oils #1-5 using the wide range cryoscope Cryette WR from Precision Systems. The freezing point depression of the solution (oil as solute and benzene as solvent) measured in the cryoscope is in direct proportion to the concentration of the solute. After accurately weighing portions of solvent and solute, the freezing points are measured, and at least two readings are required to calculate the solute average molecular weight using *Equation 1* (ASTM-D02 Committee, 2008). *Table 2* shows the molecular weight measurements for crude oils #1-5.

$$MW = \frac{1000KU}{\Delta TV} \qquad \text{Equation 1}$$

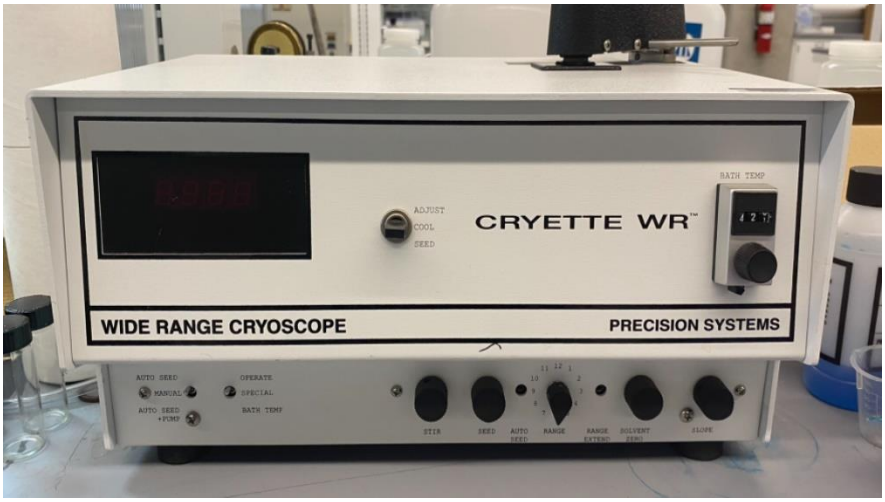

Figure 11. Cryoscope Cryette WR, Precision Systems

Table 2. Molecular weight for crude oils #1-5

Crude oil #	Molecular weight, g/mole
1	212.28
2	230
3	255
4	191
5	209.91

3.2.3. Viscosity

The viscosity is measured only for crude oil #5 since the PVT experiment will be performed at different temperatures. A viscosimeter DV-II + Pro from Brookfield is used; this rotational viscosity meter measures dynamic viscosity as the ratio of shear stress to share rate. The oil sample is placed in a cup where a spindle is inserted. The spindle rotates at fixed rates, defined as "shear rates." Simultaneously the viscometer measures the torque resistance at each spindle rotation, described as "shear stress." The temperature sensing range of the viscosimeter is -100 °C to 300 °C. The reported viscosity and temperature accuracy are ± 1.0 % of the full-scale range and ± 1 °C from -100 °C to +149 °C or ± 2 °C from -150 °C to +300 °C, respectively. The viscosity repeatability is ± 0.2 % of the full-scale range. The operating environment temperature range and relative humidity are 0°C to 40°C and 20% to 80% for a non-condensing atmosphere (Brookfield, 2022).

Initially, the viscometer cup and spindle must be clean. Toluene removes the residues, acetone removes the remaining toluene, and it is easily evaporated. A stream of dry air available in the lab is used to dry the cup and spindle. Then, the cup and spindle are assembled, and the instrument is turned on, leveled, and autozeroed. The next step is to set the gap and proceed with the calibration. The calibration fluid should be carefully chosen for the sample viscosity ranges. After the calibration, the viscosimeter is ready for measuring. The cup and spindle must be clean and dry. The gap must be set. 0.5 ml of crude oil #5 is charged in the cup. The desired temperature is set in the thermo-cooling bath. The shear rate is set in rpm. The viscosimeter motor is turned on and allowed to show a constant value of viscosity and temperature on the screen. The viscosity, shear rate, and torque are recorded. The procedure is repeated for other temperatures and share rates. When the samples need to be changed, the

cleaning, drying, leveling, autozeroing, and calibration must be performed before starting the new measurements (Yang, 2020). *Figure 12* shows the viscosity results for crude oil #5 at different temperatures.

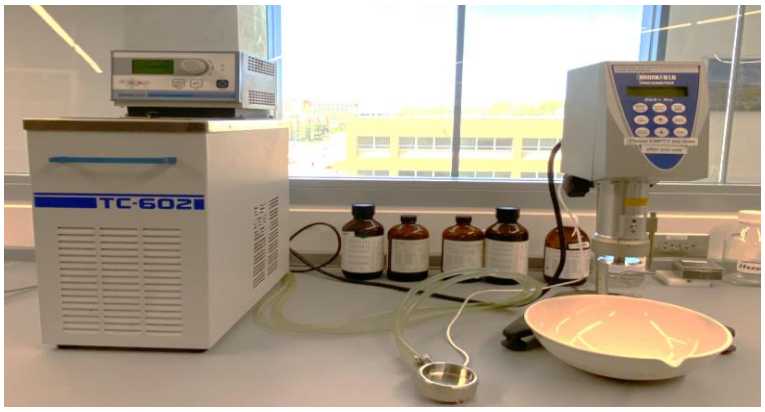

Figure 12. Viscosimeter DV-II + Pro, Brookfield with Thermo-cooling Bath TC-602

Crude oil #5 has a measured viscosity of 7.192 cP at 15.5 °C.

3.2.4. Summary

The crude oils #1-5 density, °API, and molecular weight were measured in the lab. Viscosity

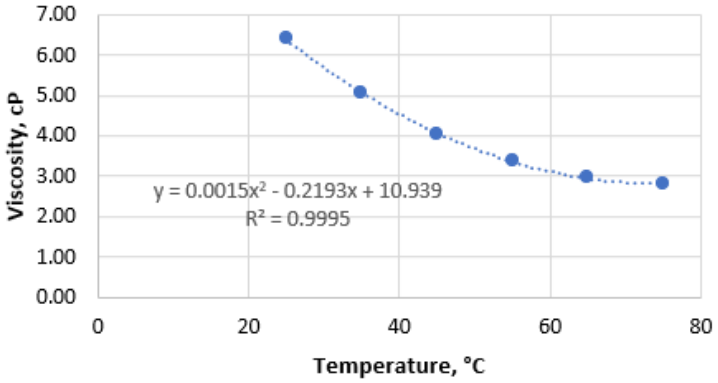

was measured only for crude oil #5 since the PVT analyses will be performed at different temperatures. The crude oil #5 viscosity at 15.5 °C is reported as 7.192 cP.

3.3 Saturation Pressures and Swelling Factors Measurements

3.3.1. Materials

Five oil samples were investigated to determine their saturation points and swelling factors at different reservoir temperatures. The density, °API, molecular weight, and viscosity are presented in *section 3.2, Crude Oil Properties*. The gases propane, ethane, and CO_2 used as solvents have purities of 99.9999 %, 99.9999 %, and 99.999% (Matheson, USA), respectively. *Table 3* shows the feeds prepared for crude oils #1-4 and propane injections, *Table 4* shows the feeds prepared for ethane injections, and *Table 5* shows the feeds prepared for crude oil #5 and CO_2 injections.

Table 3. Feeds prepared for propane and crude oils #1-4

Crude oil #	Feed #	Propane-mole%	Oil-mole%	Temperature, °C
1	**1**	68.76	31.24	42.2
	2	55.69	44.31	
	3	46.81	53.19	
	4	40.38	59.62	
	5	35.50	64.50	
	6	31.67	68.33	
	7	28.59	71.41	
	8	26.05	73.95	
2	**1**	20	80.00	104.4
	2	30	70.00	
	3	40	60.00	
	4	50	50.00	
	5	60	40.00	
3	**1**	20	80.00	73.3
	2	30	70.00	
	3	40	60.00	
	4	50	50.00	
	5	60	40.00	
4	**1**	20	80.00	104.4
	2	30	70.00	
	3	40	60.00	
	4	50	50.00	
	5	60	40.00	

Table 4. Feeds prepared for ethane and crude oils #1-4

Crude oil #	Feed #	Ethane-mole%	Oil-mole%	Temperature, °C
1	**1**	64.57	35.43	42.2
	2	52.23	47.77	
	3	43.85	56.15	
	4	37.79	62.21	
	5	33.20	66.80	
	6	29.60	70.40	
	7	26.71	73.29	
2	**1**	20	80.00	104.4
	2	30	70.00	
	3	40	60.00	
	4	50	50.00	
	5	60	40.00	
3	**1**	20	80.00	73.3
	2	30	70.00	
	3	40	60.00	
	4	50	50.00	
	5	60	40.00	
4	**1**	20	80.00	104.4
	2	30	70.00	
	3	40	60.00	
	4	50	50.00	
	5	60	40.00	

Table 5. Feeds prepared for CO_2 and crude oil #5

Crude oil #	Feed #	CO_2-mole%	Oil-mole%	Temperature, °C
5	**1**	25	75	25, 60, 90, 120, 150
	2	30	70	
	3	35	65	
	4	40	60	
	5	45	55	
	6	50	50	

3.3.2. Experimental Setup

Many investigations have confirmed that the maximum asphaltene precipitation content is found at the saturation pressure (Pedersen et al., 2015; Yen & Chilingarian, 1994, 2000). Therefore, it is essential to measure this property before conducting asphaltene precipitation experiments. The method used for measuring saturation pressure (bubble point) for an oil sample in a mixture with gas injection is called Constant Composition Expansion (CCE), and it is performed in a PVT cell.

This work uses a piston-equipped PVT cell system (PVT 300/700 FV, Core Lab) for all the bubble point and swelling factor measurements. A schematic representation of the PVT cell system is shown in *Figure 13*. The PVT cell has a maximum volume of 300 ml. The operational range of pressure and temperature is from 0 psi to 10,150 psi and from -10 °C to 200 °C, respectively. The temperature inside the PVT cell is controlled by an internal heating source and an external heating-cooling bath. A magnetic stirrer is activated for volumes higher than 25 ml to accelerate the equilibrium state inside de PVT cell. The piston is moved forward and backward for volume control and pre-and-depressurized the system inside the cell. In-situ pressure and temperature sensors provide reliable data with an accuracy of ± 0.35% Full Scale and ± 0.1 °C, respectively. A charged-couple device (CCD) digital 6M pixels video camera allows the visualization of the phase behavior changes during the whole experiment. Falcon and Euclide software will also record the experimental pressure, temperature, and volume (Zheng, 2020).

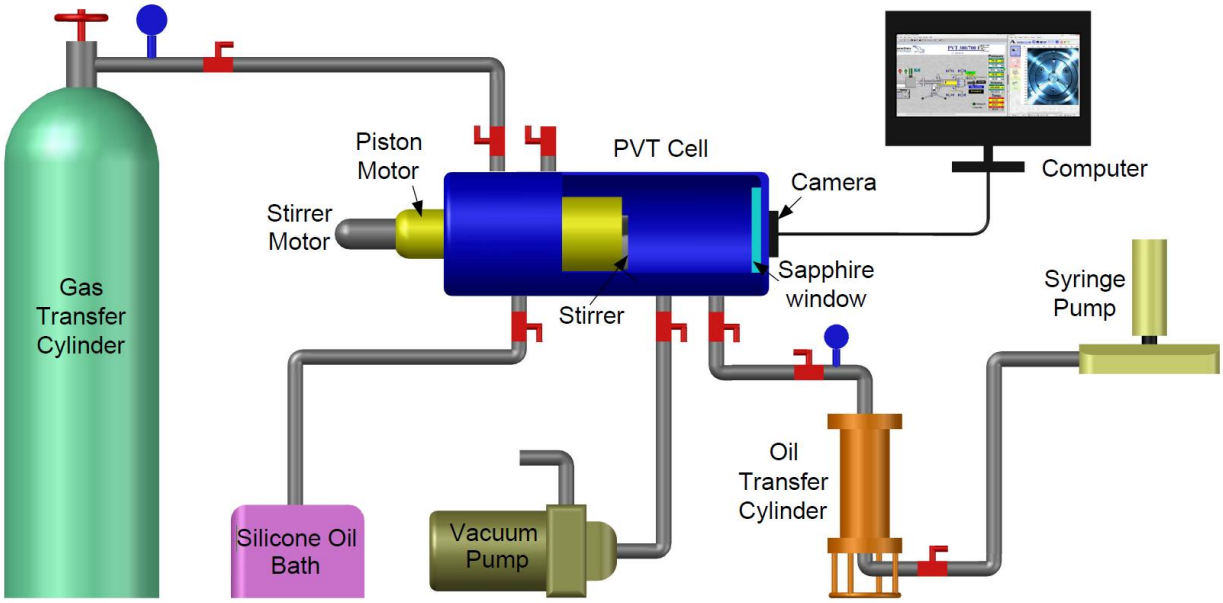

Figure 13. Schematic diagram of the experimental setup for the PVT system

3.3.3. Experimental Procedure

The experimental procedure starts with preparing the equipment. Before beginning the CCE experiment, the PVT cell must be cleaned and vacuumed adequately. The cleaning process is conducted by washing the cell with toluene, then with acetone, both three times. The vacuum process is successful when at a volume of 25 ml, the pressure in the cell remains constant at around 0 and -3 psia for 30 minutes. If this condition is not reached, a new assembly of tubing and valves must be performed. Afterward, the oil sample is injected into the PVT cell. The volume of the cell is fixed before starting the gas injection. This volume and the final pressure of the system after the gas injection are previously calculated. The gas is now injected into the cell from a pressurized cylinder. The injection process will finish when the pressure calculated previously is reached in the system. The oil sample will always be fixed, and a new fraction of gas is injected for the next feed. For every CCE experiment, the temperature is constant.

Two phases (oil in liquid and gas in vapor) can be observed through the PVT camera. The pressure is now increased until the mixture becomes one single phase. In this condition, a slight volume change will produce a significant pressure difference; this is explained because the mixture is incompressible in the liquid phase. The CCE experiment can start when the single-phase is reached, and the system is in equilibrium, so there is no change in pressure and temperature for some hours.

The CCE experiment is performed by depressurizing the system at equilibrium conditions. The cell piston is moved backward at a very low rate (3ml/h) to ensure the equilibrium condition. Changes in pressure versus volume are recorded in the Falcon software. The pressure versus volume trend will be displayed as a straight line with a fixed slope until a sharp inflection point is shown. After the inflection point, a new straight line is shown with a constant slope which describes the oil liquid and gas vapor phases at liquid-vapor equilibrium. The intersection of these two straight lines is the point of the bubble point pressure and the swollen oil volume.

As an illustrative example, *Figure 14* shows the pressure versus volume data obtained from the CCE experiment for the Crude oil #5 and CO_2 mixture at 90 °C. For this case, the bubble point pressure is 574.89 psia, and the swollen oil volume is 29.44 ml.

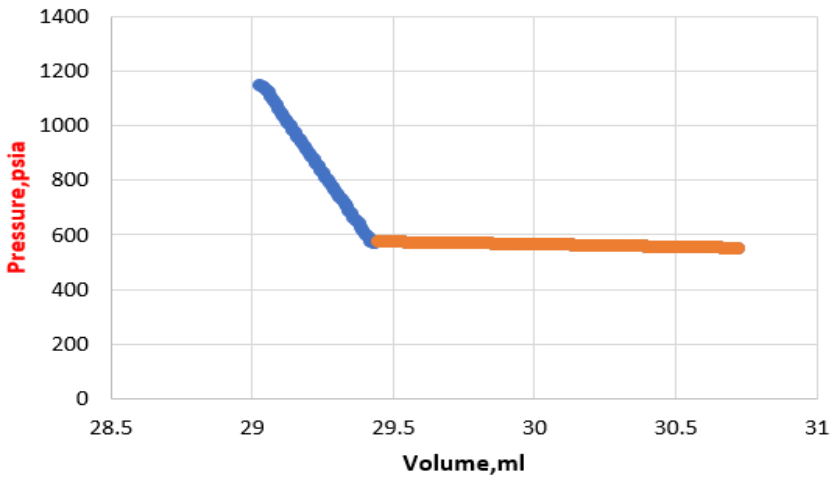

Figure 14. Pressure versus swollen oil volume for crude oil #5 and 25 mole% CO_2 injection

The next composition of gas injection is injected into the PVT cell, and the depressurization process is repeated. The procedure should start again from the cleaning and vacuum process to repeat the experiment with another gas. The results quality will depend on the equilibrium state's assurance before starting the depressurization process. Fifty-one (51) experiments were performed for five crude oil samples at various reservoir conditions.

3.3.4. Experimental Results

Saturation pressure (Psat) measurements and swelling factor (SF) calculations are listed forward for crude oils #1-4 with injections of propane and ethane at reservoir temperature and for crude oil #5 with injections of CO_2 at different reservoir temperatures (T reservoir).

3.3.4.1. Crude oil #1

Table 6. Saturation pressure and swelling factor for propane - crude oil #1

Crude oil	#1			
T reservoir	42.2 °C			
°API	35.8			
Feed #	**Propane-mole%**	**Oil-mole%**	**Psat, psi**	**SF, psi**
1	68.76	31.24	**140.23**	**1.55**
2	55.69	44.31	**123.24**	**1.24**
3	46.81	53.19	**113.33**	**1.11**
4	40.38	59.62	**110**	**1.06**
5	35.50	64.50	**98.53**	**1.02**
6	31.67	68.33	**96.31**	**1.02**
7	28.59	71.41	**86.18**	**1.00**
8	26.05	73.95	**85.57**	**0.09**

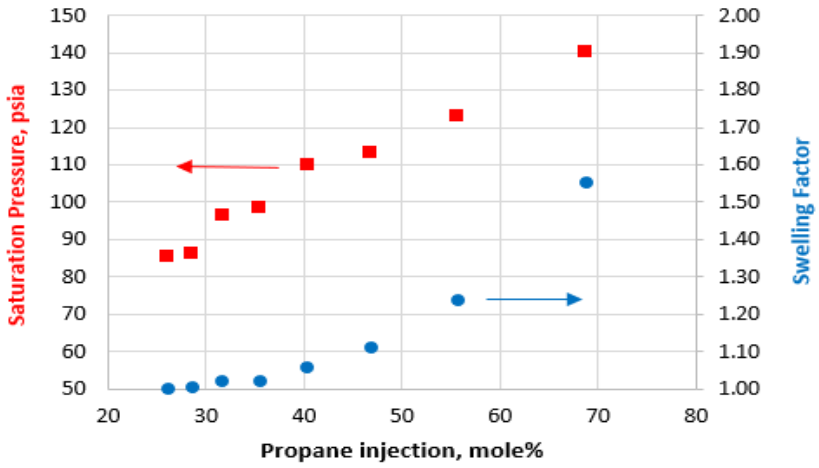

Figure 15. Saturation pressure and swelling factor versus propane injection for crude oil #1

Table 7. Saturation pressure and swelling factor for ethane - crude oil #1

Crude oil	crude oil #1			
T reservoir	42.2 °C			
°API	35.8			
Feed #	**Ethane-mole%**	**Oil-mole%**	**Psat, psi**	**SF, psi**
1	64.57	35.43	**506.76**	**1.58**
2	52.23	47.77	**394.66**	**1.35**
3	43.85	56.15	**323.49**	**1.24**
4	37.79	62.21	**273.01**	**1.24**
5	33.20	66.80	**237.18**	**1.15**
6	29.60	70.40	**208.7**	**1.12**
7	26.71	73.29	**187.03**	**1.11**

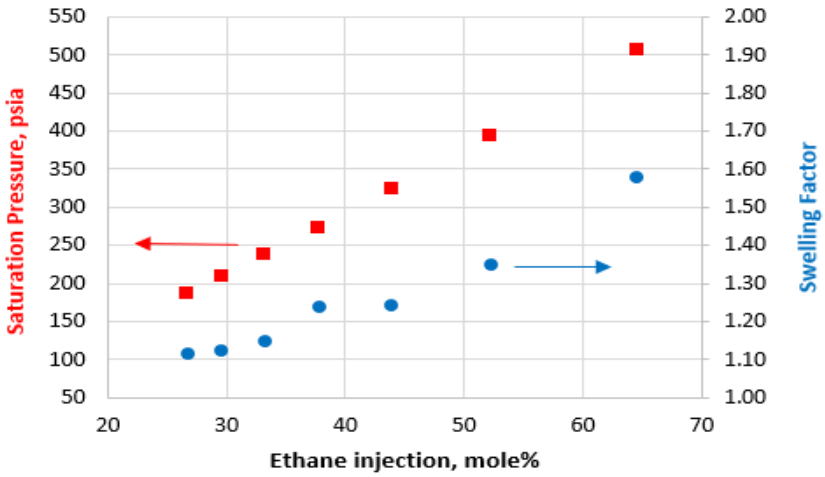

Figure 16. Saturation pressure and swelling factor versus ethane injection for crude oil #1

3.3.4.2. Crude oil #2

Table 8. Saturation pressure and swelling factor for propane - crude oil #2

Crude oil	crude oil #2			
T reservoir	104.4 °C			
°API	29.07			
Feed #	**Propane-mole%**	**Oil-mole%**	**Psat, psi**	**SF, psi**
1	20	80.00	**168.51**	**1.02**
2	30	70.00	**213.1**	**1.26**
3	40	60.00	**268.31**	**1.38**
4	50	50.00	**336.94**	**1.53**
5	60	40.00	**404.62**	**1.77**

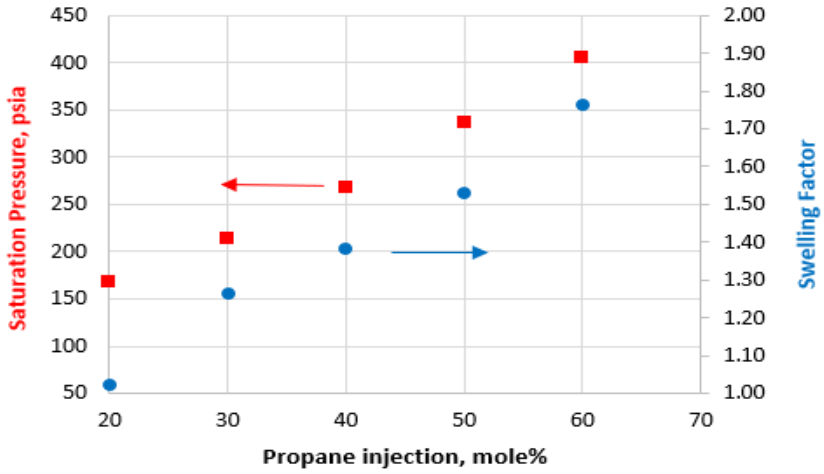

Figure 17. Saturation pressure and swelling factor versus propane injection for crude oil #2

Table 9. Saturation pressure and swelling factor for ethane - crude oil #2

Crude oil #	2			
T reservoir	104.4 °C			
°API	29.07			
Feed #	**Ethane-mole%**	**Oil-mol%**	**Psat, psi**	**SF, psi**
1	20	80.00	**357.11**	**1.12**
2	30	70.00	**659.75**	**1.21**
3	40	60.00	**795.85**	**1.26**
4	50	50.00	**1067.32**	**1.35**
5	60	40.00	**1171.52**	**1.43**

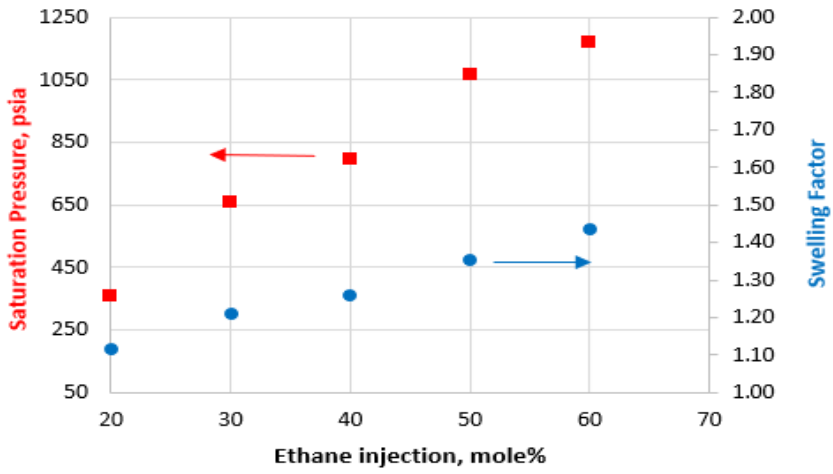

Figure 18. Saturation pressure and swelling factor versus ethane injection for crude oil #2

3.3.4.3. Crude oil #3

Table 10. Saturation pressure and swelling factor for propane - crude oil #3

Crude oil #	3			
T reservoir	73.3 °C			
°API	39.47			
Feed #	**Propane-mole%**	**Oil-mole%**	**Psat, psia**	**SF, psi**
1	20	80.00	**77.9**	1.13
2	30	70.00	**111.5**	1.20
3	40	60.00	**147.68**	1.27
4	50	50.00	**190.26**	1.39
5	60	40.00	**231.24**	1.56

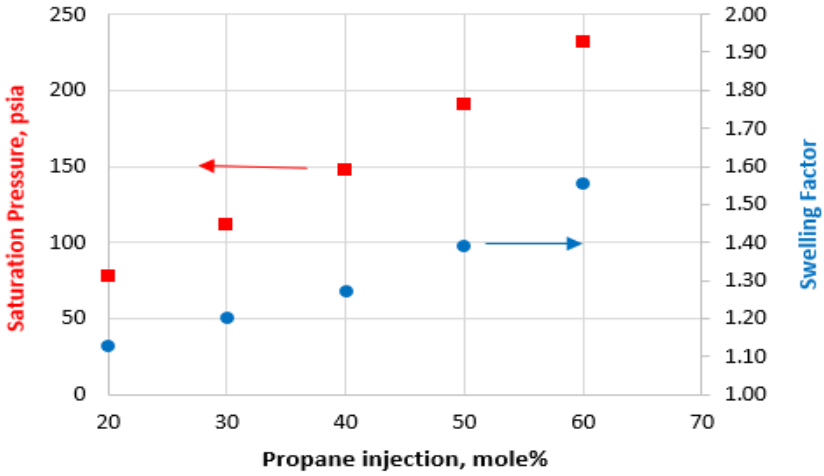

Figure 19. Saturation pressure and swelling factor versus propane injection for crude oil #3

Table 11. Saturation pressure and swelling factor for ethane - crude oil #3

Crude oil #	3			
T reservoir	73.3 °C			
°API	39.47			
Feed #	**Ethane-mole%**	**Oil-mole%**	**Psat, psia**	**SF, psi**
1	20	80.00	**221.73**	**1.07**
2	30	70.00	**344.64**	**1.12**
3	40	60.00	**468.59**	**1.20**
4	50	50.00	**608.71**	**1.29**
5	60	40.00	**754.4**	**1.42**

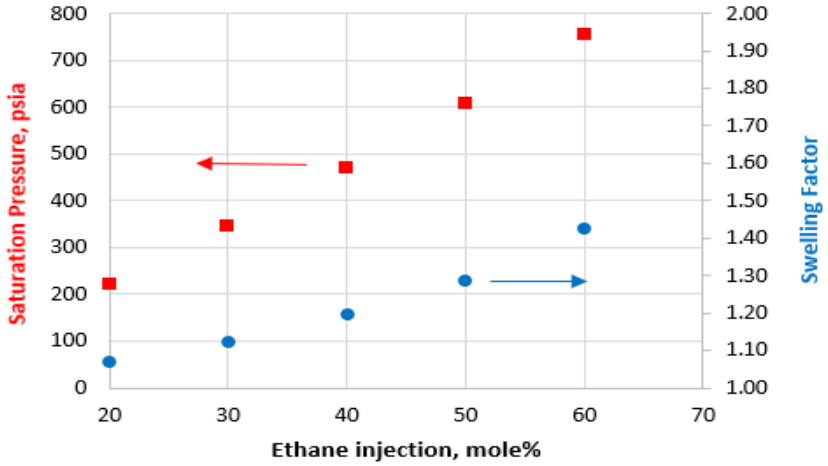

Figure 20. Saturation pressure and swelling factor versus ethane injection for crude oil #3

3.3.4.4. Crude oil #4

Table 12. Saturation pressure and swelling factor for propane - crude oil #4

Crude oil #	4			
T reservoir	104.4 °C			
°API	44.43			
Feed #	**Propane-mole%**	**Oil-mole%**	**Psat, psi**	**SF, psi**
1	20	80.00	**80.69**	**1.137**
2	30	70.00	**106.94**	**1.206**
3	40	60.00	**135.32**	**1.295**
4	50	50.00	**163.69**	**1.446**
5	60	40.00	**194.65**	**1.624**

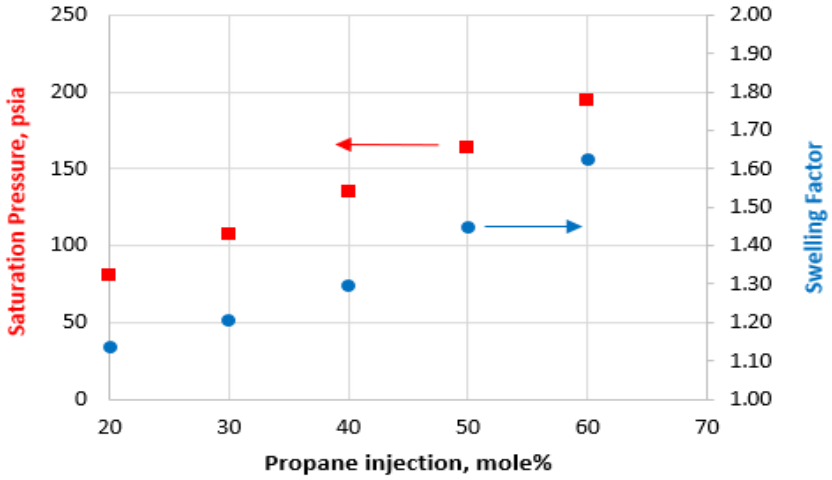

Figure 21. Saturation pressure and swelling factor versus propane injection for crude oil #4

Table 13. Saturation pressure and swelling factor for ethane - crude oil #4

Crude oil #	4			
T reservoir	104.4 °C			
°API	44.43			
Feed #	**Ethane-mole%**	**Oil-mole%**	**Psat, psi**	**SF, psi**
1	20	80.00	**224.05**	**1.108**
2	30	70.00	**359.28**	**1.196**
3	40	60.00	**454.40**	**1.278**
4	50	50.00	**531.7**	**1.376**
5	60	40.00	**596.68**	**1.454**

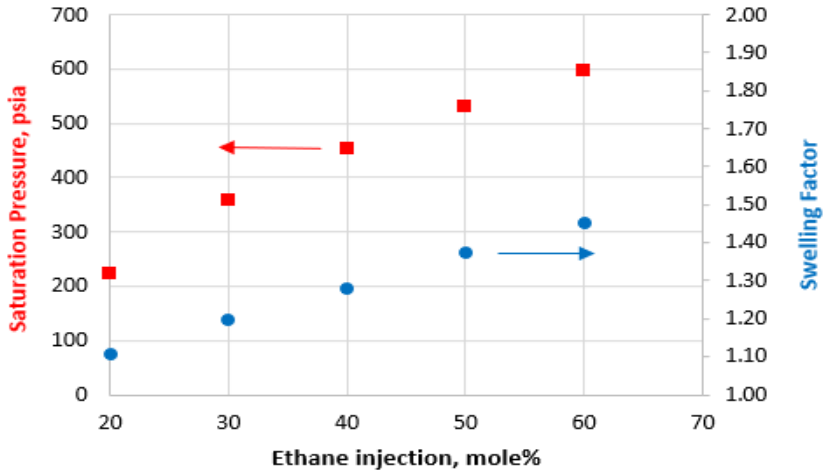

Figure 22. Saturation pressure and swelling factor versus ethane injection for crude oil #4

3.3.4.5. Crude oil #5

Table 14. Saturation pressure for CO_2 - crude oil #5

Crude oil #	5						
°API	39.47						
Feed #	**CO_2-mole%**	**Oil-mole%**	**Psat, psia**				
			25 °C	**60 °C**	**90 °C**	**120 °C**	**150 °C**
1	25	75	**313.75**	**453.52**	**574.89**	**692.34**	**805.96**
2	30	70	**402.44**	**561.72**	**714.59**	**873.74**	**999.92**
3	35	65	**465.38**	**690.24**	**896.48**	**1076.28**	**1234.63**
4	40	60	**531.66**	**879.81**	**1053.74**	**1278.86**	**(*)**
5	45	55	**623.03**	**(*)**	**(*)**	**(*)**	**(*)**
6	50	50	**644.01**	**(*)**	**(*)**	**(*)**	**(*)**

(*) The experiment found no values because the system reached a liquid-liquid equilibrium where no saturation pressure could be measured.

Table 15. Swelling factors for CO_2 - crude oil #5

Crude oil #	5						
°API	39.47						
Feed #	CO_2-mole%	Oil-mole%	SF				
			25 °C	60 °C	90 °C	120 °C	150 °C
1	25	75	1.12	1.15	1.17	1.20	1.23
2	30	70	1.14	1.17	1.19	1.22	1.24
3	35	65	1.17	1.20	1.22	1.23	1.25
4	40	60	1.19	1.23	1.25	1.25	(*)
5	45	55	1.23	(*)	(*)	(*)	(*)
6	50	50	1.25	(*)	(*)	(*)	(*)

(*) The experiment found no values because the system reached a liquid-liquid equilibrium where no saturation pressure could be measured.

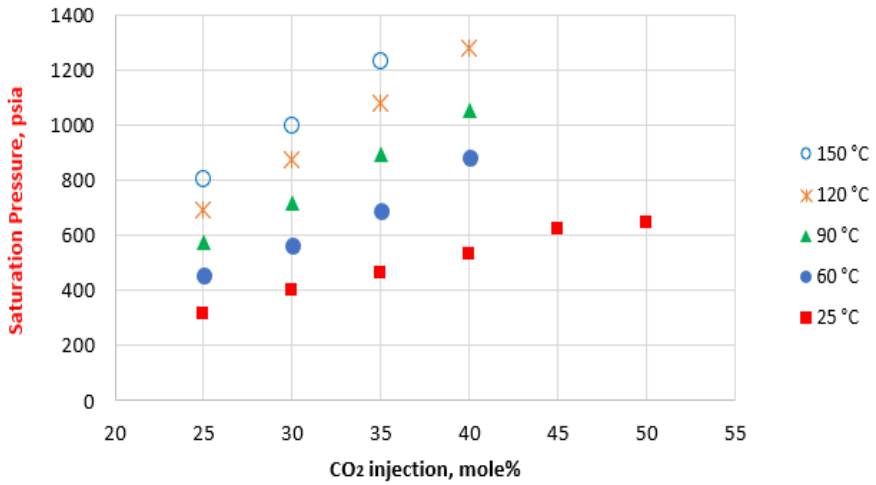

Figure 23. Saturation pressure versus CO_2 injection for crude oil #5

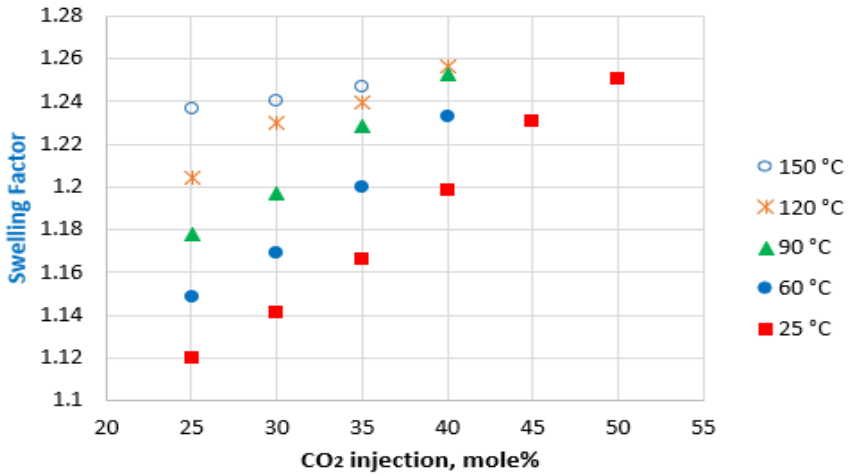

Figure 24. Swelling factor versus CO_2 injection for crude oil #5

3.3.4.6. Asphaltene Visualization in PVT Cell

Figure 25 to *29* show the PVT cell's final condition after the CCE experiment for all crude oil cases. Crude oil #1 presents tiny dark particles, while crude oils #2-3 do not show any precipitation. Crude oil #4 shows a highly viscous liquid similar to wax. From the solid, black particle visualizations, we can confirm the existence of asphaltene precipitation for crude oil #5 due to the CO_2 injection. For this reason, crude oil #5 with injections of CO_2 gas is used for the further asphaltene precipitation analyses.

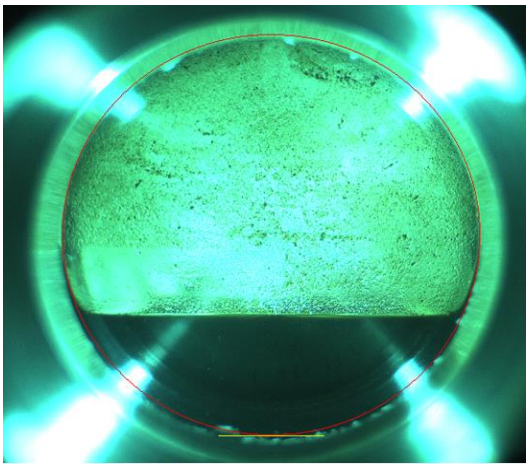

Figure 25. Crude oil #1 final condition

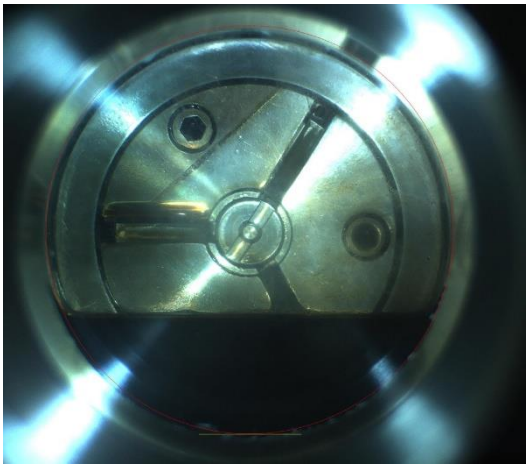

Figure 26. Crude oil #2 final condition

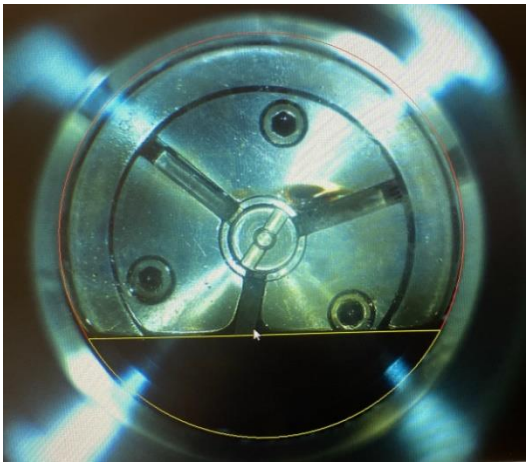

Figure 27. Crude oil #3 final condition

Figure 28. Crude oil #4 final condition

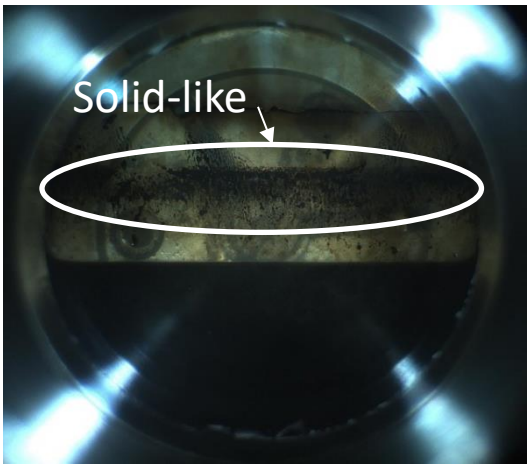

Figure 29. Crude oil #5 final condition

3.3.5. Summary

Saturation pressure increases with temperature and gas injections for all cases. The swelling factor rises with temperature and gas injections in all cases. However, theoretically, it is well known that the oil swelling factor increases under immiscible conditions. The oil swelling factor will decrease for a miscible process because the swollen oil has reached a maximum, and oil extraction into the gas phase has begun.

Comparing propane and ethane saturation pressures, higher values were found for mixtures of oil-ethane than oil-propane for crude oils #1-4. This difference is explained by the knowledge that lighter components have higher vapor pressures. For the case of CO_2 injections, the saturation pressure values were higher than ethane and propane injections for the same reservoir temperatures and at the same gas mole fraction injections. The explanation is that the non-hydrocarbon component, CO_2, has higher vapor pressure than ethane and propane at the same temperature. From the images taken after the PVT experiment, it is clear that for crude oil #5, the injection of CO_2 will produce asphaltene precipitation. For this reason, this crude oil is chosen to study further asphaltene precipitation predictions.

3.4 Saturation Pressure Simulation

3.4.1. Mathematical Modelling

3.4.1.1. Chemical Potential and Fugacity

The chemical potential (G_i) of a component (i) in a mixture is calculated by:

$$dG_i = RTd(\ln f_i) \quad \text{Equation 2}$$

$$\lim_{P \to 0} f_i = y_i P = P_i \quad \text{Equation 3}$$

Where R is the universal gas constant, T is the temperature of the mixture, f_i is fugacity, P is pressure, and y_i is vapor composition of component *i*.

The following condition must be met to calculate the vapor-liquid equilibrium pressure.

$$f_{vi} = f_{li} \quad \text{Equation 4}$$

The fugacity of the vapor phase equals the fugacity of the liquid phase.

3.4.1.2. Fugacity coefficient and K factor

The fugacity coefficient is defined as:

$$\varphi_i = \frac{f_i}{y_i P} \quad \text{Equation 5}$$

The K_i factor is defined as the ratio of fugacity coefficient of the liquid phase and fugacity coefficient of the vapor phase.

$$K_i = \frac{\varphi_{li}}{\varphi_{vi}} \quad \text{Equation 6}$$

3.4.1.3. Peng-Robinson (PR) EOS

The PR EOS proposed by Peng and Robinson in 1976 is the most widely used equation of state applied in the chemical and petroleum industries (Peng & Robinson, 1976). This equation was modified in 1978, introducing a new parameter for heavier components with an acentric factor (ω) higher than 0.49. The PR EOS is used to determine the saturation pressure of CO_2 and crude oil #5.

The PR EOS model is defined by:

$$P = \frac{RT}{v-b} - \frac{a}{v(v+b)+b(v-b)} \qquad \text{Equation 7}$$

Where v is molar volume, and a and b are the EOS parameters:

3.4.1.4. Mixing rule

For a mixture, the PR-EOS parameters are defined by:

$$a = \sum_{i=1}^{N}\sum_{j=1}^{N} y_i y_j \sqrt{a_i a_j}\left(1-k_{ij}\right) \qquad \text{Equation 8}$$

$$b = \sum_{i=1}^{N} y_i b_i \qquad \text{Equation 9}$$

$$a_i = 0.457235\frac{R^2 T_{ci}^2}{P_{ci}}\alpha_i \qquad \text{Equation 10}$$

$$b_i = 0.077796\frac{RT_{ci}}{P_{ci}} \qquad \text{Equation 11}$$

where y_i and y_j are the vapor compositions of components i and j. a_i and b_i are the EOS parameters for component i, and k_{ij} is often referred to as the binary interaction

parameter (BIP) or sometimes referred to as the binary interaction coefficient (BIC). R is the ideal gas constant, T_{ci} is the critical temperature, and P_{ci} is the critical pressure.

The coefficient α_i can be calculated by:

$$\alpha_i = [1 + m(\omega_i)(1 - \sqrt{T_{ri}}]^2 \quad \text{Equation 12}$$

where m is a function of the acentric factor ω :

$$m(\omega_i) = 0.3796 + 1.485\omega_i - 0.1644\omega_i^2 + 0.01667\omega_i^3, \quad \omega_i > 0.49 \quad \text{Equation 13}$$

$$m(\omega_i) = 0.37464 + 1.54226\omega_i - 0.26992\omega_i^2, \quad \omega_i \leq 0.49 \quad \text{Equation 14}$$

3.4.1.5. BIP

The binary interaction parameters (BIP) are a set of correction terms required for calculating *a*, the EOS parameter. The BIP can be obtained by fitting the EOS for each binary mixture. WinProp uses the following BIP correlation.

- Chueh-Prausnitz Correlation (1967)

$$k_{ij} = 1 - \frac{\sqrt{(v_{ci}^{1/3} v_{cj}^{1/3})}}{(v_{ci}^{1/33} + v_{cj}^{1/3})/2}^{\beta} \quad \text{Equation 15}$$

where v_{ci} and v_{cj} are the molar critical volume of components i and j. β is an empirical parameter that can be adjusted for the fluid system (Chueh & Prausnitz, 1967).

3.4.1.6. Volume Translation

Another important parameter is the volume translation described by (Péneloux et al., 1982). Volume translation solves the main problem with two-constant EOS, the poor liquid volumetric predictions. A simple correlation term is applied to the EOS-calculated molar volume. For a multicomponent mixture:

$$v_l = v_l^{EOS} - \sum_{i-1}^{N} x_i c_i \qquad \text{Equation 16}$$

$$v_v = v_v^{EOS} - \sum_{i-1}^{N} y_i c_i \qquad \text{Equation 17}$$

Where v_l and v_v are the corrected liquid and vapor molar volumes, v^{EOS} is the EOS-calculated volume, and c_i is the component-specific constant which is define for every component through the volume-translation coefficient (s_i).

$$s_i = \frac{c_i}{b_i} = 1 - \frac{A_o}{M_i^{A_1}} \qquad \text{Equation 18}$$

A_o and A_1 are constant values depending on the hydrocarbon family: paraffin, naphthene, or aromatic. M_i is the molecular weight of each component in the mixture and b_i are the component EOS parameters for component i.

3.4.2. Simulation Results

WinProp (CMG, 2011) calculates the saturation pressures of the mixture of CO_2 and Crude oil 5. The EOS chosen in the software is PR (1978). Before starting the saturation pressure calculations, the program requires the following data: Composition specification, Initial K-values, Output level, and Stability test level.

The composition specification for crude oil #5 is shown in *section 4.5.1 Oil Characterization, Table 29.*

The initial K-values are estimated internally from Wilson's equation (Wilson, 1969).

$$lnK_i = 5.37(1 + \omega_i)\left(1 - {T_{ci}}/{T}\right) + \ln\left({P_{ci}}/{P}\right) \quad \text{Equation 19}$$

The output level is usually 1, but if more information is needed regarding the flash calculation iterations, set the output level to 2.

The stability test calculates whether the system needs to split into two or more phases to achieve equilibrium at a specified pressure and temperature. (Baker et al., 1982; Michelsen, 1982) showed how the Gibbs energy tangent-plain criterium could be used to establish the equilibrium. The mixture will split into two phases, *y* and *x*, if the mixture's Gibbs energy is lower than the Gibbs energy of the mixture's n moles, which is considered a homogeneous phase. In WinProp for two-phase oil/gas systems, level 1 is sufficient; for systems with more than two phases, a value of 4 may be used.

The simulation program also needs component properties such as critical pressures, critical temperatures, and acentric factors for all components, including the plus fraction. These values are calculated internally for WinProp, *Table 30.*

The procedure describing the saturation pressure calculation in WinProp is described following:

a) A temperature value at which the saturation pressure is calculated is required.
b) The estimated saturation pressure is also required as the initial value.

c) At a given temperature, there are two saturation pressures, upper and lower values, the upper can be the dew point, and bubble point of the fluid, and the lower is the dew point of the fluid. One of them should be chosen.

3.4.3. Regression

Most EOS characterizations commonly hold errors in saturation pressures from around ± 10%, errors in density predictions of ± 5%, and composition mole percent might be off for the key components (Coats & Smart, 1986; Whitson, 1984).

Following the guidelines from Coats and Smart (1986), the EOS parameters chosen for the regression were the BIP, BIP's exponent from (Chueh & Prausnitz, 1967), and the omega factors Ω_a and Ω_b for the lightest and the heaviest component. The omega factors Ω_a and Ω_b for the PR EOS are 0.45724 and 0.07780, which can be adjusted to match experimental data to the model.

1. Ω_a for the lightest component (OA).
2. Ω_a for the heaviest component (OA).
3. Ω_b for the lightest component (OB).
4. Ω_b for the heaviest component (OB).
5. k_{ij} between the lightest heaviest component (DD).
6. β experimental exponent (PVC3).

A summary of the regression variables is shown below.

Table 16. Regression variables from WinProp

Variable		Lower Bound	Upper Bound	Initial Value	Final Value	% Change
OA CO2		2.9262E-01	4.3893E-01	3.6578E-01	3.7542E-01	2.64
OA C25+		2.9262E-01	4.3893E-01	3.6578E-01	3.7105E-01	1.44
OB CO2		6.2236E-02	9.3355E-02	8.1695E-02	8.2218E-02	0.64
OB C25+		6.2236E-02	9.3355E-02	6.3218E-02	6.3218E-02	0.00
PVC3 1		0.0000E+00	1.8000E+00	0.0000E+00	1.7107E+00	100.00
DD C25+	:CO2	0.0000E+00	2.0000E-01	0.0000E+00	6.0281E-02	100.00

Saturation pressures after the final regression are shown below.

Table 17. Saturation pressure for CO_2 - crude oil #5 Simulation

Feed	Psat, psi (simulation)						
	%CO_2-mole	%Oil-mole	25 °C	60 °C	90 °C	120 °C	150 °C
1	25	75	**307.41**	**458.59**	**589.20**	**711.05**	**818.55**
2	30	70	**378.96**	**567.76**	**730.45**	**881.32**	**1013.2**
3	35	65	**454.90**	**684.84**	**882.42**	**1064.5**	**1222.4**
4	40	60	**535.91**	**811.13**	**1046.9**	**1262.7**	**(*)**
5	45	55	**622.78**	**(*)**	**(*)**	**(*)**	**(*)**
6	50	50	**716.58**	**(*)**	**(*)**	**(*)**	**(*)**

(*) Values were not found in the experiment, so the simulation was not performed.

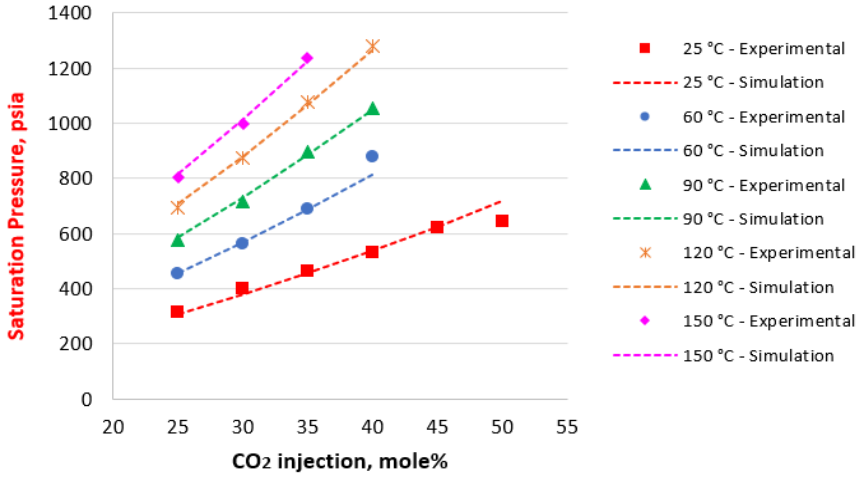

Figure 30. Experimental and simulated saturation pressures versus CO_2 injections

The average relative deviation (AARD) gives how accurate the regression is.

$$AARD = \frac{1}{n}\sum_{i=1}^{n}\frac{|P_i^{cal} - P_i^{exp}|}{P_i^{exp}} \qquad \text{Equation 20}$$

After the regression, an *AARD* value of 3.3% confirms good experimental saturation pressure data predictions.

3.4.4. Summary

Determining saturation pressures using the PR-EOS (1978) available in WinProp gives a good prediction of the experimental data. However, an adequate regression must be performed to match the experimental and modeled data. After tuning the regression parameters, a calculated value of AARD equal to 3.3 % confirms the reliability of the modeled saturation pressures. The next chapter will use these saturation pressures to predict the asphaltene precipitation of crude oil #5 and CO_2 mixtures at different reservoir temperatures.

Chapter 4: Asphaltene Precipitation Prediction

4.1. Introduction

As mentioned earlier, crude oil #5 studies the asphaltene precipitation during the CO_2 injection process. The procedure and results from quantifying the asphaltene content in crude oil #5 are explained in section *4.2, Asphaltene Content by ASTM-3279*. In section *4.3, Asphaltene Content in SDS*, crude oil #5 asphaltene precipitation is analyzed through a high-pressure-high-temperature and high-resolution microscope of a Solid Detection System (SDS). Section *4.4 Asphaltene Onset Pressures, Phase Behavior, Reversibility Mechanisms,* and Precipitation *Measurements,* shows the experimental results of the CO_2-induced EOR process for crude oil #5 under different reservoir conditions. Following section *4.5, Asphaltene Precipitation Simulation* includes using a solid thermodynamic model available in WinProp (CMG, 2011) to reproduce the experimental asphaltene precipitation data. The modeling program uses the saturation pressures calculated in *Chapter 3: PVT Analyses.* Asphaltene precipitation predictions show good approximations to the experimental data for isothermal cases at different CO_2 mole injection fractions. However, the program faced limitations in predicting the asphaltene precipitation at different temperatures. For that reason, a developed solid molar volume equation is proposed in this work. The proposed correlation for the solid molar volume combines changes in temperature and CO2 mole injection fractions in one function, which tunes the solid model used in WinProp. Finally, this chapter's findings are presented, and the accuracy of the simulated results using the developed solid molar volume equation is confirmed with an absolute average relative deviation (AARD) of 0.7%.

4.2. Asphaltene Content by ASTM-3279

4.2.1 Materials

Crude oil #5 is the sample chosen for the asphaltene precipitation analysis. This sample is the dead oil collected from a reservoir in Texas. The API gravity is measured at 37.82, and the molecular weight is 209.91 g/mole. N-pentane (HPLC Grade, 95% min, Alfa Aesar) is the precipitating solvent. Toluene (99% purity, Fisher Chemical) is also used in this experiment to separate impurities. The labware and equipment required are listed following: a 100 ml Erlenmeyer flask, a 500 ml filtering flask, 500 ml beaker, filtering funnel, six glass microfiber filter pads 32-34 mm diameter, a 100 ml graduated measuring cylinder, oven capable of maintaining a temperature of 110 ± 5 °C, and a balance with an accuracy of at least 0.0001 g.

4.2.2 Experimental Setup and Procedure

The experiment followed the standard ASTM-3279 (ASTM-D04 Committee, 2007). *Figure 31* and Figure 32 show the flowcharts of this procedure (Espinoza Mejia et al., 2022). Crude oil #5 was in the liquid phase at ambient conditions, so the pre-heating process was unnecessary. The Erlenmeyer flask mass is weighted as *A*. Around 1 gram of oil sample is placed in the flask, and its mass is weighted as *B*. The oil sample mass, *C*, will be the difference between *B* and A, *Equation 21*. 100 ml of n-pentane per 1g of oil sample is added to the flask, labeled as Mixture 1. Mixture 1 is placed on a magnetic stirrer hot plate with a refluxing condenser for 15 minutes and kept resting until it reaches ambient temperature, around two hours. A filtration pad is dried at 110 °C, weighted as *D*, and placed in a filtration funnel. Mixture 1 now contains the sample's asphaltene precipitation and some solid impurities. A gentle vacuum filtration performs the separation of the insoluble solids.

$$\boldsymbol{C = B - A} \qquad \text{Equation 21}$$

C is the oil sample mass (g), *B* is the flask + oil sample mass (g), and *A* is the flask mass (g)

Depending on the insoluble solids content of the sample, more than one filter pad may be needed. The insoluble material collected in the filter pad is placed in the oven at 110 °C for 30 minutes and then weighted as *E*. The difference between *E* and *D* is the mass of the insoluble material, *F* (asphaltene + impurities), *Equation 22*. Asphaltenes are soluble in toluene; therefore, to separate the impurities from asphaltene particles, the filter pad containing the insoluble solids is placed in a 500 ml beaker and washed with toluene. The liquid and solids are kept for further filtration, labeled as Mixture 2. A new filter pad is placed in the oven at 110 °C for 30 minutes and then weighted as *G*. The dried filter pad is placed in the filtration funnel, and Mixture 2 is filtrated. More than one filter pad may be needed depending on the purity of the sample. The filter pad containing the impurities is placed in the oven at 110 °C for 30 minutes and then is weighted as *H*. The difference between *H* and *G* is the mass of the impurities, *I*, *Equation 23*. The mass percent of asphaltenes, *Ac* present in the oil sample is a ratio of the difference between *F* and *I* with respect to *C*, *Equation 24*.

$$\boldsymbol{F = E - D} \qquad \text{Equation 22}$$

F is the insoluble mass (g), *E* is insoluble + filter pad mass (g), and *D* is filter-pad mass (g)

$$\boldsymbol{I = H - G} \qquad \text{Equation 23}$$

I is the impurities (g), *H* is the impurities + filter pad mass (g), and *G* is filter-pad mass (g)

$$\boldsymbol{Ac = \frac{(F - I)}{C} 100\%} \qquad \text{Equation 24}$$

Ac is the asphaltenes content (wt%)

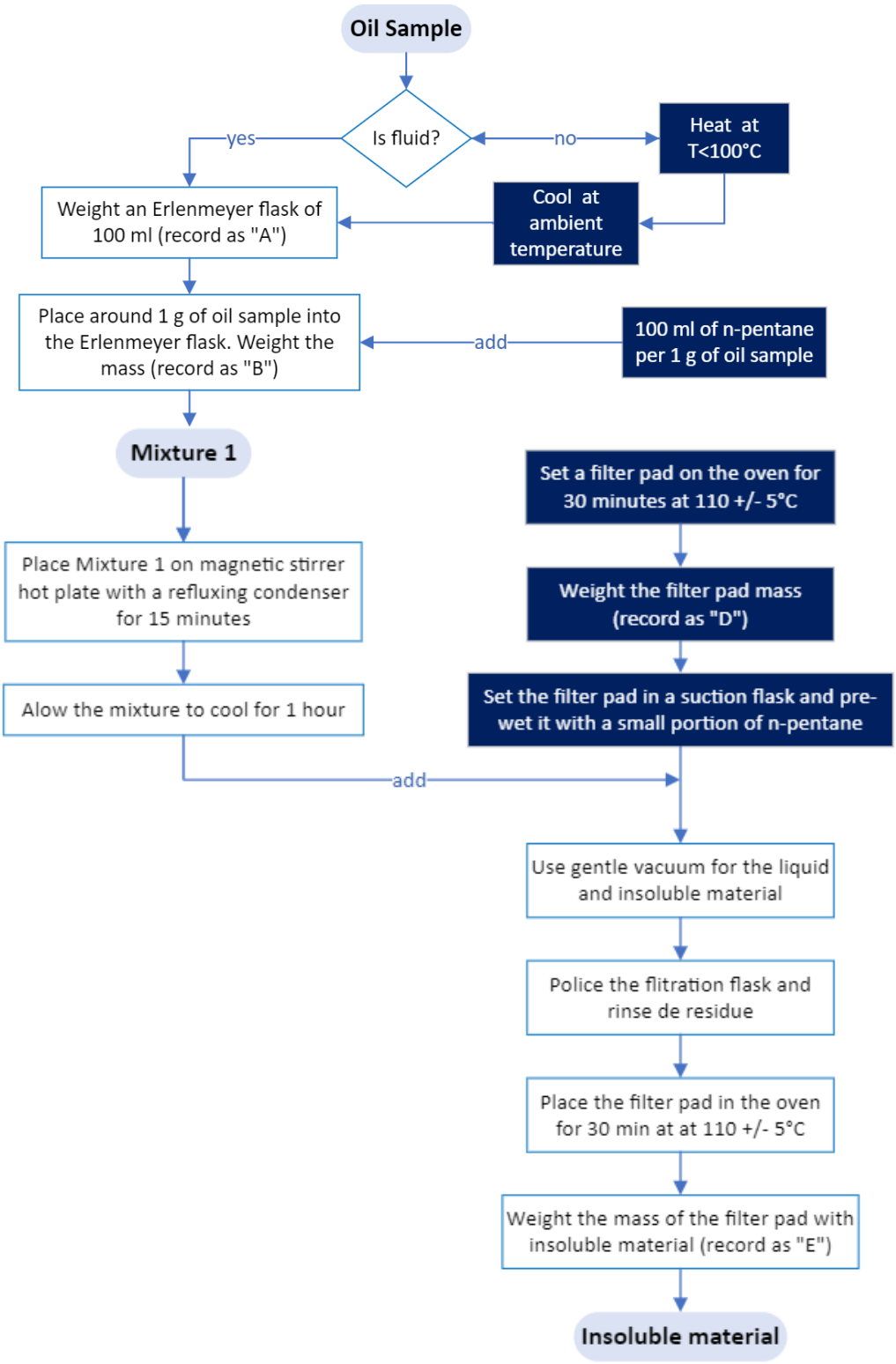

Figure 31. Asphaltene content determination-experimental procedure part 1

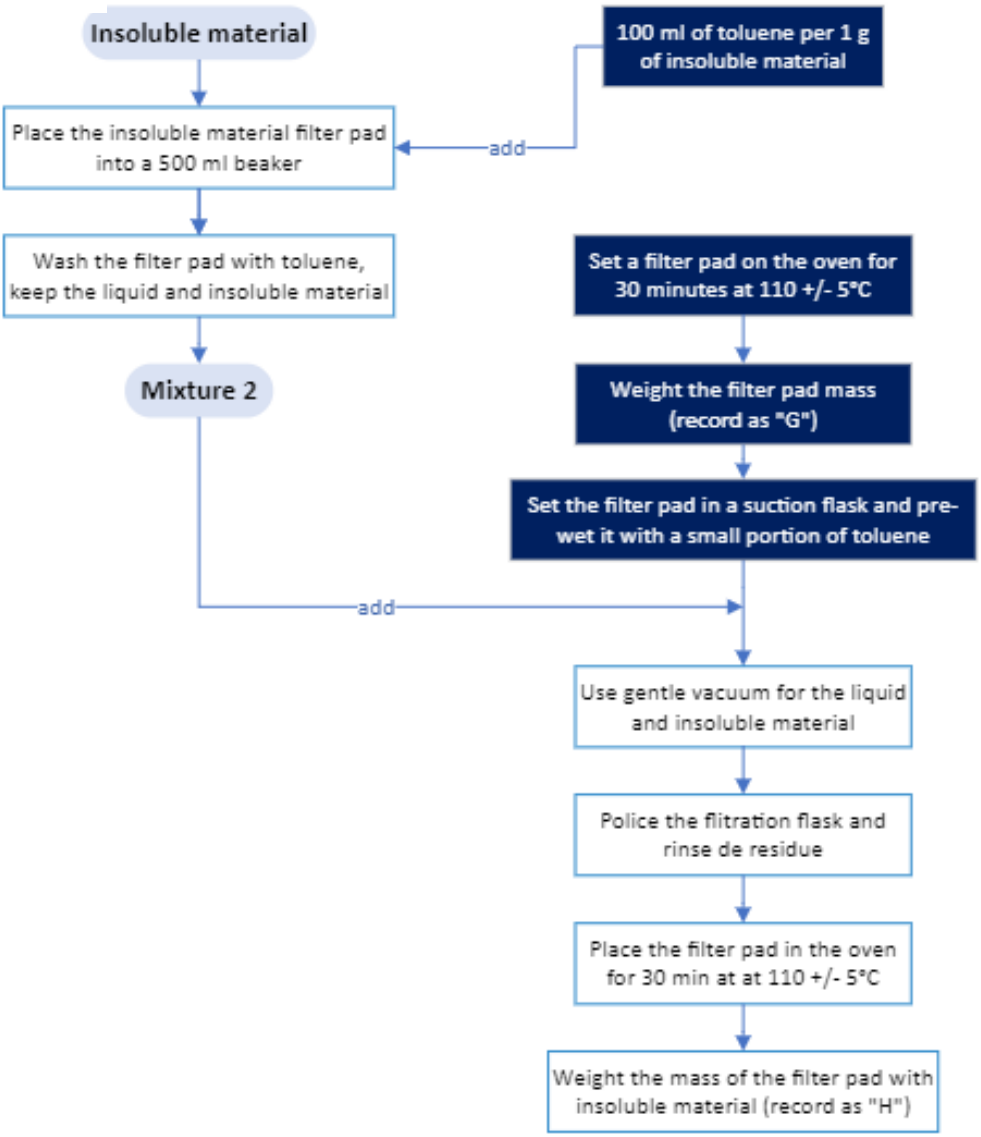

Figure 32. Asphaltene content determination-experimental procedure part 2

4.2.3 Experimental Results

The asphaltene content experiment for crude oil #5 was performed twice, named experiments #1-2. The results are shown in *Table 18*. Before starting the procedure, the oil sample was already clean; no impurities were found in any experiments. *Figure 33* shows the asphaltene particle appearance for crude oil #5 when the solvent is n-pentane. If the alkane solvent is changed, the appearance of asphaltene particles might also change (Buckley et al., 1998; Wang & Buckley, 2003). The solubility of asphaltenes in a determinate solvent affects their final molecular structure (Buckley et al., 2007; Fakher et al., 2020).

Table 18. Average asphaltene content for crude oil #5

Experiment #		**1**	**2**
A	Erlenmeyer flask mass, g	68.376	107.171
B	Erlenmeyer flask mass + oil sample, g	69.491	108.287
C	oil sample mass, g	1.115	1.116
D	filter pad mass, g	0.111	0.112
E	filter pad mass + insoluble material, g	0.196	0.163
F	Insoluble material mass, g	0.085	0.051
G	filter pad mass, g	0.111	0.112
H	filter pad + impurities mass, g	0.111	0.112
I	impurities mass, g	0.000	0.000
Ac%	asphaltenes content, wt%	**7.62%**	**4.57%**
Average		**6.10%**	

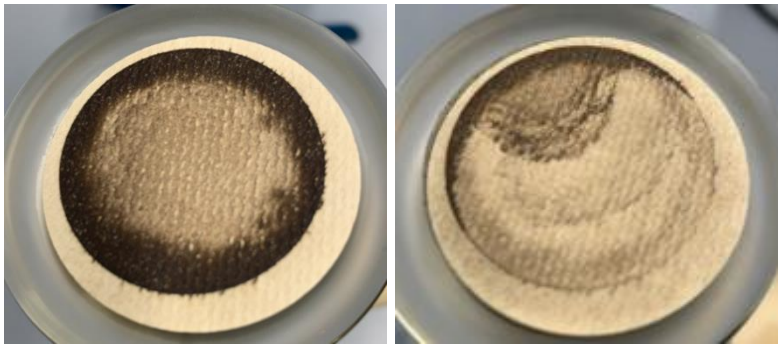

Figure 33. Asphaltenes from experiment #1 (left) from experiment #2 (right)

The appearance of asphaltene solids changes from one crude oil to another (Dickie & Yen, 1967; Sheu et al., 1995; Sheu, 2002; Buenrostro-Gonzalez et al., 2004). New experiments, #3-4, were performed with crude oils #6-7 to corroborate the variation in the appearance of asphaltene particles. The results for the asphaltene precipitation experiments are shown in *Table 19*. *Figure 34* shows the asphaltene appearance for crude oils #6 (left) and crude oil #7 (right). The asphaltene content of crude oils #6-7 is higher than crude oil #5. Likewise, The solid particles are darker than crude oil #5.

Table 19. Average asphaltene content for crude oils #6-7, respectively

Experiment #		**3**	**4**
A	Erlenmeyer flask mass, g	68.376	68.376
B	Erlenmeyer flask mass + oil sample, g	69.426	69.407
C	oil sample mass, g	1.050	1.031
D	filter pad mass, g	0.111	0.111
E1	filter pad mass 1 + insoluble material, g	0.128	0.120
E2	filter pad mass 2 + insoluble material, g	0.192	0.160
F	Insoluble material mass, g	0.098	0.058
G	filter pad mass, g	0.111	0.111
H	filter pad + impurities mass, g	0.111	0.111
I	impurities mass, g	0	0
Ac%	asphaltenes content, wt%	**9.33%**	**5.63%**

Figure 34. Asphaltenes from experiment #3 (left) and experiment #4 (right)

4.2.4 Summary

Crude oils #5-7 showed asphaltene contents higher than 3%. The total asphaltene contents are 6.10% (average), 9.33%, 5.63% for crude oils #5-7, respectively. According to the Boer criteria (de Boer et al., 1995), crude oils with asphaltene content higher than 3% are more likely to develop asphaltene precipitation problems. However, nowadays, many researchers have confirmed that asphaltene precipitation not only depends on the asphaltene content but also on the interactions of asphaltenes with other SARA components (Maqbool et al., 2009; Punase et al., 2016; Ashoori et al., 2017). The strong polar-polar interactions between asphaltenes-resins and resins-aromatics molecules keep the force balance in equilibrium. The introduction of a solvent, in this case, n-pentane, produces the separation of asphaltenes molecules from the resin-aromatics structures. The asphaltene micro-aggregates agglomerate with other asphaltene molecules forming bigger aggregates and eventually clusters. The asphaltene precipitation starts when associated asphaltene structures are big and heavy enough that they can no longer be colloids in the solution (Mullins et al., 2017; Vargas & Tavakkoli, 2018).

The experiment concluded that the precipitated asphaltene solids for crude oils #5, 6, and 7 have different colors and appearances even though the same solvent (n-pentane) is used. This fact corroborates the theory that asphaltenes have no unique and extremely complex structure (Dickie & Yen, 1967; Mitchell & Speight, 1973).

4.3. Asphaltene Content in SDS

4.3.1 Materials

This section uses a piston-equipped Solid Detection System (SDS) to corroborate the results obtained in *section 4.2*. The SDS (SDSPVTFV1000, Core Lab) is equipped with a high-pressure-high-temperature cell. Additionally, a charge-couple-device (CCD) high-resolution digital 1.4M pixels video camera allows real-time visualization of the process. An internal heater and an external bath-cooler control the temperature increasing and decreasing. The pressurization and depressurization process in the SDS are managed by moving forward and backward the piston of the cell. The SDS-cell's maximum operating volume, pressure, and temperature are 40 ml, 15,000 psia, and 200°C. Pressure and temperature data are recorded in real-time with sensors of ±0.35 full scale and 0.5 °C, respectively (Zheng, 2020). Acetone and Toluene (99% purity, Fisher Chemical) are used for washing purposes.

The SDS's software is described next. Euclide has friendly-user interphase with a video camera which allows changing the images' resolution, tone, and scale. Likewise, this program measures the fluid volumes from the screen view. Falcon shows in friendly-user interphase where the reference and setpoints pressure, temperature, and volume, and graphs with respect to time are displayed in real-time. Besides, the piston stroke rate is adjusted to simulate small or significant pressure differences. Last, the Ellix software is a statistical distribution tool that measures the number, length, width, perimeter, thickness, and area of particles detected by the SDS's video camera. Ellix reports a statistical analysis where the maximum and minimum particle sizes are listed, the data median is calculated, and the particle's distribution plot is presented. *Figure 35* shows a schematic representation of the SDS.

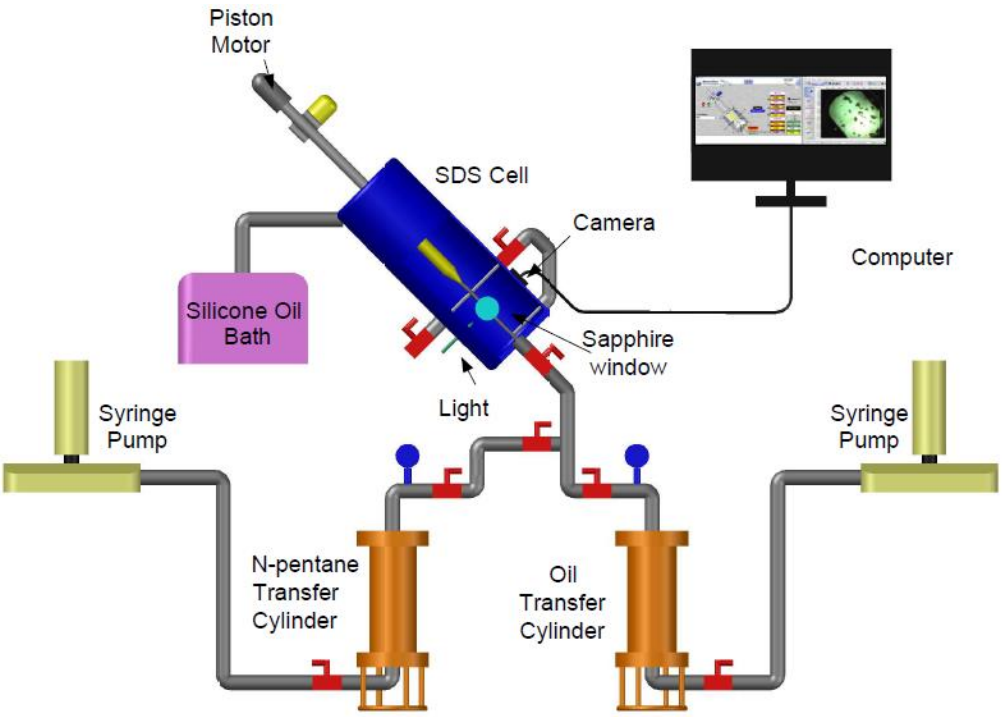

Figure 35.Schematic diagram of the SDS for the asphaltene content experiment

4.3.2 Experimental Setup

Before starting the experiment, the SDS must be cleaned and dried. First, 5 ml of toluene is used to wash the remaining hydrocarbon. Then, 5 ml of acetone is used to wash the remaining water. This procedure is performed three times or until clear acetone is obtained after the final washing. The next step is to dry the SDS. In the drying process, a line of compressed air is used for 1 hour. Usually, a vacuum process is followed after the drying. However, for this experiment, void conditions are not required. After the cleaning and drying, the SDS is ready for the oil and n-pentane injection.

4.3.3 Experimental Procedure

The procedure starts by connecting the oil and n-pentane transfer cylinders to the SDS cell. Then, 0.4 ml of Crude oil #5 is charged into the SDS at room temperature. The mass of the oil sample is calculated using the oil density from *section 3.2.1, Density*. Following the proportion recommended by the ASTM-3279 (1g of oil sample per 100 ml of n-pentane), 33.4 ml of n-pentane is charged into the SDS at room temperature. Next, keeping the recirculation valve open and the rest valves close, the piston is moved forward and backward to enhance the mixture recirculation. Lastly, the mixture is kept resting for about 24 hours to ensure the maximum asphaltenes precipitation. The Ellix software allows the observation, quantification, and statistical analysis of the precipitated asphaltene particles. In the SDS microscope, the asphaltene particles' morphology is visualized. The solid particles' size, color, and shape are compared with referential data to verify their coincidence with asphaltene particle characteristics.

4.3.4 Experimental Results

Figure 36 shows the asphaltenes particles' color and shape. The dark shapes are asphaltenes, the green line areas are software particle identification, and the white-like fond is the microscope window. 769 asphaltene particles were found. The minimum and maximum length, width, median, thickness, perimeter, and area are also reported in *Table 20*. *Figure 37* shows the statistical distribution of the numbers of particles versus their length.

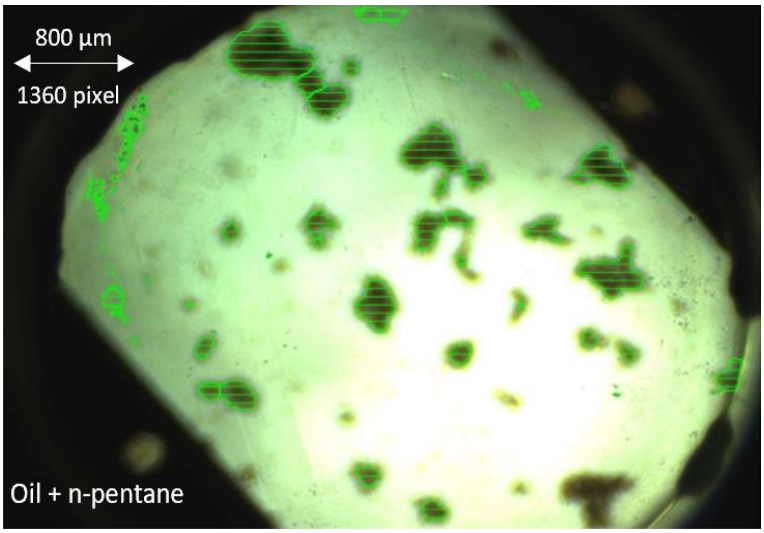

Figure 36.Asphaltene particles microscopic visualization for crude oil #5

Table 20. Asphaltene statistical data from Ellix software for crude oil #5

	Number	Minimum	Maximum	Sum	Average	Standard dev.	% Conf
Length [µm]	769.00	4.09	749.25	17779.72	23.12	62.84	19.21
Width [µm]		4.09	529.65	11581.00	15.06	44.94	21.09
Median [µm]		4.05	673.10	17531.75	22.80	73.22	22.70
Thickness [µm]		3.34	328.56	7122.07	9.26	24.23	18.49
Object perimeter [µm]		9.44	2199.87	48080.27	62.52	195.31	22.08
Object area [µm²]		11.13	197988.48	1128412.13	1467.38	10366.51	49.93

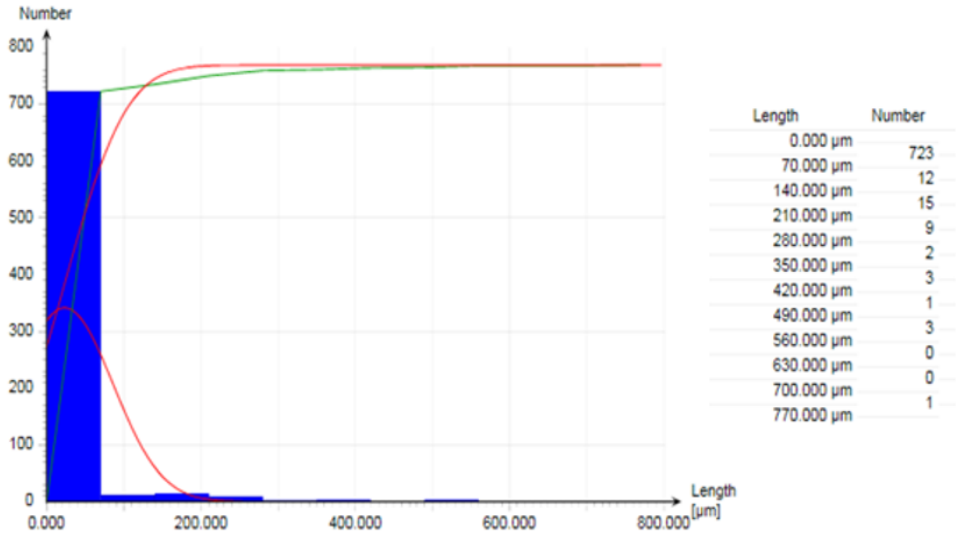

Figure 37. Statistical distribution of asphaltene particles for crude oil #5

Table 21 shows the calculation of the asphaltene content in mass percent. The oil contained in the microscope view volume is calculated with the microscope window dimensions and the oil density. A theoretical average value of asphaltenes density of 1.232 g/cm^3 (Elkahky et al., 2019), the sum area, and the mean thickness from *Table 20* are used in the calculation. The asphaltene content found is 10.864 wt% for crude oil #5. This value is slightly higher than the average 6.1 wt%, determined in section *4.2 Asphaltene Content by ASTM-3279*. The calculated asphaltene content demonstrates that the SDS returns good predictions of asphaltene content.

Table 21. Asphaltene mass content in the SDS microscope view

camera window diameter, cm	1.270
camera window area, cm^2	1.267
camera window wide, cm (diameter tube SDS)	0.836
oil + n-pentane volume, cm^3 (1g-oil=0.836cm^3-oil/100cm^3-n-pentane)	0.304
oil volume, cm^3	0.003
oil density, g/cm^3 @25°C	0.836
oil mass, g	**0.002**
asphaltenes sum area, cm^2 (Table 20)	0.011
asphaltenes mean thickness ((max+min)/2), cm (Table 20)	0.017
asphaltenes average volume, cm^3	1.87E-04
asphaltenes average density, g/cm^3	1.232
asphaltenes mass, g	**2.31E-04**
asphaltenes mass, wt%	**10.955%**

4.3.5 Summary

From the experiment, asphaltene precipitation particles typically vary from black to brown and do not have a specific shape. Some are small chunks, and others are big-long particles. These results are consistent with other authors' publications (Hosseini-Dastgerdi et al., 2015; Pillon, 2001; Taheri-Shakib et al., 2020).

The particle length of asphaltenes for crude oil #5 varies from 0 to 70 μm for 723 particles, from 70-140 μm for 12 particles, and 140-210 μm for 15 particles. These results match most of the asphaltene particle sizes reported by other researchers (Ferworn et al., 1993; Zeinali Hasanvand et al., 2017).

The asphaltene content (10.864 wt%) determined using the SDS corroborates a successful asphaltene precipitation prediction.

4.4. Asphaltene Onset Pressures, Phase Behavior, Reversibility Mechanisms, and Precipitation Measurements during CO_2-induced EOR process

4.4.1 Materials

The crude oil #5 asphaltene content and its particle characteristics were determined and analyzed in *section 4.3*. This section presents the effect of pressure and temperature on asphaltene precipitation for mixtures of crude oil #5 and CO2 gas injections. A pressure-depletion-CO_2-induced EOR process is reproduced using the SDS. The asphaltene onset pressures (AOP) are measured for each isothermal-depressurization process for three different CO_2 mole % injections. The measurements are repeated for five different reservoir temperatures. At each of these conditions, the phase behavior and reversibility mechanisms of the process are analyzed. Finally, the asphaltene precipitation is calculated for each condition based on the SDS microscope visualizations.

An SDS full description is presented in *section 4.3.1, Materials*. Figure 38 shows a schematic representation of the SDS for the AOP experiment. Crude oil #5 is the dead oil collected from a reservoir in Texas. The API gravity is measured at 37.82, and the molecular weight is 209.91 g/mole. The solvent, CO2 gas, has a purity of 99.999% (Matheson, USA). Acetone and Toluene (99% purity, Fisher Chemical) are used for washing purposes.

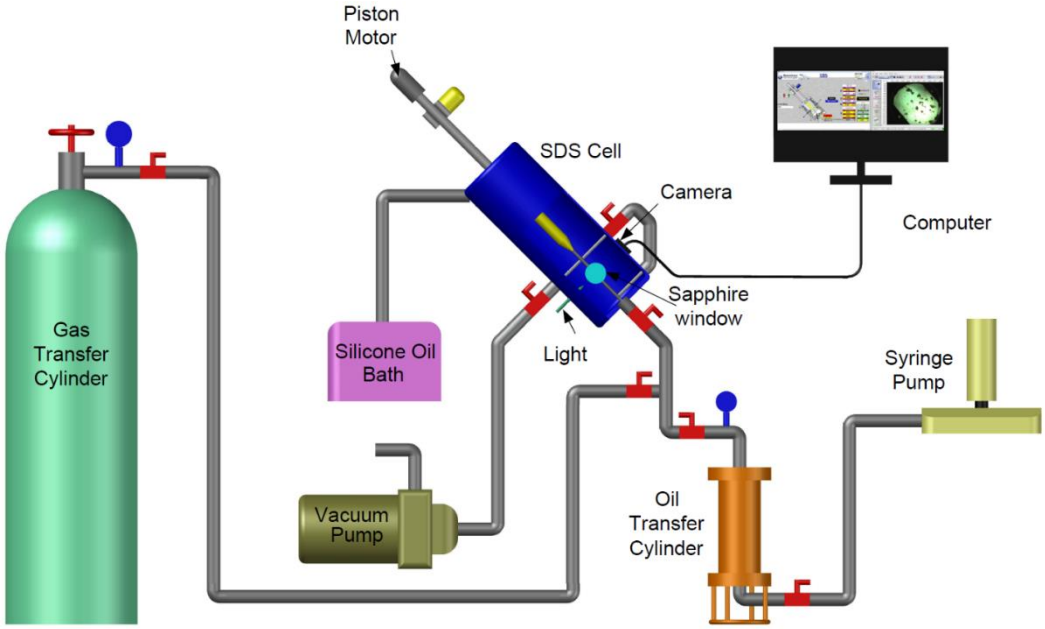

Figure 38. Schematic diagram of the SDS for the AOP experiment

4.4.2 Experimental Setup

The SDS setup is explained in *section 4.3.2 Experimental Setup*. The vacuum process is required before starting the experimental procedure for these experiments.

4.4.3 Experimental Procedure

A pressure-depletion-CO_2-induced EOR process is reproduced in the SDS. First, the asphaltene onset pressures (AOP) are measured. The AOP experiment determines the upper asphaltene onset pressure (UAOP) and the lower asphaltene onset pressure (LAOP). At reservoir conditions, asphaltenes are in equilibrium with the oil-gas fluid. When depletion starts, pressure

decreases continuously, and asphaltene particles start precipitating. The UAOP is the pressure at which the first asphaltene particles start separating from the fluid phase.

Along with the pressure reduction, more asphaltene particles continue leaving the oil phase to start forming a significant number of asphaltene clusters. The maximum amount of asphaltene precipitation is found at the saturation point. Below saturation point, the asphaltene precipitation is induced to re-peptize into the oil phase until the last asphaltene particle is dissolved; this pressure is the LAOP.

Before starting the experiment, the clean and dry SDS cell must be vacuumed. A correct vacuum process is performed with the SDS piston at 15 ml cell volume. The vacuum pump and the SDS must be connected through a seal tubing arrangement. The vacuum process is performed for 30 minutes. The oil injection starts once the SDS is at vacuum pressure and room temperature. A syringe pump injects 10 ml of crude oil #5 from the transfer cylinder into the SDS cell. With all the valves closed, the piston is placed at 300 ml. The CO_2 gas is charged to the SDS from a pressurized cylinder tank. The pressure controls the CO2 injection read in the SDS cell. This pressure was designed previously for a volume combined of 25 mole% of oil and 75 mole% of CO_2 (Feed #1) for an isochoric system. *Table 22* shows the feeds designed for the AOP experiment. A total of 15 isothermal depressurization experiments were performed.

Table 22. Designed tests for AOP experiments

Feed #	CO_2 mole%	Oil mole%	Temperatures, °C
1	25	75	25, 60,90,120,150
3	35	65	
5	45	55	

The oil volume is constant for feeds #1 to 5, and increments of 10 mole% of CO_2 injection were performed for crude oil #5 at 25, 60, 90, 120, and 150 °C.

After the CO_2 injection, with all the valves closed, the cell temperature is set at 25°C. Afterward, in Falcon, pressure versus volume is plotted. The piston is moved forward at 100 ml/h to increase the cell pressure until a single phase is reached in the mixture. A single phase is identified in the plot pressure versus volume for a sudden pressure increment. Meanwhile, the phase behavior changes in the mixture are observed through Ellix. If the camera shows two phases (liquid oil and vapor CO_2), the pressure must increase by moving forward the piston. The rate of this second pressurization must be around 20 ml/h to be able to stop the process when the plot pressure versus volume shows a sharp turning point. The sharp turning point and fast increment of the pressure with respect to volume is an indication that the mixture is in a full liquid phase. The single-phase pressure can be around 10,000-8,000 psia. Allow the system to reach equilibrium condition, monitor for 1 hour the change in pressure and temperature until it reaches constant values along the time. Now, the SDS is ready to start the AOP experiment.

The depressurization process is performed by moving backward the piston of the SDS cell at 3 ml/h. This rate is minimal, which simulates depressurization at equilibrium conditions. Through the Ellix software, the phase behavior changes can be observed during the pressure-reduction process. When the first asphaltenes particles appear in the microscope camera, the pressure is annotated as UAOP. The depressurization process continues, and more asphaltene particles start coming out. The maximum asphaltene precipitation should occur close to the saturation point where the first bubble of CO_2 is observed in the camera. After this point, the asphaltene particle disappears from the microscope view because of their redissolution into the oil phase, and more CO_2 bubbles appear. When the last asphaltene particle is redissolved into the oil phase, the

pressure is annotated as LAOP. The AOP experiment has finished. It is necessary to record and take pictures during the whole experiment to use the asphaltenes precipitation area images to calculate the asphaltene precipitation mass percentage.

The asphaltene onset pressures (UAOP and LAOP) are now measured at 25 °C. The same procedure is followed at 60, 90, 120, and 150 °C for the same feed (75 mole% crude oil #5 and 25 mole% CO_2). For charging feed #2 into the SDS, the system should be stabilized at room temperature again, place the piston at 300 ml and inject the required CO_2 by matching the designed pressure. Then repeat the same procedure for the AOP experiment at all temperatures. The same procedures are followed for feed #3.

4.4.4 Experimental Results

2.2.1.2. Upper Asphaltene Onset Pressures (UAOP)

Table 23 and *Figure* 39 show the UAOP for feeds #1-3. The results show that upper asphaltene onset pressures decrease with temperature increments but increase with CO_2 mole fraction injections.

The values for UAOP are very close at temperatures of 60 and 90°C for 35 and 45 mole% of CO_2 injections. The results' interpretation is that at either 35 or 45 mole% of CO_2 injections in the mixture, the first asphaltene particles start precipitating at values close to 9000 and 7200 psia, respectively.

Table 23. Experimental upper asphaltene onset pressures

Feed #	CO_2-mole%	Oil-mole%	UAOP, psi (experiment)			
			25 °C	60 °C	90 °C	120 °C
1	25	75	**8000**	**7100**	**6000**	**4700**
2	35	65	**9300**	**8900**	**7000**	**6500**
3	45	55	**10000**	**9000**	**7200**	**7000**

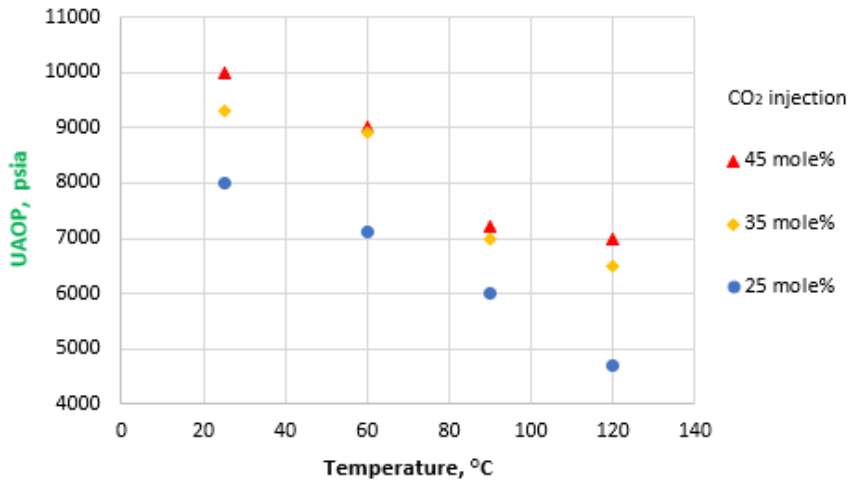

Figure 39. UAOP versus temperature at various CO_2 mole fraction injections

2.2.1.3. Lower Asphaltene Onset Pressures (LAOP)

Table 24 and *Figure 40* show the LAOP for feeds #1-3. The results show that lower asphaltene onset pressures increase with temperature increments and CO_2 mole fraction injections.

LAOP follows the tendency of saturation pressures (see *Figure 23*). Values of LAOP are closer for the cases of 25 and 35 mole% of CO_2 injections. However, for 45 mol% of CO_2 injection, the LAOP has a notorious increment. The results' interpretation is that at 45 mole% of CO_2 injection, the redissolution of asphaltenes is triggered at higher pressures during the pressure-reduction process.

Table 24. Experimental lower asphaltene onset pressure

Feed #	CO2-mole%	Oil-mole%	LAOP, psi (experiment)			
			25 °C	60 °C	90 °C	120 °C
1	25	75	**120**	**150**	**230**	**300**
2	35	65	**205**	**220**	**290**	**352**
3	45	55	**275**	**382**	**440**	**516**

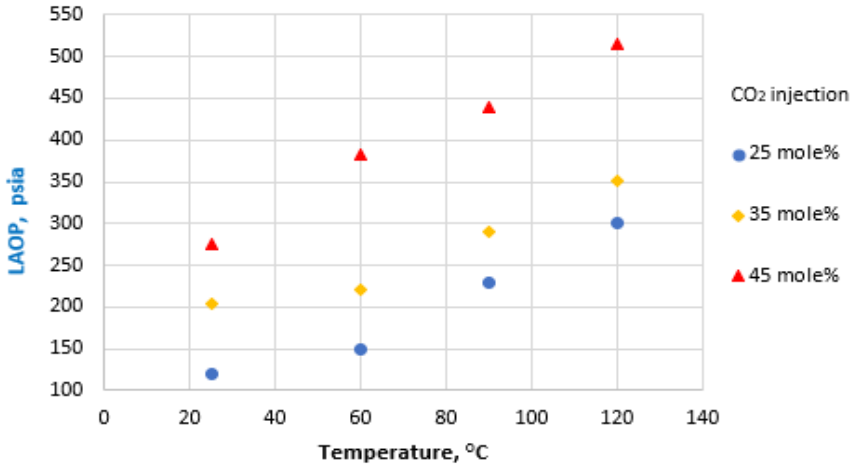

Figure 40. LAOP versus temperature at various CO_2 mole fraction injections

2.2.1.4. Saturation Pressures (Psat)

Table 25 and *Figure 41* show the saturation pressures for feeds #1-3. These results are taken from *Table 14* and corroborated in the AOP experiment. The values in italic (*) are not measured in the CCE experiment. At 60, 90, and 120 °C and 45 mole% of CO_2 injection, the system reached a liquid-liquid equilibrium where no saturation pressure can be measured. On the contrary, the italic values in *Table 25* are taken from the AOP experiment only for comparison purposes between UAOP, LAOP, and *Psat (Figure* 43 *and* Figure 44).

Table 25. Experimental Saturation Pressure

Feed	CO2-mole%	Oil-mole%	Psat, psi (experiment)			
			25 °C	60 °C	90 °C	120 °C
1	25	75	**314**	**454**	**575**	**692**
2	35	65	**465**	**690**	**896**	**1076**
3	45	55	**623**	***1003 (*)***	***1250 (*)***	***1300 (*)***

(*) Values were taken for the AOP experiment only for comparison because the system reached a liquid-liquid equilibrium where no saturation pressure could be measured.

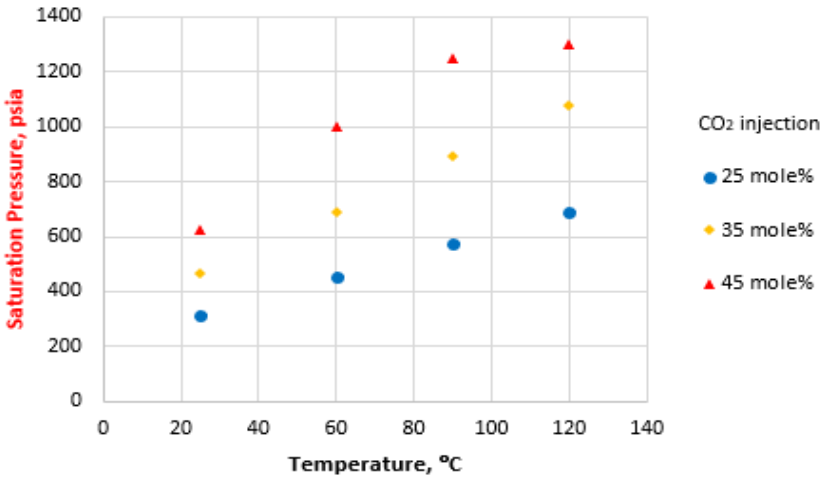

Figure 41. *Psat* versus temperature at various CO_2 mole fraction injections

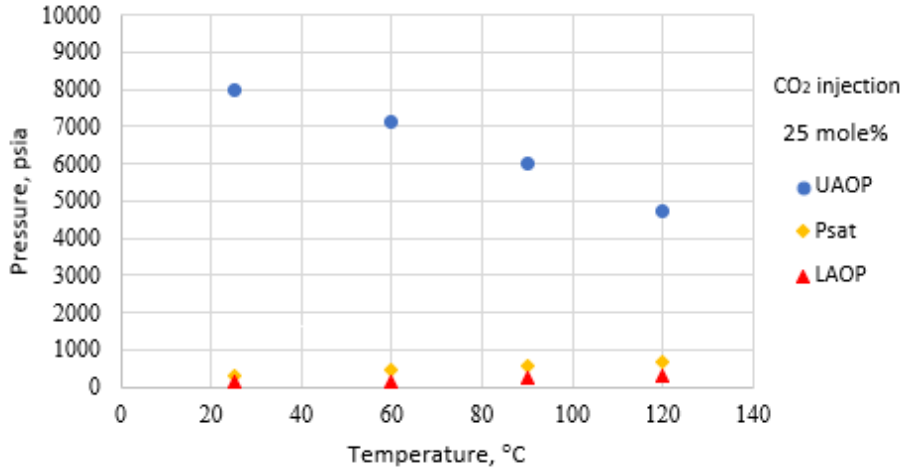

Figure 42. UAOP, *Psat*, and *LAOP* versus temperature at 25 mole% CO_2

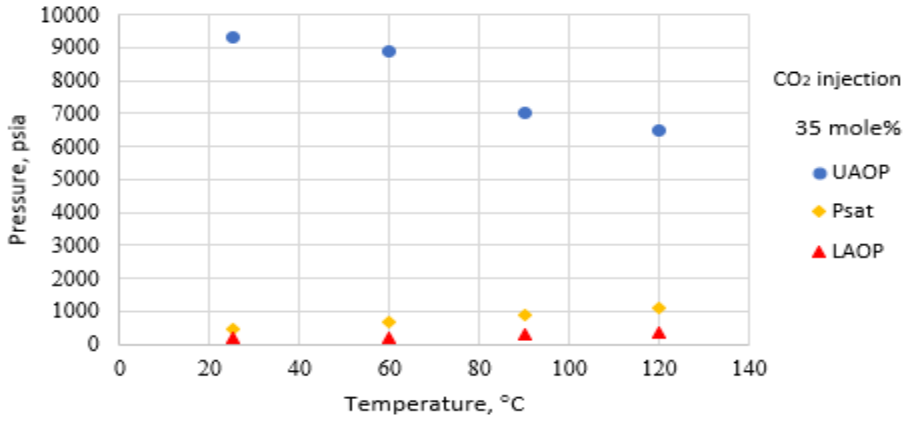

Figure 43. UAOP, Psat, and LAOP versus temperature at 35 mole% CO_2

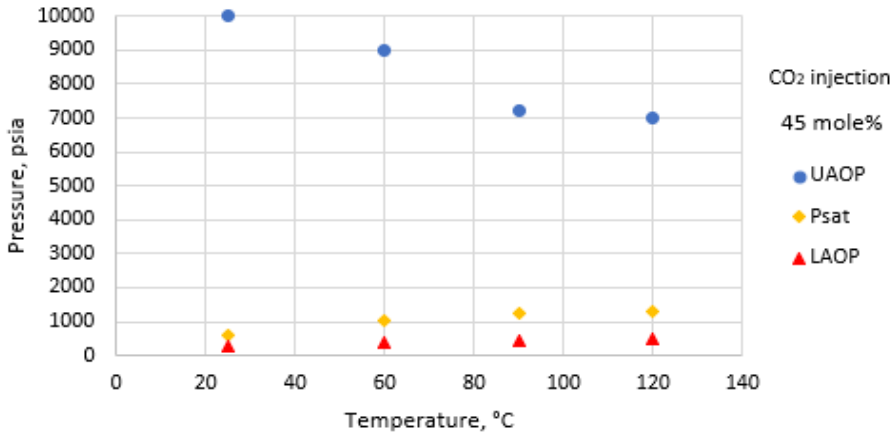

Figure 44. UAOP, *Psat*, and *LAOP* versus temperature at 45 mole% CO_2

2.2.1.5. Asphaltene Phase Behavior Analysis

Figure 45 shows the phase behavior during the AOP experiment at 25 and 60°C. At UAOP, the first asphaltene micelles start coming out from the liquid phase (25 mole% CO_2 and 75 mole% crude oil) until they reach the maximum at saturation pressure. At this pressure (*Psat*), three different phases are identified, solid (asphaltenes), liquid (oil), and gas (CO_2 bubbles). Finally, at LAOP, it is clear to see the liquid (oil) and gas (CO_2) phases, and the last particles of asphaltenes remain in the liquid phase. Visually, the number of asphaltene particles at *Psat* is higher at 25 °C than at 60 °C.

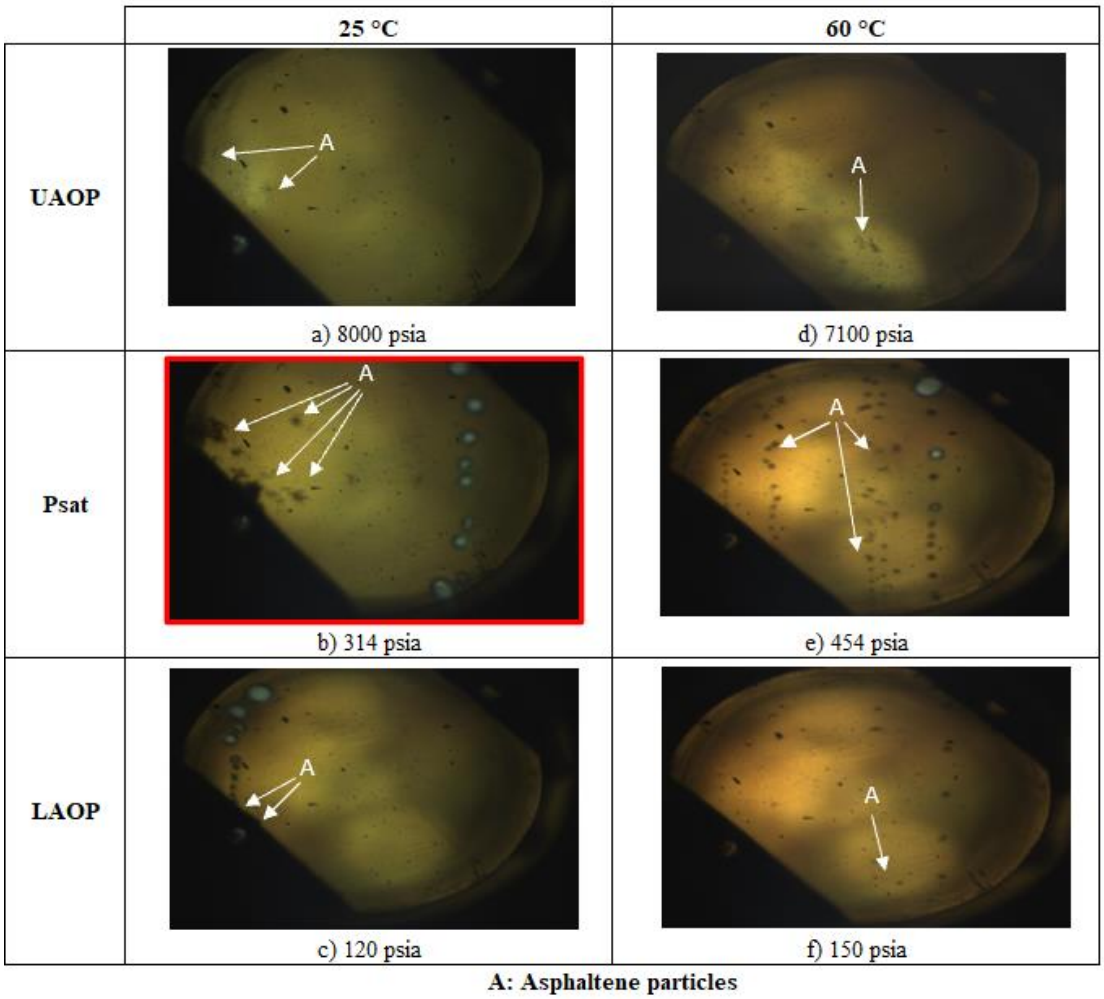

Figure 45. Asphaltene phase behavior, 75 mole% oil and 25 mole% CO_2 at 25 °C and 60 °C

Figure 46 shows the phase behavior during the AOP experiment at 90 and 120°C. The first asphaltene particles coming out at the UAOP can barely be seen at 90 and 120°C. At saturation pressure and 120 °C, the size of the asphaltene particles is smaller than at 60°C. Tiny small asphaltene particles remain as solids at LAOP. From the observations, the asphaltene particle size and the amount decrease along with the temperature increments.

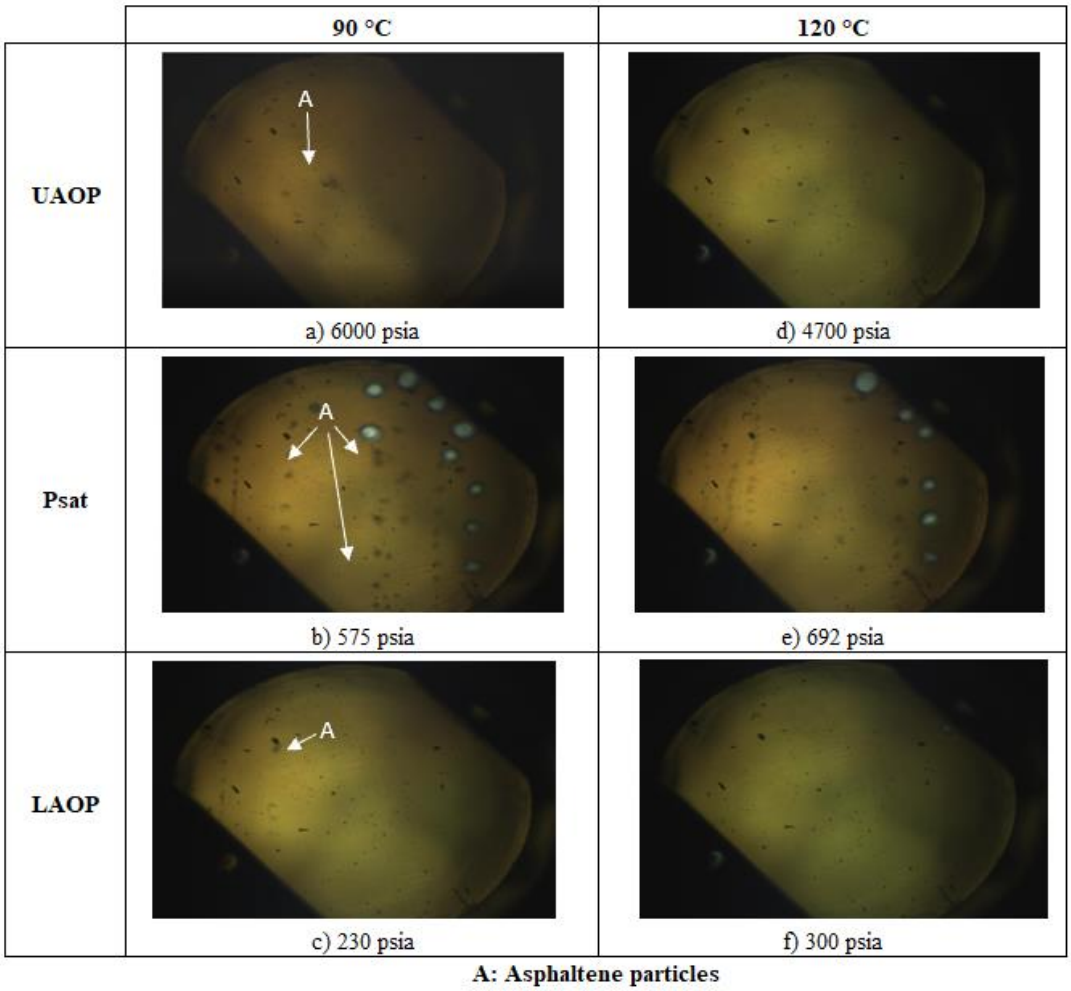

Figure 46. Asphaltene phase behavior, 75 mole% oil and 25 mole% CO_2 at 90 °C and 120 °C

Figure 47 shows the phase behavior during the AOP experiment at 25 and 60°C. At UAOP, the first asphaltene micelles start coming out from the liquid phase (35 mole% of CO_2 and 65 mole% of crude oil) until they reach a maximum at saturation pressure. At this pressure (*Psat*), three different phases are identified, solid (asphaltenes), liquid (oil), and gas (CO_2 bubbles). At LAOP, the last tiny particles of asphaltenes remaining in the liquid phase are shown. Visually, the number of asphaltene particles at *Psat* is higher at 25 °C than at 60 °C.

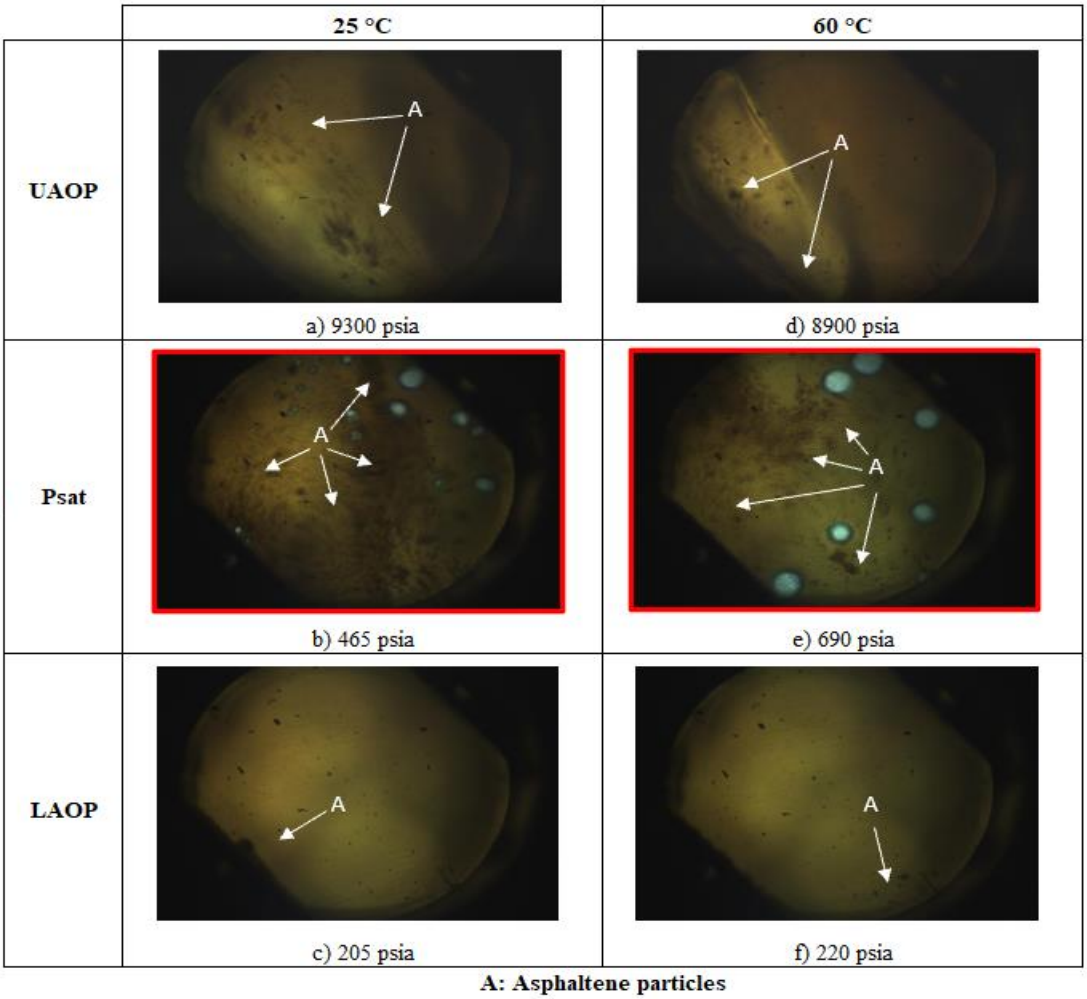

Figure 47.Asphaltene phase behavior, 65 mole% oil and 35 mole% CO_2 at 25 °C and 60 °C

Figure 48 shows the phase behavior during the AOP experiment at 90 and 120°C. More first asphaltene particles coming out at the UAOP are seen for 90 °C than for 120 °C. At saturation pressure and 120 °C, the size of the asphaltene particles is smaller than at 90°C. Tiny small asphaltene particles remain as solids at LAOP for both cases, 90 and 120 °C. From the observations, the asphaltene particle size and the amount decrease along with the temperature increments.

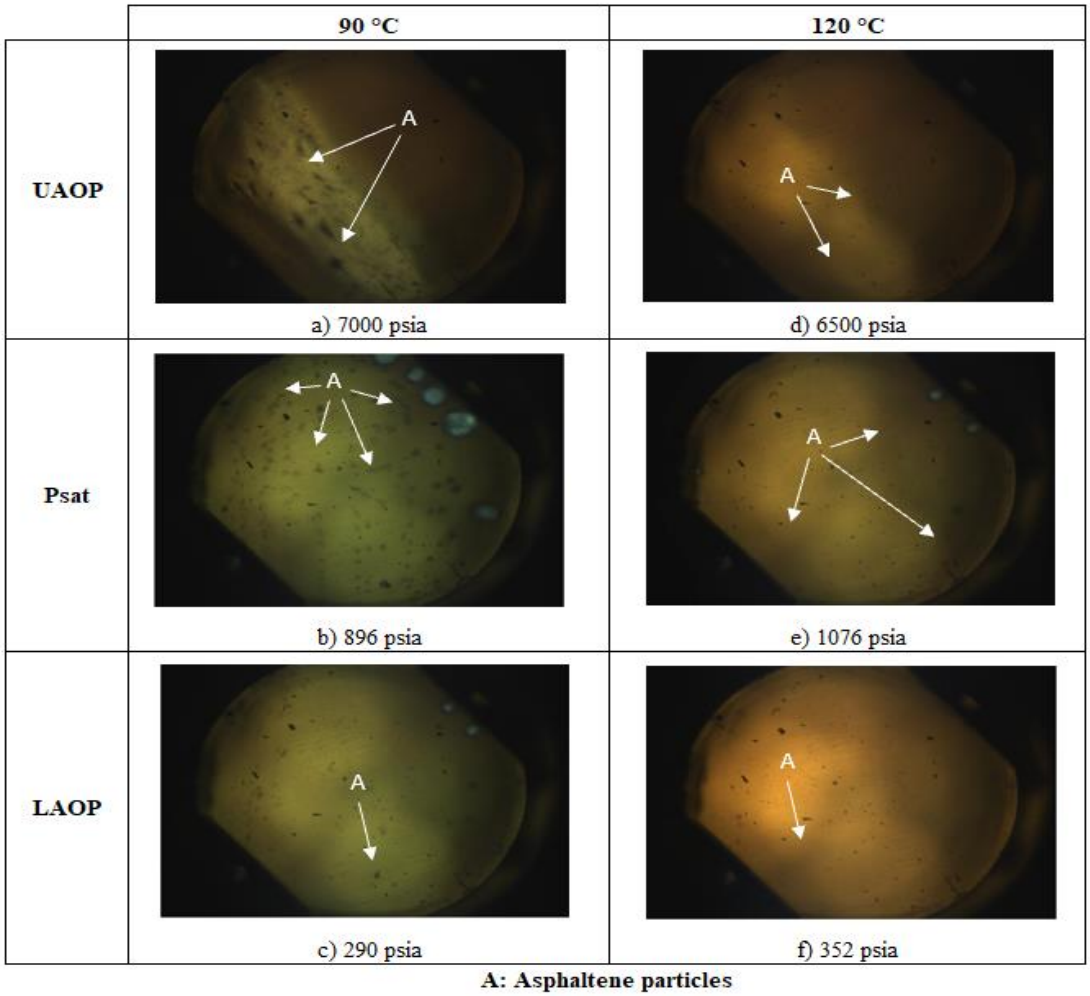

Figure 48. Asphaltene phase behavior, 65 mole% oil and 35 mole% CO_2 at 90 °C and 120 °C

Figure 49 shows the phase behavior during the AOP experiment at 25 and 60°C. At 10000 psia, many asphaltene particles were present in the liquid phase (45 mole% CO_2 and 55 mole% crude oil). The chunks become bigger until they reach a maximum at saturation pressure. At this pressure (*Psat*), three different phases are identified, solid (asphaltenes), liquid (oil), and gas (CO_2 bubbles). At LAOP, the last tiny particles of asphaltenes remaining in the liquid phase are shown. Visually, the number of asphaltene particles at *Psat* is higher at 25 °C than at 60 °C.

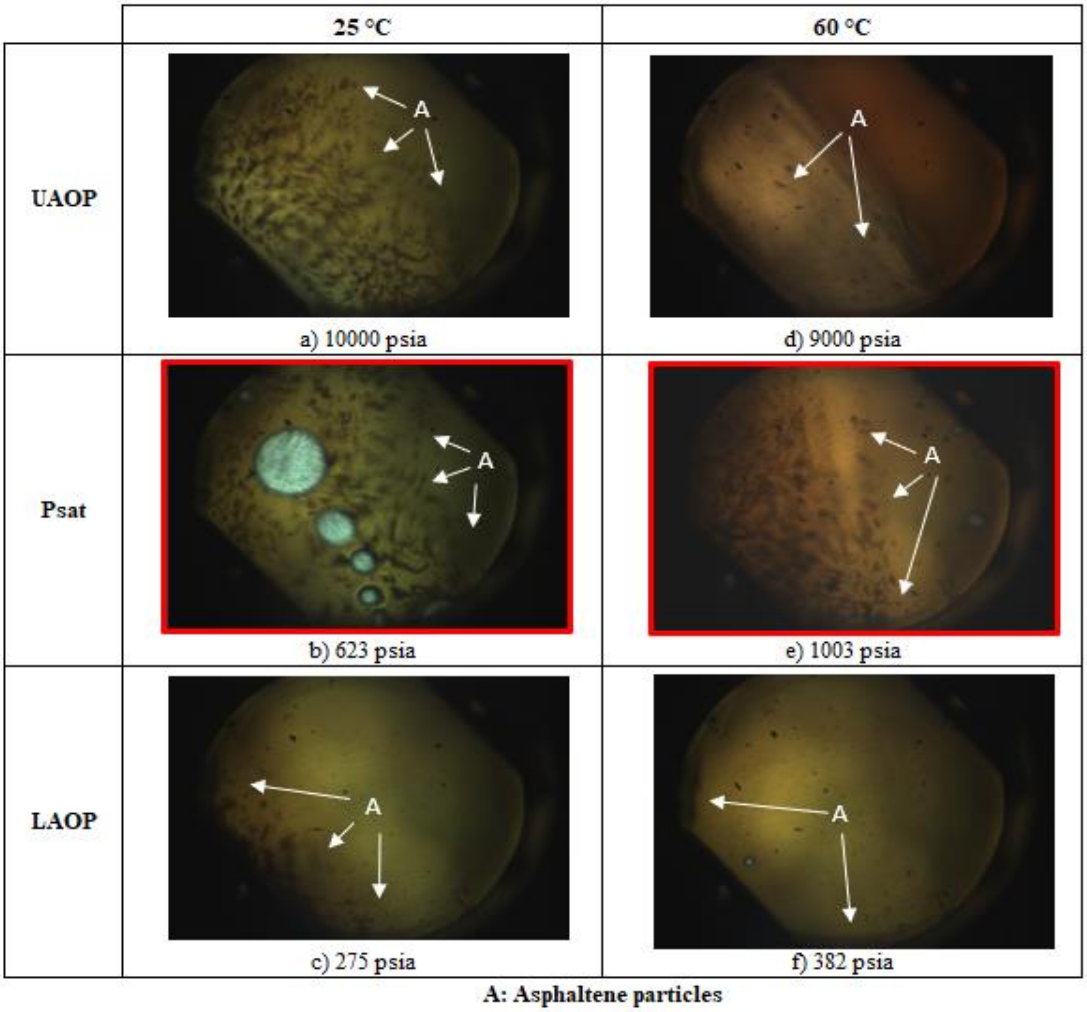

Figure 49. Asphaltene phase behavior, 55 mole% oil and 45 mole% CO_2 at 25 °C and 60 °C

Figure 50 shows the phase behavior during the AOP experiment at 90 and 120°C. The dark appearance of the liquid phase at UAOP is because the first asphaltene particles are super fine solids. Similar characteristics are found at 90 °C and 120 °C. At 120 °C and saturation pressure, the asphaltene particles' size is similar to at 90°C. Tiny small asphaltene particles remain as solids at LAOP for both cases, 90 and 120 °C. From the observations, the asphaltene particle size and amount barely change with the temperature increments for 45 mole% of CO_2 injection.

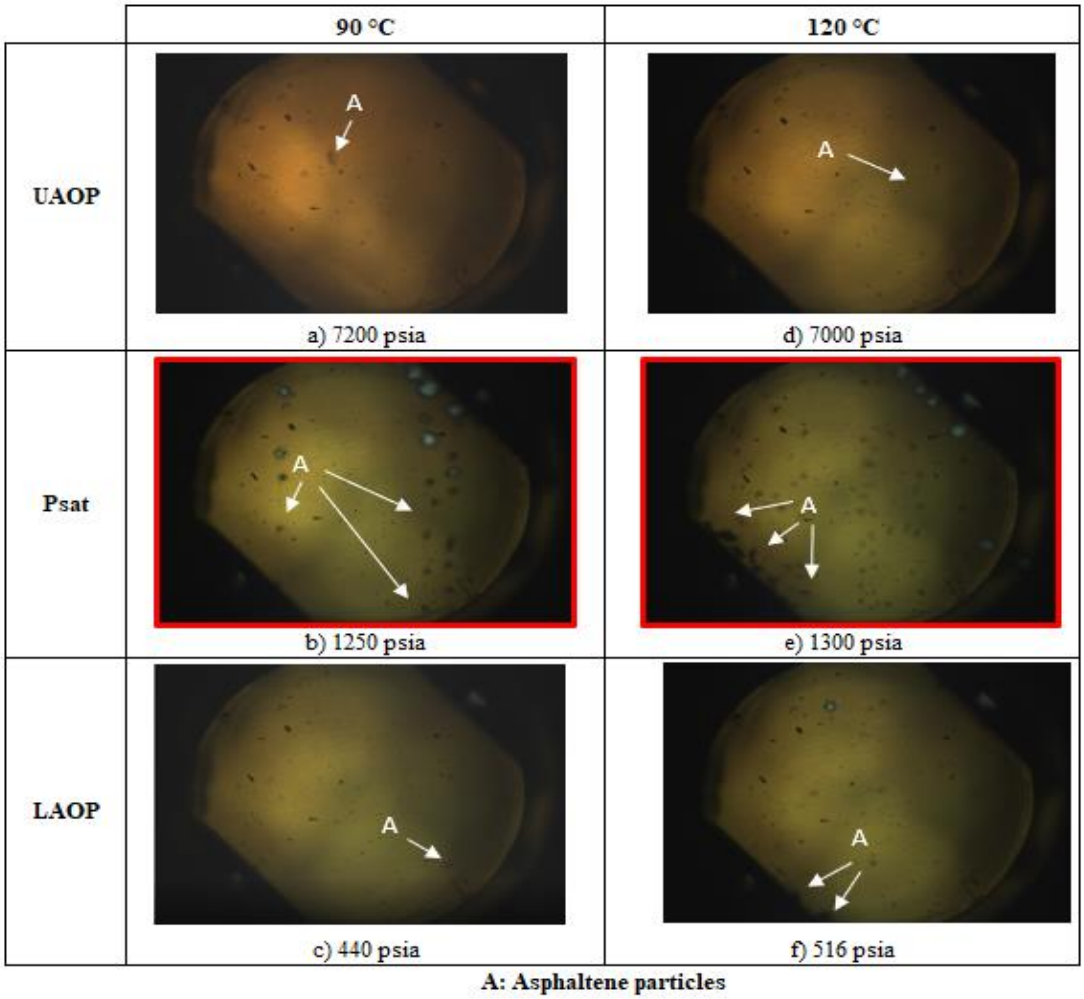

Figure 50. Asphaltene phase behavior, 55 mole% oil and 45 mole% CO_2 at 90 °C and 120 °C

2.2.1.6. Reversibility Mechanisms

In the present AOP experiment, the reversibility of the asphaltene precipitation process is studied. Many authors have corroborated the reversibility of the asphaltene precipitation process for oils without solvents for changes in pressure and temperature (Hirschberg et al., 1984; Kokal & Sayegh, 1995). However, when a solvent is involved, separated cases must be studied (Chaisoontornyotin et al., 2017). The concentration of the solvent will impact the reversibility of the asphaltene precipitation process for changes in pressure and temperature. The reversible process is achieved when all the asphaltene particles are re-dissolved into the liquid phase after depressurization. On the contrary, the process will be irreversible if some particles are still in the solid phase after the depressurization. The remaining asphaltene solid particles are likely to form asphaltene deposition problems (Vargas et al., 2014).

Table 26 presents the reversibility results observed under the SDS microscope for feeds #1-3. Asphaltene particles remained in the SDS cell view after the depressurization for all cases where *Irreversible* is reported. At 25 °C and 25, 35, and 45 mole% CO_2 injections, all cases experienced an irreversible process. Likewise, at 45 mole% CO_2 injections and 25, 60, 90, and 120 °C, all cases experienced an irreversible process. It is concluded that low temperature and high CO_2 fractions are unfavorable conditions triggering the worst asphaltene precipitation cases.

Table 26. Visual determination of asphaltene precipitation reversibility

Feed #	CO_2 mole%	Oil mole%	25 °C	60 °C	90 °C	120 °C
1	25	75	***Irreversible***	*Reversible*	*Reversible*	*Reversible*
2	35	65	***Irreversible***	***Irreversible***	*Reversible*	*Reversible*
3	45	55	***Irreversible***	***Irreversible***	***Irreversible***	***Irreversible***

2.2.1.7. Asphaltene Precipitation

The asphaltene precipitation is calculated with the same method used in section *4.3 Asphaltene Content in SDS*. The precipitated asphaltene particles from mixtures of oil and CO_2 are very small compared to the particles obtained with n-pentane as solvent. In this case, the SDS cannot use statistical analysis to calculate the area of the objects in the microscope view. For that reason, a manual calculation of the area is performed based on the pictures from the AOP experiment (*Figure 45* to *Figure* 50), using the fixed overall particles thickness of 0.017 and asphaltene density of 1.232 g/cm^3 from *Table 21*. Results are shown in *Table 27* at UAOP.

Table 27. Experimental asphaltene precipitation weight percentage at UAOP

	UAOP					
Feed #	**CO_2-mole%**	**Oil-mole%**	**Asphaltene precipitation, wt%**			
			25 °C	**60 °C**	**90 °C**	**120 °C**
1	25	75	**0.239**	**0.061**	**0.016**	**0.004**
2	35	65	**1.177**	**0.801**	**0.206**	**0.106**
3	45	55	**2.355**	**1.820**	**0.411**	**0.317**

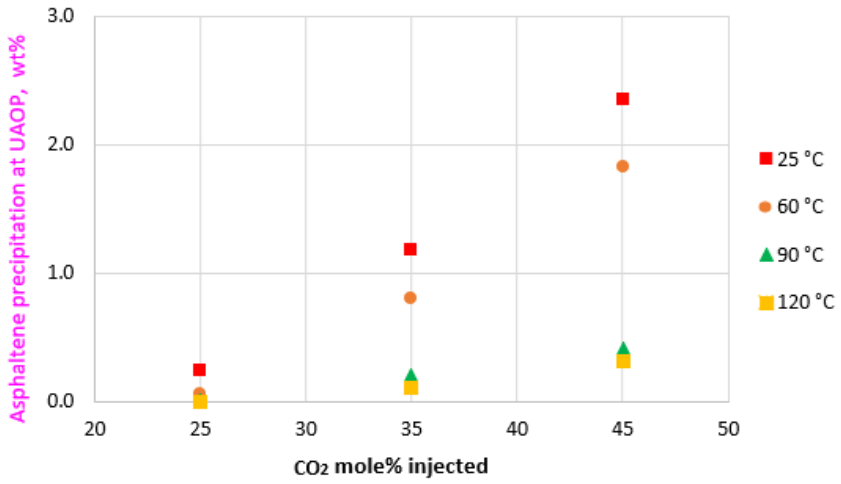

Figure 51. Asphaltene precipitation at UAOP

Similarly, asphaltene precipitation in weight percentage is calculated at saturation pressure. Results are presented in *Table 28* and *Figure 52*.

At saturation pressure, the asphaltene precipitation reaches its maximum. By analyzing the effect of temperature and gas injection, the asphaltene precipitation reaches a maximum value at low temperature, 25 °C, and high CO_2 injection, 45 mole%. When the injection of CO_2 is 25 mole%, the temperature does not significantly impact the asphaltene precipitation. However, for 35 and 45 mole% of CO_2 injections, the values of asphaltene precipitation are higher at 25 and 60 °C than for 90 and 120 °C.

Table 28. Experimental asphaltene precipitation weight percentage at Psat

	Psat					
Feed #	**CO_2-mole%**	**Oil-mole%**	**Asphaltene precipitation, wt%**			
			25 °C	**60 °C**	**90 °C**	**120 °C**
1	25	75	**0.921**	**0.712**	**0.366**	**0.188**
2	35	65	**4.346**	**2.986**	**1.022**	**0.525**
3	45	55	**8.692**	**6.718**	**3.066**	**1.575**

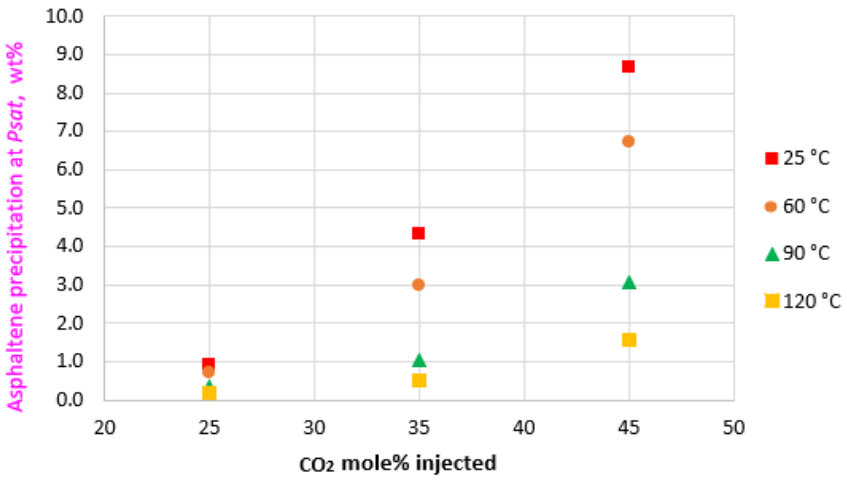

Figure 52. Asphaltene precipitation at saturation pressure

4.4.5 Summary

UAOP and LAOP were successfully measured in the AOP experiment. Likewise, the experiment confirmed the saturation pressures by observing the maximum asphaltene precipitation at saturation conditions. The asphaltene phase behavior is analyzed during the depressurization experiment, and the reversibility mechanisms are identified. After pressure and temperate were established to initial conditions, the remaining asphaltene particles in the microscope view indicated the irreversibility process. Not all CO_2 mole% injections in the mixture experienced irreversibility. The experimental work concluded that low temperature, 25 °C, and high CO_2 mole% injection, 45 mole% are unfavorable conditions where irreversible asphaltene precipitation processes can occur. The quantification of asphaltene precipitation at saturation pressure and UAOP was calculated indirectly using a proportion of the microscope view area and a theoretical value of asphaltene density. This method was proven valid in section *4.3, Asphaltene Content in SDS*. The experimental asphaltene precipitation weight percentages in the next section are simulated in WinProp.

4.5. Asphaltene Precipitation Simulation during CO_2-induced EOR process

4.5.1. Oil Characterization

Normally thermodynamic calculations and the black-oil models consider crude oil as a single component in a combination of gas and water. This simplification reduces the mathematical and computational time (Trangenstein & Bell, 1989). However, crude oil has numerous components, and its characterization has been one of the most challenging topics for petroleum researchers, especially for simulating purposes. The closest approximation to characterizing a crude oil sample is addressed by separating the crude oil into various boiling point fractions in the laboratory (Whitson & Brulé, 2000). Splitting the heaviest fraction improves the characterization of the oil. However, the significant number of oil components increases the properties calculations time, making the flash thermodynamic model solutions impractical. Lumping components with similar properties (pseudo-components or C_{7+} components) improves the oil characterization with an acceptable computational time increment (Abedini & Abedini, 2012).

4.5.1.1. Compositional Analysis

The compositional analysis of crude oil #5 is shown in *Table 32*. The ASTM D5307-97 is used to determine the oil components based on the boiling range distribution by gas chromatography. This method is used for water-free crude oil samples through a maximum temperature of 538 °C. Any material boiling point above 538 °C is reported as residue. This standard applies to crude oil samples that can be solubilized in a solvent to permit sampling.

Table 29. Crude oil #5 compositional analysis

SCN	Component	wt, fraction	MW, g/mole	mole, fraction (z_N)
7	Toluene	0.038	100	0.089
8	Dimethylbenzene	0.039	114	0.081
9	Trimethylbenzenes	0.058	128	0.106
10	Tetramethylbenzenes	0.046	142	0.076
11	C_{11}	0.038	156	0.058
12	C_{12}	0.033	170	0.046
13	C_{13}	0.048	184	0.061
14	C_{14}	0.046	198	0.055
15	C_{15}	0.040	212	0.044
16	C_{16}	0.036	226	0.037
17	C_{17}	0.051	240	0.050
18	C_{18}	0.042	254	0.039
19	C_{19}	0.034	268	0.030
20	C_{20}	0.025	282	0.021
21	C_{21}	0.030	296	0.024
22	C_{22}	0.022	310	0.017
23	C_{23}	0.025	324	0.018
24	C_{24}	0.024	338	0.017
25+	C_{25+}	0.326	570	0.134
		1.00	**234.67**	**1.00**

4.5.1.2. Characterization of the Plus Fraction

For this case, the plus fraction is C_{25+}. Its characterization is performed by splitting this fraction into more pseudo-components.

Pedersen observed a pattern between the oil mole fractions and their component carbon numbers (Pedersen et al., 1985). The oil components mole fraction logarithms directly relate to their single carbon numbers (SCN) above C_6, *Equation 25*.

$$SCN = A + Bln(z_N) \quad \text{Equation 25}$$

where *SCN* is the single carbon number, A and B are constants, and z_N is the mole fraction.

It is desired to split the C_{25+} to C_{49+} (commonly used as the asphaltene component). The splitting mole fractions until C_{48} can be determined using the oil composition from Table 1 and the extrapolation with Equation 2. The lasted fraction, for C_{49+}, is determined by material balance.

For the material balance, the molecular weight of the splitting fractions from C_{25} until C_{48} must be approximated using *Equation 26.*

$$MW_{C_i} = 14SCN - 4 \qquad \text{Equation 26}$$

where MW_{C_i} is the molecular weight of the C_i component and *SCN* is the single carbon number.

The C_{49+} mole fraction is equal to the C_{25+} mole fraction and C_{25} to C_{48} mole fraction summation according to *Equation 27.*

$$z_{C_{49+}} = z_{C_{25+}} - \sum_{i=25}^{48} z_{C_i} \qquad \text{Equation 27}$$

where z_{C_i} is the molar fraction of the C_i component.

The molecular weight of the heaviest splitting plus fraction is determined by *Equation 28*.

$$MW_{C_{49+}} = \frac{MW_{C_{25+}} z_{C_{25+}} - \sum_{i=25}^{48} MW_{C_i} z_{C_i}}{z_{49+}} \qquad \text{Equation 28}$$

All these steps are performed internally in WinProp.

4.5.1.3. Properties for SCNs

The properties required for the vapor-liquid equilibrium calculations are critical pressure and temperature, acentric factor, specific gravity, and boiling temperature. These properties can be estimated from empirical correlations. One of the most popular correlations is the Watson factor, based on the crude oil's molecular weight and specific gravity (Riazi, 1980) *Equation 29.*

$$K_w = 4.5579 MW^{0.15178} \gamma^{-0.84573} \qquad \text{Equation 29}$$

where K_w is the Watson factor, MW is the oil molecular weight, and γ is the oil specific gravity.

Using the Watson factor, the specific gravity of each SCN from 1 to 48 can be calculated according to *Equation 30.*

$$\gamma_{C_i} = 6.0108 MW_{C_i}^{0.17947} K_w^{-1.18241} \qquad \text{Equation 30}$$

where γ_{C_i} is the specific gravity of the C_i component, MW_{C_i} is the molecular weight of the C_i component, and K_w is the Watson factor.

The specific gravity of the maximum plus fraction, C_{49+}, is estimated from material balance with *Equation 31*.

$$\gamma_{C_{49+}} = \frac{z_{C_{49+}} MW_{C_{49+}}}{\frac{MW}{\gamma} - \sum_1^{48} \frac{z_{C_i} MW_{C_i}}{\gamma_{C_i}}} \qquad \text{Equation 31}$$

The boiling temperatures are calculated using *Equation 32* (Soreide, 1989)*Equation* 32.

$$T_{b_{C_i}} = 1928.3 - (1.695 \cdot 10^5) M_{C_i}^{-0.03522} \gamma_{C_i}^{3.266} \cdot \exp\left[-(4.922 \cdot 10^{-3}) M_{C_i} - 4.7685 \gamma_{C_i} + (3.462 \cdot 10^{-3}) M_{C_i} \gamma_{C_i}\right] \quad \text{Equation 32}$$

where $T_{b_{C_i}}$ is the boiling temperature of the C_i component in °R.

The critical temperatures and pressures can be estimated from *Equation 33* and *Equation* 34 (Lee & Kesler, 1975).

$$T_{c_{C_i}} = 341.7 + 811\gamma_{C_i} + \left(0.4244 + 0.1174\gamma_{C_i}\right) T_{b_{C_i}} + (0.4669 - 3.2623\gamma_{C_i}) 10^5 T_{b_{C_i}}^{-1} \quad \text{Equation 33}$$

$$P_{c_{C_i}} = \exp\{8.3634 - 0.0566\gamma_{C_i}^{-1} - \left[\left(0.24244 + 2.898\gamma_{C_i}^{-1} + 0.118857\gamma_{C_i}^{-2}\right) 10^{-3}\right] T_{b_{C_i}} + \left[\left(1.4685 + 3.648\gamma_{C_i}^{-1} + 0.47227\gamma_{C_i}^{-2}\right) 10^{-7}\right] T_{b_{C_i}}^2 - \left[(0.42019 + 1.6977\gamma_{C_i}^{-2}) 10^{-10}\right] T_{b_{C_i}}^3\} \quad \text{Equation 34}$$

where $T_{c_{C_i}}$ is the critical temperature and $P_{c_{C_i}}$ is the critical pressure of the C_i component, in °R and psia, respectively.

The acentric factor ω_{C_i} is calculated using Lee and Kesler (1975) correlation,

If $\frac{T_{b_{C_i}}}{T_{c_{C_i}}} < 0.8$:

$$\omega_{C_i} = \frac{-\ln\left(P_{c_{C_i}}/14.7\right) + A_1 + A_2 T_{b_{C_i}}^{-1} + A_3 lnT_{b_{C_i}} + A_4 lnT_{b_{C_i}}^{6}}{A_5 + A_6 T_{b_{C_i}}^{-1} + A_7 lnT_{b_{C_i}} + A_8 lnT_{b_{C_i}}^{6}} \quad \text{Equation 35}$$

If $\frac{T_{b_{C_i}}}{T_{c_{C_i}}} \geq 0.8$:

$$\omega_{C_i} = -7.904 + 0.1352K_w - 0.007456K_w^2 + 8.359T_{b_{C_i}} + (1.408 - 0.01063K_w)T_{b_{C_i}}^{-1} \quad \text{Equation 36}$$

were A_1 = -5.92714, A_2 = 6.09648, A_3 = 1.28862, A_4 = -0.169347, A_5 = 15.2518, A_6 = 15.6875, A_7 = -13.4721, A_8 = 0.43577

All these steps are performed internally in WinProp.

4.5.1.4. Lumping and property averaging

The properties calculated for each SCN component must be lumped to optimize computing and iteration time for the flash equilibrium calculations. For this case, the heaviest plus fraction, C_{49+}, is not required to lump since this is assigned as the asphaltene component. This process is performed internally in WinProp.

Table 30 shows the compositional analysis and SCN properties of crude oil #5, its lumped components, and its heaviest splitting fraction, C_{49+}.

Table 30. Split and lumped crude oil #5 compositional analysis and SCN properties

SCN	Component	MW, g/mole	mole, % (z_N)	Pc (atm)	Tc (K)	Acentric Factor
7	Toluene	96.00	0.09	30.97	543.20	0.31
8	Dimethylbenzene	107.00	0.08	29.12	570.50	0.35
9	Trimethylbenzenes	121.00	0.11	26.94	598.50	0.39
10	Tetramethylbenzenes	134.00	0.08	25.01	622.10	0.44
11	C_{11}	147.00	0.06	23.17	643.60	0.48
12	C_{12}	161.00	0.05	21.63	663.90	0.52
13	C_{13}	175.00	0.06	20.43	682.40	0.56
14	C_{14}	190.00	0.05	19.33	700.70	0.60
15	C_{15}	206.00	0.04	18.25	718.60	0.65
16	C_{16}	222.00	0.04	17.15	734.50	0.68
17	C_{17}	237.00	0.05	16.35	749.20	0.73
18	C_{18}	251.00	0.04	15.65	760.50	0.76
19	C_{19}	263.00	0.03	15.06	771.00	0.79
20	C_{20}	275.00	0.02	14.36	782.90	0.82
21	C_{21}	291.00	0.02	13.83	793.30	0.86
22	C_{22}	300.00	0.02	13.26	804.40	0.88
23	C_{23}	312.00	0.02	12.83	814.00	0.92
24	C_{24}	324.00	0.02	12.38	823.20	0.94
25-34	C_{25}-C_{34}	405.13	0.06	8.86	821.63	1.08
35-43	C_{35}-C_{43}	539.73	0.03	6.70	892.33	1.29
44-48	C_{44}-C_{48}	641.91	0.01	5.54	938.59	1.42
49+	C_{49+}	906.62	0.03	3.53	1044.31	1.70
		234.67	**1**			

4.5.2. Mathematical Modeling

4.5.2.1. Thermodynamic Model

WinProp (CMG, 2011) models the asphaltene precipitation for crude oil #5 and CO_2 mole% injections. A multiphase flash calculation models the precipitation of asphaltenes from oil-CO_2 mixtures. Here, the fluid phase includes the oil and CO_2, and the solid phase is the asphaltene particles. The PR-EOS describes the fluid phase, and a solid thermodynamic model proposed by Nghiem et al. in 1993, 1997, and 2000; and Khose et al. in 2000 describes the solid phase. The fugacity of the asphaltenes in the solid model is calculated using *Equation 37* (Kohse et al., 2000; Nghiem et al., 1993, 2000; Nghiem & Coombe, 1997).

$$ln f_s = ln f_s^* + \frac{v_s}{R}\left[\frac{p - p_{tp}}{T} - \frac{p^* - p_{tp}}{T^*}\right] - \frac{\Delta H_{tp}}{R}\left[\frac{1}{T} - \frac{1}{T^*}\right] - \frac{\Delta C_p}{R}\left[\ln\left(\frac{T^*}{T}\right) - T_{tp}\left(\frac{1}{T} - \frac{1}{T^*}\right)\right] \quad \text{Equation 37}$$

where f_s is the asphaltenes fugacity at pressure p and temperature T, f_s^* is the reference fugacity at reference pressure $p^*$and reference temperature T^*, v_s is the asphaltenes solid molar volume, ΔC_p is the solid-liquid heat capacity difference, ΔH_{tp} is the heat of fusion at the triple point, p_{tp} and T_{tp} are the pressure and temperature at the triple point, and R is the universal gas constant.

Equation 37 was used in the WinProp program to model the experimental asphaltene precipitation results shown in *Table 28*. However, inconsistent results were found when *Equation 37* was used.

An approximation of the solid model is proposed for isothermal conditions. The fugacity of the asphaltenes in the solid model is calculated using *Equation 38*.

$$lnf_s = lnf_s^* + v_s(p - p^*)/RT \qquad \text{Equation 38}$$

4.5.2.2. Characterization of the Solid Forming Component

Asphaltenes are defined as the heaviest components of crude oil. Either *Equation 37* or *Equation* 38 requires the asphaltenes components' specification to determine the solid fugacity. The maximum mass content in the oil can be calculated by splitting the oil plus fraction. Usually, the plus fraction is split to C_{49+}. The C_{49+} molar fraction and molecular weight are determined from WinProp. The C_{49+} asphaltene content is determined for a specific volume of oil (SDS microscope view volume). The C_{49+} asphaltene precipitation is compared to the experimental asphaltene precipitation from section *4.2 Asphaltene Content by ASTM-3279.* The asphaltene content in the plus fraction must be higher than the asphaltene content obtained in section *4.2*. The plus fraction asphaltene content represents the total asphaltene content in the oil, including asphaltene precipitation by solvent injection and changes in pressure and temperature.

This work shows the composition of crude oil #5 in *section 4.5.1 Oil Characterization, Table 29*. The C_{25+} component was split to C_{49+}, and the asphaltene content was calculated. *Table* 31 shows the single calculation for the total mass oil at 25 °C in the SDS microscope view.

Table 31. Total mass oil calculation in SDS microscope view

camera window diameter, in	0.500
camera window diameter, cm	1.270
camera window area, cm^2	1.267
oil density, g/cm^3 @25°C	0.836
camera window width, cm (diameter tube SDS)	0.240
oil volume, cm^3	0.304
oil mass, g	**0.254**

From the splitting in WinProp, the molar fraction of the C_{49+} component is 0.031, and its molecular weight is 906.624 g/mole.

Table 32 summarizes all asphaltene content calculations for 25, 60, 90, and 120°C. Results are almost the same corroborating that temperature does not impact the solid content of oil without solvent.

Table 32. Asphaltene content wt% in the C_{49+} component

	Crude oil #5			**Asphaltene C_{49+}**			
T, °C	**density, g/cm^3**	**mass, g**	**mole**	**mole**	**mass, g**	**wt, %**	**mole fraction**
25	0.836	0.254	1.083E-03	3.312E-05	0.030	**11.816**	0.031
60	0.805	0.245	1.042E-03	3.187E-05	0.029	**11.816**	0.031
90	0.784	0.238	1.015E-03	3.105E-05	0.028	**11.816**	0.031
120	0.763	0.232	9.878E-04	3.021E-05	0.027	**11.816**	0.031

The asphaltene content found for the C_{49+} component is 11.816 wt%, a value very close to the asphaltene content found from the precipitation with n-pentane in *Table 21*, 10.955 wt%. This value suggests reducing the plus fraction to increase the asphaltene content in the heaviest fraction of crude oil #5. A new asphaltene content calculation is made this time for the C_{25+} component.

From the splitting in WinProp, the molar fraction of the C_{25+} component is 0.134, and its molecular weight is 570 g/mole.

Table 33 summarizes all asphaltene content calculations for 25, 60, 90, and 120°C. Results are almost the same corroborating that temperature does not impact the solid content of oil without solvent.

Table 33. Asphaltene content wt% in the C_{25+} component

	Oil			C_{25+}			
T, °C	**density, g/cm^3**	**mass, g**	**mole**	**mole**	**mass, g**	**wt, %**	**mole fraction**
25	0.829	0.252	1.07E-03	1.44E-04	0.082	**32.548**	0.134
60	0.805	0.245	1.04E-03	1.40E-04	0.080	**32.548**	0.134
90	0.784	0.238	1.02E-03	1.36E-04	0.078	**32.548**	0.134
120	0.763	0.232	9.88E-04	1.32E-04	0.075	**32.548**	0.134

The value of asphaltene content, 32.548 wt%, is an excellent value to start the asphaltene precipitation modeling in WinProp.

4.5.2.3. Irreversible Asphaltene Calculations

The irreversible or reversible mechanisms of asphaltene precipitation are described by:

$$S_1 \underset{K}{\longleftrightarrow} S_2 \qquad \text{Equation 39}$$

where S_1 is the reversible solid and S_2 is the irreversible solid. The rate formation of S_2 is given by:

$$r = k_{12}C_1 - k_{21}C_2 \qquad \text{Equation 40}$$

where C_1 and C_2 are the molar concentrations of S_1 and S_2 respectively.

The equilibrium constant, *K* is defined as:

$$K = \frac{k_{21}}{k_{12}} = \frac{C_1}{C_2} \quad \text{Equation 41}$$

The mole fraction of reversible solid relative to the total amount of solid is:

$$x_1 = \frac{C_1}{C_2 + C_1} = \frac{K}{K + 1} \quad \text{Equation 42}$$

and the mole fraction of the irreversible solid is:

$$x_2 = \frac{C_2}{C_2 + C_1} = \frac{1}{K + 1} \quad \text{Equation 43}$$

where *K*=0 indicates all the solid is reversible, *K*=1 gives equal amounts of irreversible and reversible solid, and *K*>>1 implies that all the solid is reversible. For this analysis, *K*=0 is used.

4.5.2.4. Specification of the solid model parameters

- ***Asphaltene precipitating component***

As mentioned before, the heaviest component is considered the asphaltene component. However, this asphaltene component, C_{25+} does not fully precipitate as a solid phase. The C_{25+} component is splitting into a non-precipitating, C_{25A+} and a precipitating component, C_{25B+}. In the oil characterization, these two components, C_{25A+} and C_{25B+}, have the same critical properties and acentric factors, but C_{25B+} have higher binary interaction coefficients with respect to the lightest components up to C_5.

- ***Asphaltene precipitating composition***

The composition of the precipitating component, C_{25B+} is calculated by:

$$x_{C_{25B+}} = A_c \frac{MW_{oil}}{MW_{C_{25+}}} \quad \text{Equation 44}$$

where $x_{C_{25B+}}$is the mole fraction of the C_{25B+} component, A_c is the experimental asphaltene mass content from *Table 21*, MW_{oil} is the molecular weight of oil, and $MW_{C_{25+}}$ is the molecular weight of the C_{25B+} component. The mole fraction composition of the C_{25B+} is discount from the C_{25+} mole fraction and the difference is assigned to the C_{25A+}. *Table 34* shows the compositional analysis and SCN properties for crude oil #5 with the C_{25B+} component.

- ***Reference solid fugacity for solid model***

WinProp calculates the reference fugacity by setting a new oil composition identical to the crude oil #5 composition but C_{25B+} mole composition calculated from the asphaltene mass content at the isothermal UAOP. The solid thermodynamic model uses this new oil #5 composition and the UAOP, temperature, and CO_2 mole% injection. The model is run, and the solid molar volume calculated from *Equation 38* is used as the initial value for predicting the asphaltene precipitation in the solid model.

Table 34. Compositional analysis and SCN properties for crude oil #5 with C_{25B+} component

SCN	Component	MW, g/mole	mole, % (z_N)	Pc (atm)	Tc (K)	Acentric Factor
7	Toluene	100	8.9	28.61	549.69	0.31
8	Dimethylbenzene	114	8.1	26.09	578.55	0.35
9	Trimethylbenzenes	128	10.6	23.94	605.54	0.40
10	Tetramethylbenzenes	142	7.6	22.14	630.45	0.44
11	C_{11}	156	5.8	20.61	653.59	0.48
12	C_{12}	170	4.6	19.28	675.19	0.52
13	C_{13}	184	6.1	18.12	695.44	0.56
14	C_{14}	198	5.5	17.10	714.52	0.59
15	C_{15}	212	4.4	16.21	732.55	0.63
16	C_{16}	226	3.7	15.41	749.66	0.67
17	C_{17}	240	5	14.71	765.95	0.70
18	C_{18}	254	3.9	14.08	781.50	0.74
19	C_{19}	268	3	13.52	796.37	0.77
20	C_{20}	282	2.1	13.02	810.63	0.81
21	C_{21}	296	2.4	12.57	824.34	0.84
22	C_{22}	310	1.7	12.16	837.53	0.88
23	C_{23}	324	1.8	11.80	850.25	0.93
24	C_{24}	338	1.4	11.46	862.53	0.96
25A+	C_{25A+}	570	9.28	6.69	956.24	1.31
25B+	C_{25B+}	570	4.12	6.69	956.24	1.31
		234.67	**100**			

- ***Additional Onset Pressures***

When more additional experimental onset pressures and its asphaltene content are available at different temperatures, the solid thermodynamic model will calculate:

✓ With one additional point - ΔC_p

✓ With two additional points - ΔC_p and ΔH_{tp}

✓ With three additional points- ΔC_p, ΔH_{tp}, and v_s.

Typically, only one additional point is required to use Equation 38, adjusting the solid molar volume to the asphaltene precipitation experimental data. One additional point is what is used in this work.

- ***Number of components***

For this case, the number of components considered asphaltenes is only one, and it is the C_{25+} component. More than one component can be specified.

4.5.3. Asphaltene Precipitation Simulation Results

A second solid model is run in WinProp using the previous solid molar volume calculated for the reference fugacity in section *4.5.2.4 Specification of the solid model parameters.*

The calculated solid molar volume is adjusted to match the experimental asphaltene precipitation at saturation pressure. The final adjusted solid molar volume is annotated for the isothermal conditions and the CO_2 injection fraction. A new solid model is run for the next CO_2 injection fraction at the same isothermal condition until all the calculated solid molar

volumes can successfully predict the asphaltene precipitation at saturation point for all conditions.

The simulated and experimental asphaltene content precipitation for isothermals at 25, 60, 90, and 120 °C are shown in *Table 35* and *Figure 53* to *56* compare the experimental and simulated asphaltene precipitation. For each CO_2 mole% injection at isotherm conditions, a value of solid molar volume, v_s was adjusted.

Table 35. Simulated asphaltene precipitation weight percentage at Psat

Psat					
CO_2-mole%	**Oil-mole%**	**Asphaltene C_{25B+} precipitation, wt% (simulation)**			
		25 °C	**60 °C**	**90 °C**	**120 °C**
25	75	**0.941**	**0.658**	**0.417**	**0.192**
35	65	**3.751**	**1.592**	**1.014**	**0.526**
45	55	**8.360**	**6.833**	**3.014**	**1.502**

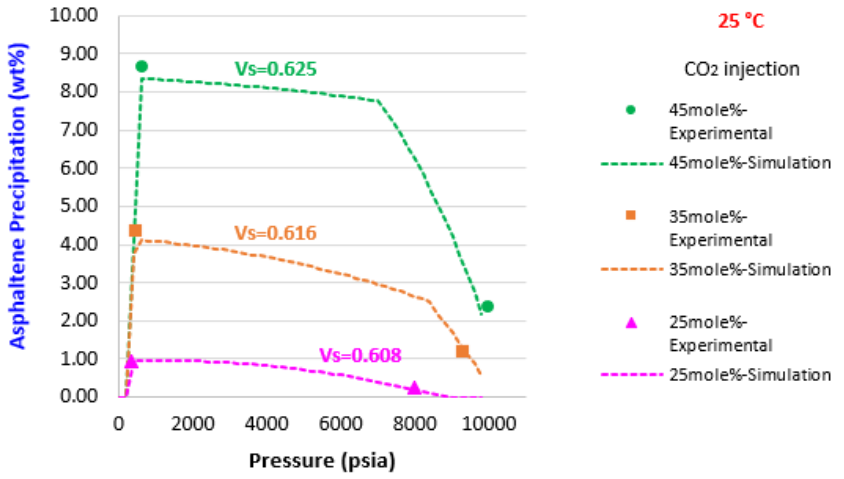

Figure 53. Experimental and simulated asphaltene precipitation at 25 °C

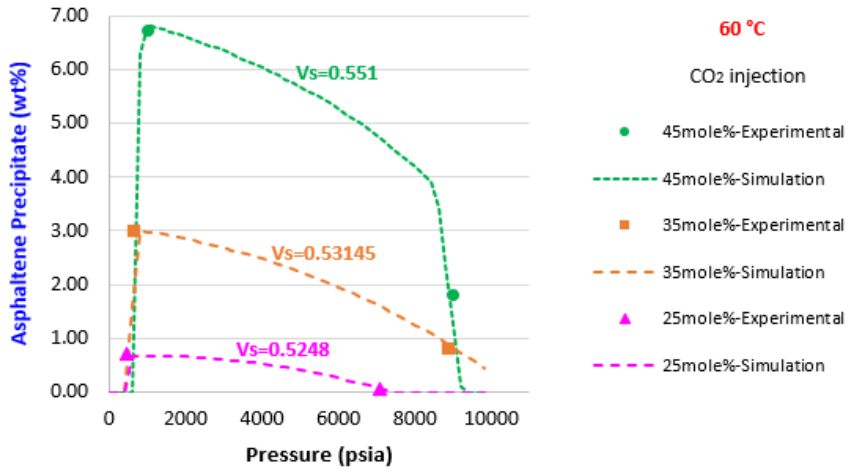

Figure 54. Experimental and simulated asphaltene precipitation at 60 °C

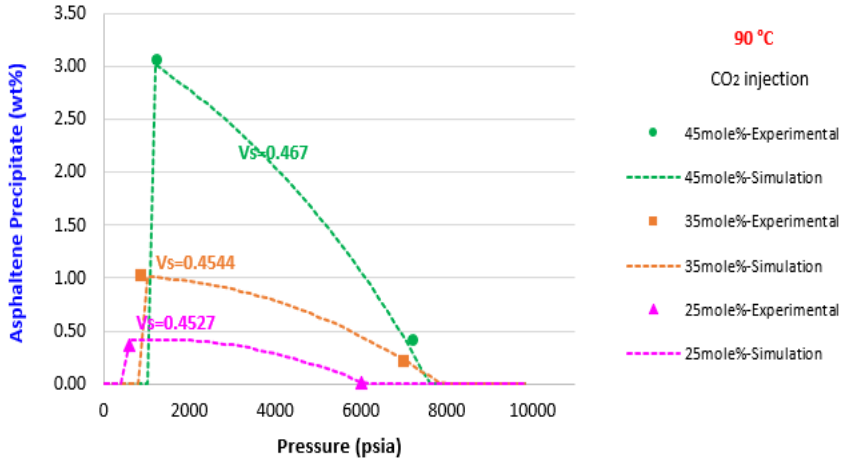

Figure 55. Experimental and simulated asphaltene precipitation at 90 °C

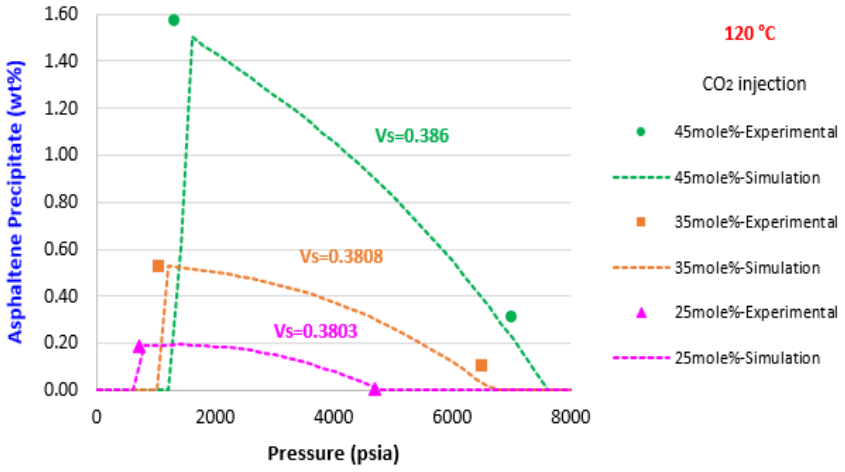

Figure 56. Experimental and simulated asphaltene precipitation at 120 °C

4.5.4. Developed Solid Molar Volume Equation

The solid molar volumes were adjusted to match the experimental values of asphaltene precipitation. *Table 36* shows solid molar volumes after tuning at isothermal conditions for the C_{25B+} component of the mixture (crude oil #5 and CO_2). The solid molar volume slightly increases with the CO_2 injection in the mixture and decreases with temperature increments.

Table 36. Solid molar volumes after tuning for asphaltene C_{25B+} component

CO_2-mole%	**Oil-mole%**	**Solid molar volume for asphaltene C_{25B+}, l/mole**			
		25 °C	**60 °C**	**90 °C**	**120 °C**
25	75	**0.6080**	**0.5248**	**0.4527**	**0.3803**
35	65	**0.6160**	**0.5315**	**0.4544**	**0.3808**
45	55	**0.6250**	**0.5510**	**0.4670**	**0.3860**

The solid molar volume is mainly changing with temperature and CO_2 mole% injection. However, the solid model available in WinProp does not match the whole experimental data at different temperatures and CO_2 mole% injections. For that reason, many values for solid molar volumes were found. This computational work is time-consuming and implies many additional calculations. For this reason, a developed solid molar volume equation function of both temperature and CO_2 mole% injection is presented in *Equation 45.*

$$v_s(\text{l/mole}) = 0.6528 - 0.0025T(°C) + 0.0008X_{CO_2}(\text{mole\%})$$

Equation 45

The WinProp modeled and developed equation calculated solid molar volumes are shown in *Figure 57.* The AARD calculated for the solid molar volumes modeled and calculated with the developed equation gives a value of 0.704%, confirming the proposed equation's accuracy.

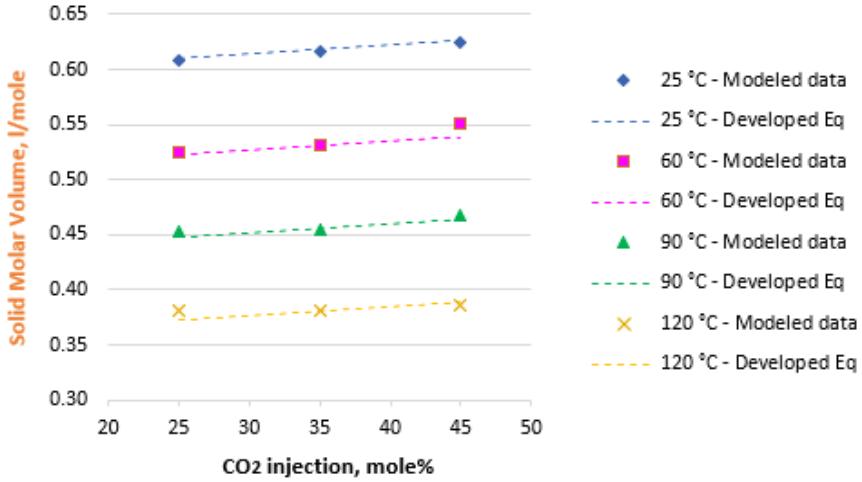

Figure 57. WinProp modeled and developed equation calculated solid molar volumes

Equation 45 can modify *Equation 38* for calculating the asphaltene precipitation at any temperature and CO_2 mole% injection in crude oil #5 mixture. The developed equation modifying the solid model can accurately predict the asphaltene precipitation mass content for crude oil #5 EOR assisted with CO2 injections at different isothermal conditions, saving a lot of time-consuming simulation work and additional calculations.

4.5.5. Summary

The oil characterization is initially performed, determining the compositional analysis by gas chromatography. The results obtained are typical for light dead oil. The largest mole fraction is found for the C_{25+} component, 0.326 mole fraction. The plus fraction is characterized by splitting the C_{25+} component to C_{49+}, typically used as the asphaltene component. The molecular weight, specific gravity, boiling temperature, critical pressure, critical temperature, and acentric factors for the C_{7+} fractions are calculated internally by WinProp. In this case, the lumping is not required since the objective of the oil characterization is to define the heaviest plus fraction to be used as the asphaltene component in the following thermodynamic calculations of saturation pressure and asphaltene precipitation.

This work measured the experimental data with a new high-pressure-high-temperature fully visual SDS. The solid thermodynamic model available in WinProp successfully predicts the experimental asphaltene precipitation for isothermal conditions in a fixed fraction of crude oil and CO_2 injection. However, the model showed limitations in predicting data at different temperatures and CO_2 mole% injections. For that reason, a developed equation is proposed to calculate the asphaltene's molar volume in the solid phase. This developed equation correlates temperature and CO_2 mole fraction in one single function. The values of asphaltene molar volumes obtained from this equation show an AARD of 0.704% with respect to the solid molar volumes from WinProp, corroborating the accuracy of the proposed equation. Using the developed equation combined with the solid molar model to predict asphaltene precipitation in crude oil #5 - EOR assisted with CO_2 at different isothermal conditions can save hours of time-consuming modeling work.

Chapter 5: Conclusions, Limitations, and Future Directions

Conclusions

The solid model used to predict asphaltene precipitation shows limitations for different CO_2 mole% injections at different isothermal conditions. Therefore, a developed correlation is proposed. The proposed asphaltene molar volume equation correlates CO_2 mole% injections and temperature to match the experimental asphaltene precipitation data. The results were satisfactory, with an AARD of 0.704%.

This work concludes that asphaltene precipitation from a CO_2-EOR process can successfully be predicted from the experiments in the PVT-SDS and the adapted modeling from WinProp. In this CO_2-induced flooding process, the gas injection takes higher importance when the injection is higher than 25 mole%. Regarding the temperature, asphaltene precipitation is worst at 25 °C and 35 and 45 mole%. These unfavorable conditions are more likely to develop irreversible processes, leading to asphaltene deposition. Saturation pressures during CO_2-EOR are commonly measured, ignoring the asphaltenes phase behavior. However, for systems oil-CO_2-asphaltenes, the phase behavior must be studied to avoid asphaltene deposition at early production conditions. The present experiments show that four different asphaltene phase behaviors are developed in the system for a reversible asphaltene process. The key to avoiding asphaltene problems is thermodynamic control and not reaching the irreversible process, where asphaltene particles do not re-peptized again into the oil phase.

Limitations

It is fair to acknowledge the limitations this work has faced. Those are listed as follows:

1) The SDS is equipped with an HPHT high-resolution video camera and can perform statistical analyses for microparticles. However, the asphaltene particles obtained from the CO_2-EOR experiment were too tiny that the software could not recognize their sizes. The asphaltene precipitation areas were calculated from the pictures taken in the experiment, which was an additional time not expected in this work. For the case where n-pentane was used as a solvent, the asphaltene particles were high enough to be detected for the system. Although, it helped set a reference for further asphaltene particle analyses.
2) The solid thermodynamic model works very well for a defined plus component set as the asphaltene component. Nonetheless, the plus component is unknown, and a trial and error task can be tricky and time-consuming. Many investigations where the solid model is used suggest initially setting C_{49+} as the plus fraction for asphaltenes. Nevertheless, the asphaltene content must match experimental data, which is not always possible with C_{49+}.
3) Due to that, the WinProp model does not predict the asphaltene precipitation at different temperatures and CO_2 injections; the asphaltene enveloped could not be plotted in the program.
4) The HPHT high-resolution camera of the SDS cannot directly identify dark, crude oil asphaltenes. The sample needs to be mixed with a solvent such as n-pentane or CO_2 like in this work.

Future Directions

The future study of the following points can complement this work:

1) The developed solid molar volume correlation proposed in this work must be evaluated with a programming language to create the asphaltene phase behavior envelope.
2) New models for asphaltene precipitation modeling use PC-SAFT to predict the asphaltene phase behavior. The verification of this work using PC-SAFT EOS can help reduce computational time. However, it is required the SARA analysis for that purpose.
3) The study of minimum miscibility pressure (MMP) can complement this work to study its relationship with AOP.
4) Asphaltene deposition experiments might be performed for the irreversible process cases predicted in this work.

References

Abedini, A., & Abedini, R. (2012). Investigation of Splitting and Lumping of Oil Composition on the Simulation of Asphaltene Precipitation. *Petroleum Science and Technology*, *30*(1), 1–8. https://doi.org/10.1080/10916461003735137

Afra, S., Samouei, H., Golshahi, N., & Nasr-El-Din, H. (2020). Alterations of asphaltenes chemical structure due to carbon dioxide injection. *Fuel*, *272*, 117708. https://doi.org/10.1016/j.fuel.2020.117708

Akbarzadeh, K., Hammami, A., Kharrat, A., Zhang, D., Allenson, S., Creek, J., Kabir, S., Jamaluddin, A., Marshall, A. G., Rodgers, R., Mullins, O., & Solbakken, T. (2007). Asphaltenes—Problematic but rich in potential. *Oilfield Review*, *19*, 22–43.

AlHammadi, A. A., Chen, Y., Yen, A., Wang, J., Creek, J. L., Vargas, F. M., & Chapman, W. G. (2017). Effect of the Gas Composition and Gas/Oil Ratio on Asphaltene Deposition. *Energy & Fuels*, *31*(4), 3610–3619. https://doi.org/10.1021/acs.energyfuels.6b02313

Al-Qasim, A. (2017). Asphaltene Phase Behavior Modeling for Wells from the Middle East. *Day 1 Mon, May 08, 2017*, D011S002R004. https://doi.org/10.2118/185976-MS

Anton Paar. (2022). *Density meter: DMA 4500 M :: Anton-Paar.com*. Anton Paar. https://www.anton-paar.com/kr-en/products/details/benchtop-density-meter-dma-4500-m/

Arnaut, M., Vulin, D., José García Lamberg, G., & Jukić, L. (2021). Simulation Analysis of CO2-EOR Process and Feasibility of CO2 Storage during EOR. *Energies*, *14*(4), 1154. https://doi.org/10.3390/en14041154

Ashoori, S., Sharifi, M., Masoumi, M., & Mohammad Salehi, M. (2017). The relationship between SARA fractions and crude oil stability. *Egyptian Journal of Petroleum*, *26*(1), 209–213. https://doi.org/10.1016/j.ejpe.2016.04.002

ASTM-D02 Committee. (2008). *Test Method for Boiling Range Distribution of Petroleum Fractions by Gas Chromatography*. ASTM International. https://doi.org/10.1520/D2887-19AE02

ASTM-D04 Committee. (2007). *Test Method for n-Heptane Insolubles*. ASTM International. https://doi.org/10.1520/D3279-19

Baker, L. E., Pierce, A. C., & Luks, K. D. (1982). Gibbs Energy Analysis of Phase Equilibria. *Society of Petroleum Engineers Journal*, *22*(05), 731–742. https://doi.org/10.2118/9806-PA

Becker, J. R. (1997). *Crude oil waxes, emulsions, and asphaltenes*. Pennwell Books.

Boussingault, J. B. (1837). Mémoire sur la composition des bitumes. *In Annales de Chimie et de Physique*, *64*, 141.

Brookfield. (2022). *DV2T Viscometer*. AMETEK Brookfield North America. https://store.brookfieldengineering.com/dv2t-viscometer/

Buckley, J. S., Hirasaki, G. J., Liu, Y., Von Drasek, S., Wang, J.-X., & Gill, B. S. (1998). Asphaltene Precipitation and Solvent Properties of Crude Oils. *Petroleum Science and Technology*, *16*(3–4), 251–285. https://doi.org/10.1080/10916469808949783

Buckley, J. S., Wang, J., & Creek, J. L. (2007). Solubility of the Least-Soluble Asphaltenes. In O. C. Mullins, E. Y. Sheu, A. Hammami, & A. G. Marshall (Eds.), *Asphaltenes, Heavy Oils, and Petroleomics* (pp. 401–437). Springer. https://doi.org/10.1007/0-387-68903-6_16

Buenrostro-Gonzalez, E., Lira-Galeana, C., Gil-Villegas, A., & Wu, J. (2004). Asphaltene precipitation in crude oils: Theory and experiments. *AIChE Journal*, *50*(10), 2552–2570. https://doi.org/10.1002/aic.10243

Chaisoontornyotin, W., W, B. A., & P, H. M. (2017). Reversibility of Asphaltene Precipitation Using Temperature-Induced Aggregation. *Energy & Fuels*. https://doi.org/10.1021%2Facs.energyfuels.6b02344

Chueh, P. L., & Prausnitz, J. M. (1967). Vapor-liquid equilibria at high pressures: Calculation of partial molar volumes in nonpolar liquid mixtures. *AIChE Journal*, *13*(6), 1099–1107. https://doi.org/10.1002/aic.690130612

Coats, K. H., & Smart, G. T. (1986). Application of a Regression-Based EOS PVT Program to Laboratory Data. *SPE Reservoir Engineering*, *1*(03), 277–299. https://doi.org/10.2118/11197-PA

Daryasafar, A., Masoudi, M., Kord, S., & Madani, M. (2020). Evaluation of different thermodynamic models in predicting asphaltene precipitation: A comparative study. *Fluid Phase Equilibria*, *514*, 112557. https://doi.org/10.1016/j.fluid.2020.112557

de Boer, R. B., Leerlooyer, K., Eigner, M. R. P., & van Bergen, A. R. D. (1995). Screening of Crude Oils for Asphalt Precipitation: Theory, Practice, and the Selection of Inhibitors. *SPE Production & Facilities*, *10*(01), 55–61. https://doi.org/10.2118/24987-PA

Dickie, J. P., & Yen, T. Fu. (1967). Macrostructures of the asphaltic fractions by various instrumental methods. *Analytical Chemistry*, *39*(14), 1847–1852. https://doi.org/10.1021/ac50157a057

Du, X. (2018). *ENHANCED SOLUBILITY OF CO2-OIL MIXTURE IN THE PRESENCE OF C3H8 UNDER RESERVOIR CONDITIONS*. University of Kansas.

Dufour, J., Calles, J. A., Marugán, J., Giménez-Aguirre, R., Peña, J. L., & Merino-García, D. (2010). Influence of Hydrocarbon Distribution in Crude Oil and Residues on Asphaltene Stability. *Energy & Fuels*, *24*(4), 2281–2286. https://doi.org/10.1021/ef900934t

Elkahky, S., Lagat, C., Sarmadivaleh, M., & Barifcani, A. (2019). A comparative study of density estimation of asphaltene structures using group contribution methods and molecular dynamic simulations for an Australian oil field. *Journal of Petroleum Exploration and Production Technology*, *9*(4), 2699–2708. https://doi.org/10.1007/s13202-019-0641-x

Espinoza Mejia, J. E., Li, X., & Zheng, R. (2022, February 16). *Experimental Study of Asphaltene Precipitation and Deposition During Immiscible CO2—EOR Process*. SPE International Conference and Exhibition on Formation Damage Control. https://doi.org/10.2118/208802-MS

Fakher, S., Ahdaya, M., Elturki, M., & Imqam, A. (2020). Critical review of asphaltene properties and factors impacting its stability in crude oil. *Journal of Petroleum Exploration and Production Technology*, *10*(3), 1183–1200. https://doi.org/10.1007/s13202-019-00811-5

Ferworn, K. A., Svrcek, W. Y., & Mehrotra, A. K. (1993). Measurement of asphaltene particle size distributions in crude oils diluted with n-heptane. *Industrial & Engineering Chemistry Research*, *32*(5), 955–959. https://doi.org/10.1021/ie00017a026

Flory, P. J. (1944). Thermodynamics of Heterogeneous Polymer Solutions. *The Journal of Chemical Physics*, *12*(3), 114–115. https://doi.org/10.1063/1.1723916

Ghasemi, M., & Al-Safran, E. (2020). Integrated reservoir/wellbore production model for oil field asphaltene deposition management. *Journal of Petroleum Science and Engineering*, *192*, 107213. https://doi.org/10.1016/j.petrol.2020.107213

Ghloum, E. F., Rashed, A. M., Safa, M. A., Sablit, R. C., & Al-Jouhar, S. M. (2019). Mitigation of asphaltenes precipitation phenomenon via chemical inhibitors. *Journal of Petroleum Science and Engineering*, *175*, 495–507. https://doi.org/10.1016/j.petrol.2018.12.071

Gonzalez, D. L., Vargas, F. M., Hirasaki, G. J., & Chapman, W. G. (2008). Modeling Study of CO_2-Induced Asphaltene Precipitation. *Energy & Fuels*, *22*(2), 757–762. https://doi.org/10.1021/ef700369u

González, F. A. (2015). *Personal communication. Asphaltene deposition economic impact.* Reservoir performance global community of practice lead BP.

Guzmán, R., Rodríguez, S., Torres-Mancera, P., & Ancheyta, J. (2021). Evaluation of Asphaltene Stability of a Wide Range of Mexican Crude Oils. *Energy & Fuels*, *35*(1), 408–418. https://doi.org/10.1021/acs.energyfuels.0c03301

Hassanzadeh, M., & Abdouss, M. (2022). A comprehensive review on the significant tools of asphaltene investigation. Analysis and characterization techniques and computational methods. *Journal of Petroleum Science and Engineering*, *208*, 109611. https://doi.org/10.1016/j.petrol.2021.109611

Hildebrand, J. H., & Wood, S. E. (1933). The Derivation of Equations for Regular Solutions. *The Journal of Chemical Physics*, *1*(12), 817–822. https://doi.org/10.1063/1.1749250

Hirschberg, A., deJong, L. N. J., Schipper, B. A., & Meijer, J. G. (1984). Influence of Temperature and Pressure on Asphaltene Flocculation. *Society of Petroleum Engineers Journal*, *24*(03), 283–293. https://doi.org/10.2118/11202-PA

Hosseini-Dastgerdi, Z., Tabatabaei-Nejad, S. A. R., Sahraei, E., & Nowroozi, H. (2015). Morphology and Size Distribution Characterization of Precipitated Asphaltene from Live Oil During Pressure Depletion. *Journal of Dispersion Science and Technology*, *36*(3), 363–368. https://doi.org/10.1080/01932691.2014.910668

Huggins, M. L. (1942). Theory of Solutions of High Polymers [1]. *Journal of the American Chemical Society*, *64*(7), 1712–1719. https://doi.org/10.1021/ja01259a068

Karan, K., Hammami, A., Flannery, M., & Artur Stankiewicz, B. (2003). Evaluation of Asphaltene Instability and a Chemical Control During Production of Live Oils. *Petroleum Science and Technology*, *21*(3–4), 629–645. https://doi.org/10.1081/LFT-120018543

Khaleel, A., Abutaqiya, M., Tavakkoli, M., Melendez-Alvarez, A. A., & Vargas, F. M. (2015). On the Prediction, Prevention and Remediation of Asphaltene Deposition. *Day 1 Mon, November 09, 2015*, D011S013R003. https://doi.org/10.2118/177941-MS

Kohse, B. F., Nghiem, L. X., Maeda, H., & Ohno, K. (2000). Modelling Phase Behaviour Including the Effect of Pressure and Temperature on Asphaltene Precipitation. *All Days*, SPE-64465-MS. https://doi.org/10.2118/64465-MS

Kokal, S. L., & Sayegh, S. G. (1995). Asphaltenes: The Cholesterol Of Petroleum. *All Days*, SPE-29787-MS. https://doi.org/10.2118/29787-MS

Lee, B. I., & Kesler, M. G. (1975). A generalized thermodynamic correlation based on three-parameter corresponding states. *AIChE Journal*, *21*(3), 510–527. https://doi.org/10.1002/aic.690210313

Leontaritis, K. J., & Ali Mansoori, G. (1988). Asphaltene deposition: A survey of field experiences and research approaches. *Journal of Petroleum Science and Engineering*, *1*(3), 229–239. https://doi.org/10.1016/0920-4105(88)90013-7

Maqbool, T., Balgoa, A. T., & Fogler, H. S. (2009). Revisiting Asphaltene Precipitation from Crude Oils: A Case of Neglected Kinetic Effects. *Energy & Fuels*, *23*(7), 3681–3686. https://doi.org/10.1021/ef9002236

Michelsen, M. L. (1982). The isothermal flash problem. Part I. Stability. *Fluid Phase Equilibria*, *9*(1), 1–19. https://doi.org/10.1016/0378-3812(82)85001-2

Mitchell, D. L., & Speight, J. G. (1973). The solubility of asphaltenes in hydrocarbon solvents. *Fuel*, *52*(2), 149–152. https://doi.org/10.1016/0016-2361(73)90040-9

Mohammadi, S., Rashidi, F., Mousavi-Dehghani, S. A., & Ghazanfari, M.-H. (2016a). Modeling of asphaltene aggregation phenomena in live oil systems at high pressure-high temperature. *Fluid Phase Equilibria*, *423*, 55–73. https://doi.org/10.1016/j.fluid.2016.04.010

Mohammadi, S., Rashidi, F., Mousavi-Dehghani, S. A., & Ghazanfari, M.-H. (2016b). On the effect of temperature on precipitation and aggregation of asphaltenes in light live oils. *The Canadian Journal of Chemical Engineering*, *94*(9), 1820–1829. https://doi.org/10.1002/cjce.22555

Mullins, O. C. (2010). The Modified Yen Model. *Energy & Fuels*, *24*(4), 2179–2207. https://doi.org/10.1021/ef900975e

Mullins, O. C., Pomerantz, A. E., Andrews, A. B., Dutta Majumdar, R., Hazendonk, P., Ruiz-Morales, Y., Goual, L., & Zare, R. N. (2017). Asphaltenes. In C. S. Hsu & P. R. Robinson (Eds.), *Springer Handbook of Petroleum Technology* (pp. 221–250). Springer International Publishing. https://doi.org/10.1007/978-3-319-49347-3_6

Nghiem, L. X., & Coombe, D. A. (1997). Modeling Asphaltene Precipitation During Primary Depletion. *SPE Journal*, *2*(02), 170–176. https://doi.org/10.2118/36106-PA

Nghiem, L. X., Hassam, M. S., & Nutakki, R. (1993). *Efficient Modelling of Asphaltene Precipitation*. 10.

Nghiem, L. X., Kohse, B. F., Ali, S. M. F., & Doan, Q. (2000). Asphaltene Precipitation: Phase Behaviour Modelling and Compositional Simulation. *All Days*, SPE-59432-MS. https://doi.org/10.2118/59432-MS

Ortiz, R. ., Perez, C. ., Sánchez, O. ., Aybar, U. ., Tellez, F. ., Mujica, L. ., Aguilar, J. ., Andrade, A. ., Resendiz, T. ., Camarillo, L. ., & Thompson, M. . (2017). Asphaltene-Prevention Work Flow Enhances Oil Production in High-Temperature Fractured Carbonate Reservoirs. *SPE Production & Operations*, *32*(04), 476–490. https://doi.org/10.2118/178956-PA

Pedersen, K. S., Christensen, P. L., & Shaikh, J. A. (2015). *Phase behavior of petroleum reservoir fluids* (Second edition). CRC Press, Taylor & Francis Group.

Pedersen, K. S., Thomassen, P., & Fredenslund, A. (1985). Thermodynamics of petroleum mixtures containing heavy hydrocarbons. 3. Efficient flash calculation procedures using the SRK equation of state. *Industrial & Engineering Chemistry Process Design and Development*, *24*(4), 948–954. https://doi.org/10.1021/i200031a009

Péneloux, A., Rauzy, E., & Fréze, R. (1982). A consistent correction for Redlich-Kwong-Soave volumes. *Fluid Phase Equilibria*, *8*(1), 7–23. https://doi.org/10.1016/0378-3812(82)80002-2

Peng, D.-Y., & Robinson, D. B. (1976). A New Two-Constant Equation of State. *Industrial & Engineering Chemistry Fundamentals*, *15*(1), 59–64. https://doi.org/10.1021/i160057a011

Pfeiffer, J. Ph., & Saal, R. N. J. (1940). Asphaltic Bitumen as Colloid System. *The Journal of Physical Chemistry*, *44*(2), 139–149. https://doi.org/10.1021/j150398a001

Pillon, L. Z. (2001). Effect of Experimental Conditions and Solvents on the Precipitation and Composition of Asphaltenes. *Petroleum Science and Technology*, *19*(5–6), 673–683. https://doi.org/10.1081/LFT-100105282

Punase, A., Prakoso, A., & Hascakir, B. (2016). The Polarity of Crude Oil Fractions Affects the Asphaltenes Stability. *All Days*, SPE-180423-MS. https://doi.org/10.2118/180423-MS

Redlich, Otto., & Kwong, J. N. S. (1949). On the Thermodynamics of Solutions. V. An Equation of State. Fugacities of Gaseous Solutions. *Chemical Reviews*, *44*(1), 233–244. https://doi.org/10.1021/cr60137a013

Riazi, M. R. (1980). Simplify property predictions. *Hydrocarbon Process*, *59*, 115–116.

Sheu, E. Y. (2002). Petroleum AsphalteneProperties, Characterization, and Issues. *Energy & Fuels*, *16*(1), 74–82. https://doi.org/10.1021/ef010160b

Sheu, E. Y., Mullins, O. C., & Fine Particle Society (Eds.). (1995). *Asphaltenes: Fundamentals and applications*. Plenum Press.

Shoukry, A. E., El-Banbi, A. H., & Sayyouh, H. (2020). Enhancing asphaltene precipitation modeling by cubic-PR solid model using thermodynamic correlations and averaging techniques. *Petroleum Science*, *17*(1), 232–241. https://doi.org/10.1007/s12182-019-00377-1

Soave, G. (1972). Equilibrium constants from a modified Redlich-Kwong equation of state. *Chemical Engineering Science*, *27*(6), 1197–1203. https://doi.org/10.1016/0009-2509(72)80096-4

Soleymanzadeh, A., Yousefi, M., Kord, S., & Mohammadzadeh, O. (2019). A review on methods of determining onset of asphaltene precipitation. *Journal of Petroleum Exploration and Production Technology*, *9*(2), 1375–1396. https://doi.org/10.1007/s13202-018-0533-5

Soreide, I. (1989). *Improved phase behavior predictions of petroleum reservoir fluids from a cubic equation of state*.

Subramanian, S., Simon, S., & Sjöblom, J. (2016). Asphaltene Precipitation Models: A Review. *Journal of Dispersion Science and Technology*, *37*(7), 1027–1049. https://doi.org/10.1080/01932691.2015.1065418

Syed, F. I., Ghedan, S. G., Hage, A. R., Tariq, S. M., & Shebl, H. (2012). Formation Flow Impairment in Carbonate Reservoirs Due to Asphaltene Precipitation and Deposition during Hydrocarbon Gas Flooding. *All Days*, SPE-160253-MS. https://doi.org/10.2118/160253-MS

Syed, F. I., Neghabhan, S., Zolfaghari, A., & Dahaghi, A. K. (2020). Numerical Validation of Asphaltene Precipitation and Deposition during CO2 miscible flooding. *Petroleum Research*, *5*(3), 235–243. https://doi.org/10.1016/j.ptlrs.2020.04.002

Taheri-Shakib, J., Saadati, N., Esfandiarian, A., Hosseini, S. A., & Rajabi-Kochi, M. (2020). Characterizing the wax-asphaltene interaction and surface morphology using analytical spectroscopy and microscopy techniques. *Journal of Molecular Liquids*, *302*, 112506. https://doi.org/10.1016/j.molliq.2020.112506

Tavakkoli, M., Chen, A., & Vargas, F. M. (2016). Rethinking the modeling approach for asphaltene precipitation using the PC-SAFT Equation of State. *Fluid Phase Equilibria*, *416*, 120–129. https://doi.org/10.1016/j.fluid.2015.11.003

Tavakkoli, M., Grimes, M. R., Liu, X., Garcia, C. K., Correa, S. C., Cox, Q. J., & Vargas, F. M. (2015). Indirect Method: A Novel Technique for Experimental Determination of Asphaltene Precipitation. *Energy & Fuels*, *29*(5), 2890–2900. https://doi.org/10.1021/ef502188u

Ting, P. D., Gonzalez, D. L., Hirasaki, G. J., & Chapman, W. G. (2007). Application of the PC-SAFT Equation of State to Asphaltene Phase Behavior. In O. C. Mullins, E. Y. Sheu, A. Hammami, & A. G. Marshall (Eds.), *Asphaltenes, Heavy Oils, and Petroleomics* (pp. 301–327). Springer. https://doi.org/10.1007/0-387-68903-6_12

Trangenstein, J. A., & Bell, J. B. (1989). Mathematical Structure of the Black-Oil Model for Petroleum Reservoir Simulation. *SIAM Journal on Applied Mathematics*, *49*(3), 749–783. https://doi.org/10.1137/0149044

Vargas, F. M., Garcia-Bermudes, M., Boggara, M., Punnapala, S., Abutaqiya, M., Mathew, N., Prasad, S., Khaleel, A., Al Rashed, M., & Al Asafen, H. (2014). On the Development of an Enhanced Method to Predict Asphaltene Precipitation. *Day 2 Tue, May 06, 2014*, D021S017R001. https://doi.org/10.4043/25294-MS

Vargas, F. M., Gonzalez, D. L., Hirasaki, G. J., & Chapman, W. G. (2009). Modeling Asphaltene Phase Behavior in Crude Oil Systems Using the Perturbed Chain Form of the Statistical Associating Fluid Theory (PC-SAFT) Equation of State. *Energy & Fuels*, *23*(3), 1140–1146. https://doi.org/10.1021/ef8006678

Vargas, F. M., & Tavakkoli, M. (2018). *Asphaltene Deposition: Fundamentals, Prediction, Prevention, and Remediation*. CRC Press.

Wang, J., & Buckley, J. S. (2003). Asphaltene Stability in Crude Oil and Aromatic SolventsThe Influence of Oil Composition. *Energy & Fuels*, *17*(6), 1445–1451. https://doi.org/10.1021/ef030030y

Whitson, C. H. (1984). Critical Properties Estimation From an Equation of State. *All Days*, SPE-12634-MS. https://doi.org/10.2118/12634-MS

Whitson, C. H., & Brulé, M. R. (2000). *Phase behavior*. Henry L. Doherty Memorial Fund of AIME, Society of Petroleum Engineers.

Wilson, G. M. (1969). A modified Redlich-Kwong equation of state, application to general physical data calculations. *In 65th National AIChE Meeting, Cleveland, OH*, *15*.

Yang, Y. (2020). *PHASE AND VOLUMETRIC BEHAVIOR OF CO2 AND BAKKEN OIL SYSTEM UNDER RESERVOIR CONDITIONS* [Thesis, University of Kansas]. https://kuscholarworks.ku.edu/handle/1808/32638

Yen, T. F., & Chilingarian, G. V. (Eds.). (1994). *Asphaltenes and asphalts* (1st ed. (v. 2)). Elsevier Science.

Yen, T. F., & Chilingarian, G. V. (2000). *Asphaltenes and Asphalts, 2: Part B*. Elsevier.

Zadeh, G. A., Moradi, S., Dabir, B., Emadi, M. A., & Rashtchian, D. (2011). Comprehensive Study of Asphaltene Precipitation due to Gas Injection: Experimental Investigation and modeling. *All Days*, SPE-143454-MS. https://doi.org/10.2118/143454-MS

Zanganeh, P., Ayatollahi, S., Alamdari, A., Zolghadr, A., Dashti, H., & Kord, S. (2012). Asphaltene Deposition during CO_2 Injection and Pressure Depletion: A Visual Study. *Energy & Fuels*, *26*(2), 1412–1419. https://doi.org/10.1021/ef2012744

Zeinali Hasanvand, M., Behbahani, R., Feyzi, F., & Mousavi-Dehghani, S. A. (2017). *Asphaltene particles size and size distribution change at high pressure high temperature conditions: Experimental study on a heavy oil sample*. *46*, 85–99.

Zheng, R. (2020). *Phase Behavior of Single, Binary, and Ternary CH4-C2H6-CO2 Hydrate Systems*. https://kuscholarworks.ku.edu/handle/1808/32640

Zuo, J. Y., Mullins, O. C., Freed, D., Elshahawi, H., Dong, C., & Seifert, D. J. (2013). Advances in the Flory–Huggins–Zuo Equation of State for Asphaltene Gradients and Formation Evaluation. *Energy & Fuels*, *27*(4), 1722–1735. https://doi.org/10.1021/ef301239h